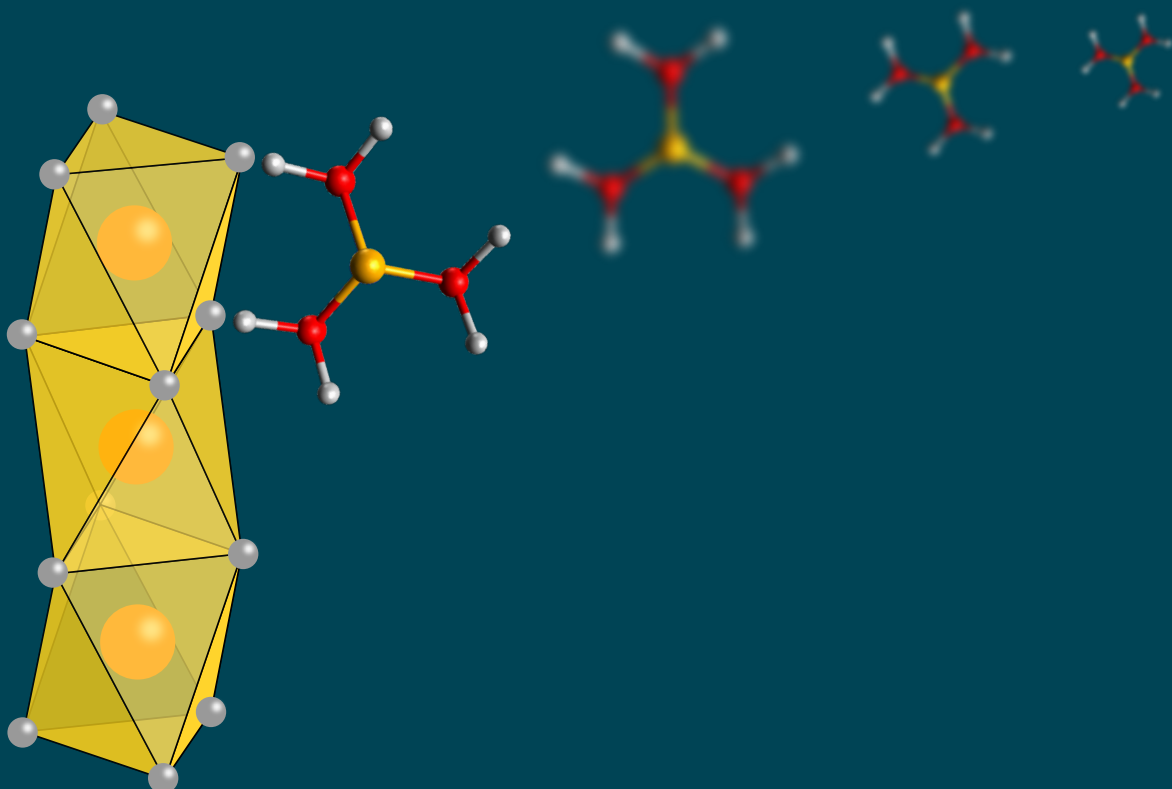
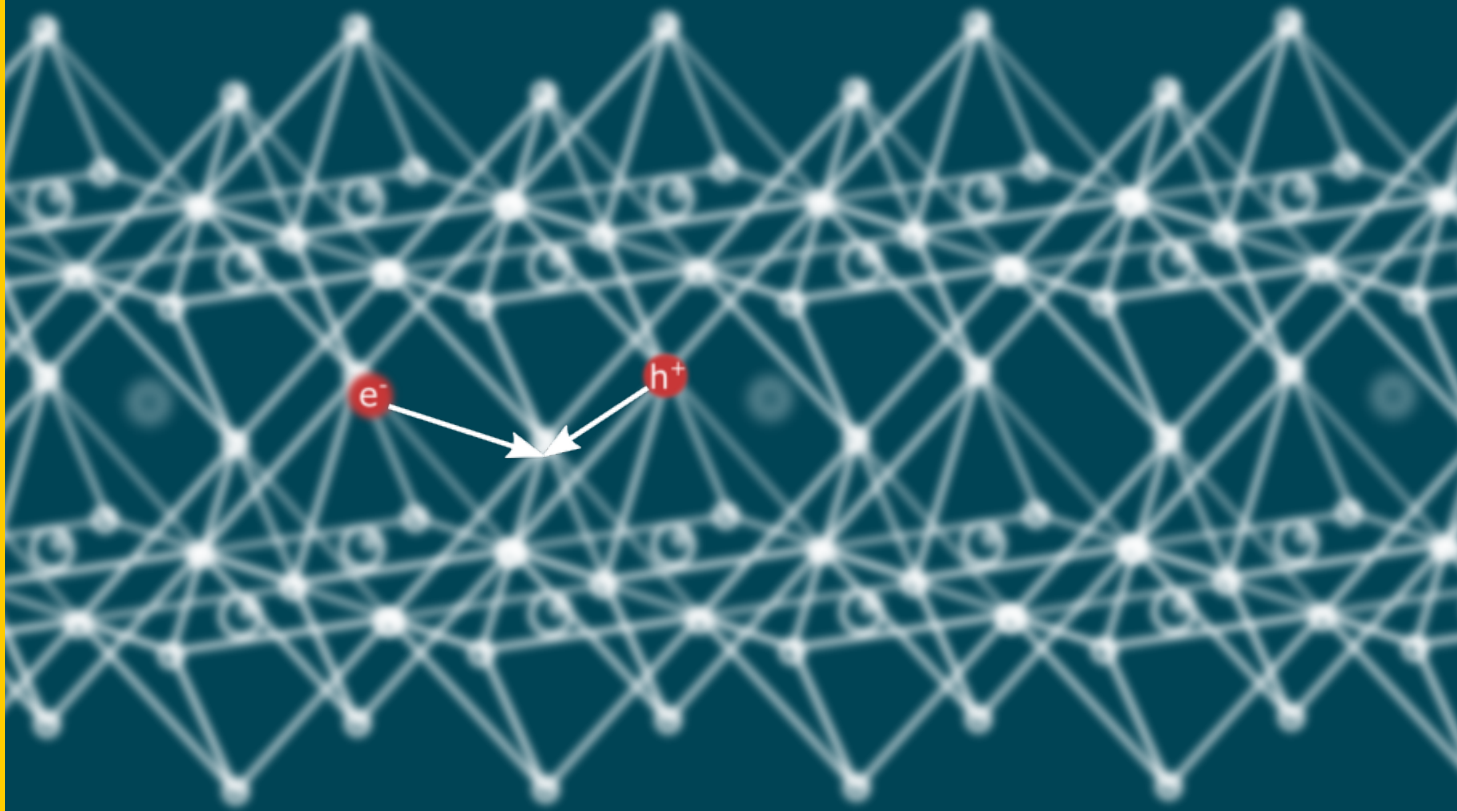




Charge and exciton dynamics in hybrid - organic photovoltaic materials

Kęstutis Budzinauskas



Carrier and exciton dynamics in organic-hybrid photovoltaic compounds

Inaugural-Dissertation
zur
Erlangung des Doktorgrades
der Mathematisch-Naturwissenschaftlichen Fakultät
der Universität zu Köln

vorgelegt von
Kestutis Budzinauskas
aus Vilnius, Litauen

Köln
September, 2021

Gutachter: Prof . Dr. Ir. P.H.M. Van Loosdrecht
Gutachter: Prof . Dr. Ir. P.H.M. Van Loosdrecht
Vorsitzender der Prüfungskommission: Prof. Dr.

Tag der mündlichen Prüfung 01. September 2021

Dedicated to Vaiva and Jonas

Contents

1	Fundamental properties of organic and hybrid semiconducting materials	3
1.1	Introduction	4
1.1.1	Ultrafast processes in semiconductors	4
1.1.2	Types of modern photovoltaics cells	7
1.2	Organic semiconducting materials	9
1.2.1	Fundamentals of organic solar cells	10
1.2.2	Charge transfer mechanism in organic compounds	11
1.2.3	Optical transitions in organic compounds	12
1.3	Fundamental properties of hybrid perovskite materials	15
1.3.1	High optical absorption in hybrid perovskites	16
1.3.2	Electronic properties of hybrid perovskites	18
1.3.3	Excitons in hybrid perovskites	21
1.4	Tailoring halide perovskite properties by chemical engineering	21
1.4.1	Formamidinium and methylammonium cations	22
1.4.2	Incorporation of cesium atoms	23
1.4.3	Effect of bromine substitution on the electronic structure of hybrid perovskite	24
1.4.4	Guanidinium and domain wall passivation	25
2	Experimental methods	34
2.1	Introduction to ultrafast spectroscopy	35
2.1.1	Transient absorption	35
2.1.2	Supercontinuum generation	37
2.1.3	Transient absorption method	38
2.1.4	Experimental layout	39
2.1.5	Types of transient spectral fingerprints	40
2.2	Photoemission spectroscopy	44
2.2.1	Two photon photoemission (2PPE)	47

2.2.2	Experimental details of 2PPE spectroscopy	48
Main goals and achievements		50
3	Hole diffusion in MAPbI₃ films	51
3.1	Introduction	52
3.1.1	Experimental setup	52
3.2	Experimental results and discussion	53
3.3	Conclusions	59
4	Charge carrier recombination dynamics in quadruple cations perovskites	62
4.1	Experimental results and discussion	63
4.1.1	Optical properties of mixed halide 4 cation perovskite	63
4.2	Micro to nanosecond dynamics of excited electrons in quadruple cations perovskite	64
4.2.1	Optical characterization	69
4.2.2	Transient absorption and photoemission	70
4.2.3	Conclusions	73
5	Molecular H-aggregate formation in merocyanine chromophores	79
5.1	Optical absorption properties of investigated merocyanine films	81
5.1.1	Merocyanine molecules and their vibronic properties	82
5.1.2	Photoluminescence properties of merocyanine dyes	83
5.1.3	Solvatochromic behavior of merocyanine dyes	85
5.1.4	H-aggregation	87
5.2	H-aggregation of merocyanines in different solvents	89
5.3	H-aggregation in merocyanine films	91
5.3.1	Use of PC ₆₁ BM molecules to tailor H-aggregation in merocyanine films	93
5.4	Conclusions	94
5.4.1	Collaborations	94
6	Charge transfer state formation in merocyanine:PC₆₁BM	98
6.1	Photophysical properties of PC ₆₁ BM	100
6.2	Charge transfer state formation in merocyanine films	103
6.2.1	Computational studies of merocyanine packing using DFT	107
6.2.2	Merocyanine:PC ₆₁ BM device characterization	109
6.3	Conclusions	113

6.3.1 Collaborations	113
Executive Summary	117
List of Publications	118
Offizielle erklärung	119

List of abbreviations

MAPbI₃ - methylammonium lead iodide
PC₆₁BM-[6,6]-Phenyl-C₆₁-butyric acid methyl ester
MA - methylammonium
FA - formamidinium
GA - guanidinium
TA - transient absorption
 E_g - band gap
SRH - Shockley-Reed-Hall recombination
AM - air mass
NIR - near infrared
GaAs - gallium arsenide
SQ - Shockley-Queisser
CdTe - cadmium telluride
CIGS - copper indium gallium arsenide
HOMO - highest occupied molecular orbital
LUMO - lowest unoccupied molecular orbital
DFT - density functional theory
TDDFT - time dependent density functional theory
CT - charge transfer
HP - hybrid perovskite
JDOS - joint density of states
DOS - density of states
CBM - conduction band minimum
VBM - valence band maximum
SOC - spin-orbit coupling
YB:KGW - ytterbium doped potassium gadolinium tungstate KGd(WO₄)₂
FWHM - full width at half maximum
SE - stimulated emission
BGR - band gap renormalization
UPS - ultraviolet photoelectron spectroscopy
XPS - X-ray photoelectron spectroscopy
2PPE - two photon photoemission
HRTEM - high resolution tunneling electron microscopy
ITO - indium tin oxide
DMF - dimethylformamide
CM - center of mass

tr-PES - time resolved photo emission
NMR - nuclear magnetic resonance
PBF - photoinduced band filling
PCE - power conversion efficiency
FF - fill factor
BHJ - bulk heterojunction
ICT - intermolecular charge transfer
IP - ionization potential
OFET - organic field effect transistor
XRD - X-ray diffraction
SER - Secondary electron replica

Chapter 1

Fundamental properties of organic and hybrid semiconducting materials

This chapter introduces fundamental and optoelectronic properties of organic and hybrid semiconducting materials which are promising to be used for solar cells. Focus of this chapter is optical excitations in organic and hybrid semiconductor materials.

1.1 Introduction

1.1.1 Ultrafast processes in semiconductors

Ultrafast processes play a very important role in the field of photovoltaics. In conventional semiconductors which are used for solar cell applications, only a fraction of absorbed photons lead to free carrier generation because of various ultrafast processes involved (figure 1.1). Following the absorption of a photon in a conventional semiconductor electrons and holes undergo a series of temporal and spatial evolution with energy losses occurring at each step. These microscopic processes largely influence the macroscopical properties of photoexcited semiconductor and play a crucial role for the efficiency in a solar cell material. Typical dynamical mechanisms following the photoexcitation are shown in a chronological order in Table 1.1[1]. The

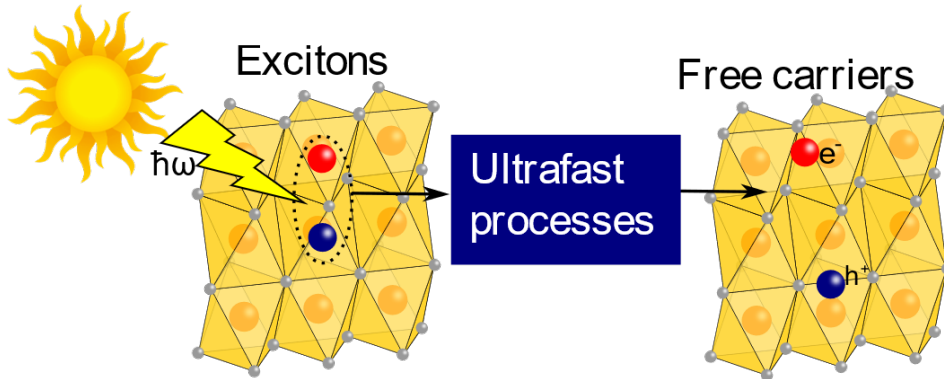


Figure 1.1: A sketch depicting the conversion of absorbed photons to excitons and free charges via ultrafast processes in photovoltaic material.

fastest of these processes is the so-called carrier-carrier scattering and it depends on the excitation density. This process is responsible for a quick momentum redistribution of excited species. Intervalley scattering is usually driven by the emission of phonons with large wave-vector and is causing carriers to be scattered between various side valleys in the Brillouin zone. In addition to the intervalley scattering, carriers can decay to the bottom of the same valley through the emission of high energy, small wave-vector phonons. Eventually all emitted phonons decay to lower energy phonons. Finally, electrons and holes diffuse spatially. The carrier diffusion is caused by the density gradient and causes carriers to move randomly if no electrical field is applied. This random motion does not yield a net current and cause the carrier density to become uniform. The timescale of the diffusion process strongly depends on macroscopical properties of the materials, such as carrier mobility and can be strongly influenced by morphology and structural defects of the material.

Figure 1.2 depicts major dynamical processes following the excitation of a direct

Table 1.1: Scattering and recombination processes following the photoexcitation in a conventional semiconductor.

Process	Timescale
Carrier-carrier scattering	$10^{-15} - 10^{-12}$ s
Intervalley scattering	$\geq 10^{-14}$ s
Intravalley scattering	$\approx 10^{-13}$ s
Carrier-Optical phonon interaction	$\geq 10^{-12}$ s
Optical phonon-acoustic phonon interaction	$\approx 10^{-11}$ s
Carrier diffusion	$\geq 10^{-11}$ s
Auger recombination	$\approx 10^{-10}$ s
Radiative recombination	$\geq 10^{-9}$ s
Lattice heat diffusion	$\approx 10^{-8}$ s

semiconductor. It is assumed that the excitation is done using a monochromatic polarized light assuming an ultrashort pulse duration and the photon energy ($\hbar\omega_0$) higher than the bandgap (E_g). Initial excitation with a short pulse creates a narrow distribution of electron and holes in energy and momentum space (figure 1.2a).

These photoexcited carriers interact both elastically and inelastically and in the first tens of femtoseconds after the photoexcitation, the momentum gets randomized. Initially electrons and holes are considered as separate systems with an individual energy and momentum distributions. Because of electron-electron and hole-hole interactions, carriers thermalize (establish a carrier temperature) in approximately in 100's of femtoseconds and form a Fermi-Dirac distribution with a specific carrier temperature (figure 1.2b). The carrier temperature of electrons and holes may be different. The temperature of carriers is slowly equilibrating with the lattice temperature through electron - phonon interaction. Because of this interaction, the population of non-equilibrium phonons increases in a picosecond time scale. Finally, the phonon-phonon interaction leads to a slow equilibration of phonons.

Lifetime of carriers in a non-equilibrium state

One of the most important microscopical properties of a good solar cell material is the lifetime of the photoexcited carriers. The long lifetime of carriers means a higher probability for the photogenerated charges to reach the extraction electrode and generate current. Few 100's femtoseconds after the photoexcitation when carriers have thermalized, electrons have reached the bottom of the conduction band and hole the top of the valence band system is in a non-equilibrium state and carrier can

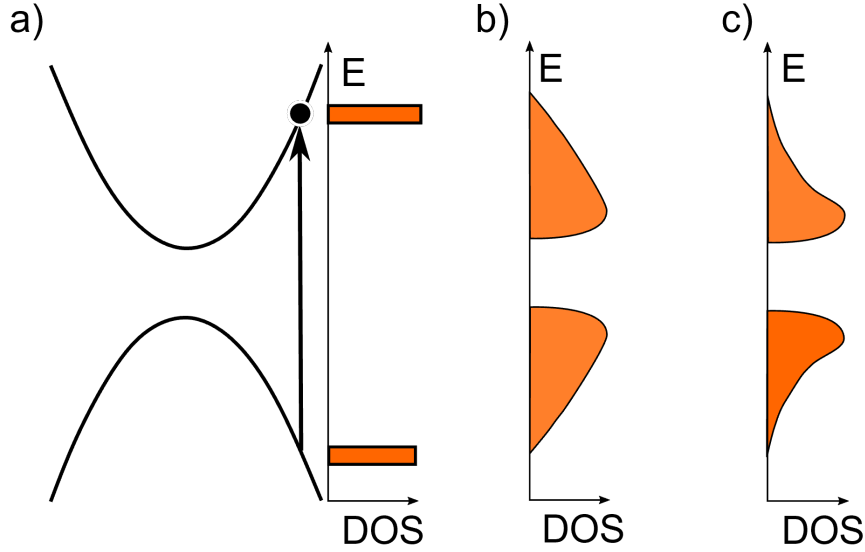


Figure 1.2: Generalized dynamical processes and DOS (density of states) formation in a conventional, direct gap semiconductor, following the photoexcitation; a) photoexcitation, b) carriers form a Fermi-Dirac distribution, described by the carrier temperature and quasi Fermi level; c) Equilibration of carriers through multiple phonon scattering, decreasing the carrier temperature.

be transferred from band to band. The total carrier lifetime in the non-equilibrium state can be expressed as the sum of different recombination rates τ . It contains radiative, Auger and non-radiative (Shockley-read type) recombination channels.

$$\tau^{-1} = \tau_{SRH}^{-1} + \tau_{rad}^{-1} + \tau_{auger}^{-1} \quad (1.1)$$

here τ_{SRH}^{-1} is the Shockley-Reed-Hall (SRH) recombination rate, τ_{rad} is the band to band radiative recombination and τ_{auger} correspond the Auger type recombination. The so-called band-to-band recombination process happens when the electron and hole recombine by releasing a photon with energy equal of the excess energy. The band-to-band recombination rate at high excitation densities can be expressed as:

$$\tau_{rad} \approx \frac{1}{B_r \Delta n} \quad (1.2)$$

here B_r is the radiative recombination coefficient and Δn corresponds to excess electron density. From this equation one can see that the radiative recombination rate has a linear dependence to excitation density. The so called SRH and Auger recombination processes are nonradiative in nature. In the SRH recombination (also called a *trap assisted recombination*) electron and hole recombine via a defect state and the excess energy is released through one or multiple phonon emission events.

The lifetime of SRH recombination at intermediate temperatures can be expressed as:

$$\tau_{SRH} = \frac{N_c}{\tau_{p0}n_0e^{-E_t/k_B T}} \quad (1.3)$$

N_c is the intrinsic carrier concentration, τ_{p0} represents the intrinsic lifetime of holes, n_0 is the equilibrium concentration of electrons and E_t is the defect energy level. Auger recombination is a three-particle process. In this process, the excess energy is being released not by the photon emission, instead it is absorbed by either the electron or the hole, putting the carrier in to higher excited state. All aforementioned scattering and recombination mechanisms lay the foundations of the charge transport properties in solar cell materials and must be well understood. In our study this is done by implementing the ultrafast spectroscopy techniques.

1.1.2 Types of modern photovoltaics cells

Solar cells are electronic devices which can convert light to electric energy. Concerns on the high level of CO_2 emission and the associate climate change has fueled research on solar cells and other renewable energy sources in recent decades. Every alternative energy source has its pros and cons. For solar energy technologies, the advantage is that the solar energy is non-exhaustive, and it can be used at almost every geographical location on the planet. Depending on the angle of the incoming sun and atmospheric circumstances, the average solar energy incidence typically is about 1 kW/m² [2]. Such a diluted energy density requires to cover a large area with high efficiency solar cells to meet world's energy consumption needs.

The so-called photo voltaic effect was first introduced by Henri Becquerel in 1839 using an electrochemical cell. Modern solar cells use the concept of a p-n junction, which was first introduced by Russel Ohl at Bell laboratories in 1939 using crystalline silicon. This type of junction is created at the interface between n type and p type semiconductors. Due to diffusion of electrons and holes, a buildup of charges at the p-n junction is responsible for a built-in electrostatic gradient. This electrostatic gradient is causing a carrier drift process, in the direction opposite of carrier diffusion across the p-n junction which in turn causes the formation of a so-called space charge region. In a typical p-n junction electron- hole pairs are generated when the incident photon energy is higher than the band gap energy of the material and the current is flowing due to a built-in electrostatic potential. The research of solar technology led to a drastic increase in the efficiencies of a single junction solar cells (where only one p-n junction is used) of up to 26.7% [3]. The real limitation for the efficiency of a photovoltaic device however is an intrinsic one and is

caused by thermodynamics of a cell. This limit is called Shockley–Queisser limit and this theoretical limit for a single junction solar cell device is 33.7%. It is calculated assuming a perfect, non-concentrated AM (air mass) of 1.5 solar spectrum with a material band gap of 1.34 eV under illumination of 1 sun (1 kW/m^2). It is assuming that the carrier recombination term is exponentially dependent on the temperature of a working cell [4].

One of the most used technologies in photovoltaics is based on crystalline and polycrystalline inorganic materials. By far the most used material in this field is crystalline silicon (c-Si) which has a band gap of 1.1 eV. The solar absorption of c-Si based p-n junction cells covers the visible and NIR part of the solar radiation. Crystalline silicon is usually grown as an ingot using the Czochralski method. These ingots are cut into wafers of $160 - 240 \mu\text{m}$ thickness which are used in photovoltaic devices. For cost reduction reasons, polycrystalline silicon is also often used as a material for solar cells. It is produced by a chemical purification method (called Siemen’s method). This second type of silicon is more cost effective because of the simple production process, but monocrystalline silicon is a leader in silicon industry with 26.7% efficiency [5].

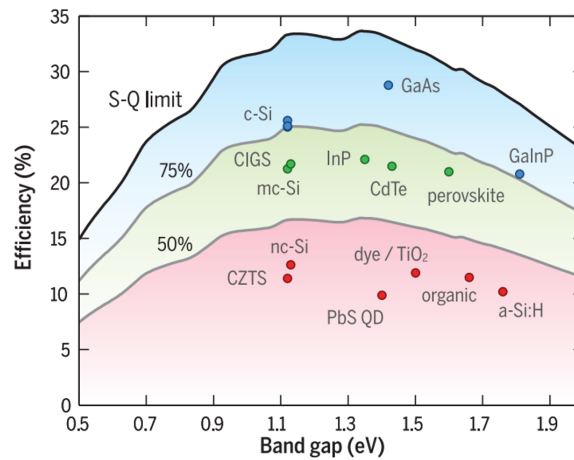


Figure 1.3: Efficiency for different types of perovskite solar cells compared to the theoretical Shockley–Queisser (SQ) efficiency limit. 75% of SQ is shown in yellow and 50% in red. Reproduced from [6].

For applications with a very high efficiency requirements, crystalline GaAs (Gallium Arsenide) solar cells are being used. It is a III-V type semiconductor material with a direct band gap of 1.44 eV. It is superior to silicon based solar cells in terms of its efficiency (28.8%) [7]. However due to the expensive technology, it is used only in space industry in a form of a multi-junction solar cells.

Other classes of modern photovoltaics include thin film solar cells, where an ac-

tive film with a typical thickness ranging from nm to μm is deposited on a flexible substrate. Commercially available thin films solar cells are based on: CdTe (cadmium telluride), CIGS (copper indium gallium selenide) and amorphous silicon. This technology allows to have flexible, semitransparent solar cells. These types of cells usually are cheaper than conventional cells based on crystalline silicon but do have multiple drawbacks. Thin films CdTe contains toxic Cadmium, even though they have a relatively high efficiency of up to 20% [8]. CIGS based cells have a lack of scalability and are not as efficient as other thin films photovoltaics. Laboratory CIGS type single cells show an efficiency of 21.7%; in large area cells a 13% efficiency is reported [8]. This decrease is due to technological challenges in large area CIGS device manufacturing.

To reduce the average price of photovoltaics in recent decades organic and hybrid solar cells were introduced. Advantage of organic solar cells is potentially cheap and easy low temperature processing and versatility in terms of chemical optimization. However organic solar cells lag in efficiency primarily due to the large disorder in these systems which for instance substantially limits the carrier mobility. Hybrid materials combine the best properties of organic and inorganic semiconductors: they can be processed at low temperature and show a high degree of crystallinity giving rise to good charge transport properties. These types of semiconductors are in the early stages of development and have a large future potential. In the remainder of this chapter some key properties of organic and hybrid semiconductors used for solar cell applications will be introduced.

1.2 Organic semiconducting materials

Organic solar cells were introduced with the goal to have a solar cell technology for large scale power generation using environment friendly materials with unlimited availability. Materials which are used in organic optoelectronics are less expensive compared to traditional silicon-based technology, have a large absorption coefficient in the visible spectral range, and are potentially harmless to the environment. Most of the materials in organic electronics can be processed at low temperature on flexible surfaces, allowing large scale printing technology to be used [9, 10].

One of the most common architectures for organic solar cells is the so called donor: acceptor structure, where a bulk heterojunction between electron donating and electron accepting molecules is formed [11]. Free charges in these bulk heterojunctions are formed through intermediate charge transfer excitons. This is a necessary step in organic semiconductors since the exciton binding energies are

larger than kT (product of the Boltzmann constant and the temperature) strongly suppressing thermal dissociation. The field of organic solar cell technology, unlike widespread use of organic LED's in smartphones and TV-screens, has so far not found widespread applications, partially due to the still relatively low efficiency (7.9% in polymer based tandem cells) and also due to the long time stability issues [12].

1.2.1 Fundamentals of organic solar cells

The field of organic semiconductors started with a ground breaking work of Shirakawa, MacDiarmid, and Heeger, who have shown that conductivity in organic polymers (such as polyacetylene) can be controlled through a doping process [13]. For this discovery, all three authors have been awarded with a Nobel prize in chemistry in 2000. This finding led to the use of conductive polymers as photo-receptors in the field of xerography. The interest in undoped polymers and molecules has risen in the 1980's after a first bulk heterojunction solar cells was demonstrated [14]. Other pioneering research demonstrated a thin film conducting polymer and oligomer based transistor [15–17] and finally high performance electro-luminescence in organic diodes of vacuum evaporated molecules and polymer films was demonstrated in the late 80's [18, 19].

Most used organic polymers and molecules are in fact insulating because of the nature of their molecular orbitals. These compounds have σ type carbon bonding. Organic compounds which are used in organic semiconductors, however, have conjugated π type molecular bonds. The ground state electronic configuration of carbon is $(1s^2)(2s^2)(2p_x^1)(2p_y^1)$, the one s and two p -orbitals can combine and form so called sp^2 hybridized orbitals with a configuration of $1s^2(2sp^2)^3(2p)$. π type bonds are formed by the p_z orbitals of sp^2 hybridized carbon atoms in the molecule. (figure 1.4). The example of two different bonding types in ethene molecule is shown in figure 1.4. The σ bond is formed between sp^2 hybridized carbon orbitals when their electronic cloud overlap in head-on orientation. The π bond in ethene molecule is formed between unhybridized p_z orbitals. The filled π band is called the highest occupied molecular orbital (HOMO) and the empty π^* band is called lowest unoccupied molecular orbital (LUMO). Usually transitions from HOMO to LUMO are in the energy range from 1.5 eV to 3 eV giving rise the optical absorption in the visible range of the spectrum. Conjugated molecules offer a great tunability because their photophysical properties can be tuned by changing the conjugation length or adding/removing electron donating or withdrawing moieties to the molecule or polymer.

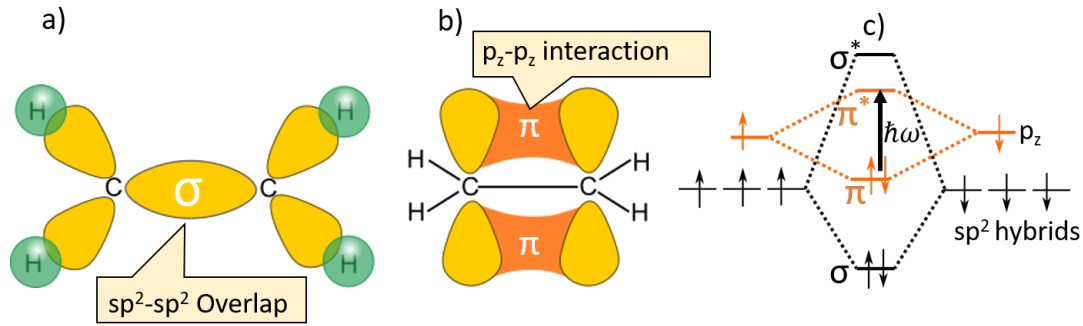


Figure 1.4: Schematic diagram of the molecular orbitals in Ethene molecule. It forms a) σ bonds between sp^2 hybridized carbon orbitals and b) π bonds between hybridized $2p_z$ orbitals, c) energy levels of corresponding bonding and antibonding levels of π and σ .

1.2.2 Charge transfer mechanism in organic compounds

The absorption of a photon in a semiconductor creates an electron in the conduction band and a hole in the valence band. Since they are created at the same point in space and have opposite charges, they attract each other through Coulomb interaction and form a bound state - the exciton. Unlike in conventional semiconductor materials, photoexcitation in organic semiconductors leads to strongly bounded exciton (Frenkel exciton). This is mainly due to the low dielectric constant of organic materials, causing strong Coulomb interactions between electron and hole with a coupling strength usually much larger than kT . The typical radius of a Frenkel exciton in an organic medium is in range of 10's of Angstroms, so excitons are on one lattice site [20]. The coupling between electron and hole lowers the overall energy of the system and exciton is frequently the lowest energy excitation in organic materials.

Excitons can be well described by a hydrogen model. The main differences with the hydrogen atom are the screening of the coulomb interaction by the environment and the fact that one must take the electron and hole masses properly into account. This leads to a series of quantized exciton levels with energy:

$$E(n) = -\frac{\mu}{m_0} \frac{1}{\epsilon_r^2} \frac{R_H}{n^2} = -\frac{R_x}{n^2} \quad (1.4)$$

where the R_H is the Rydberg's constant of 13.6 eV.

The small distance between electron and hole in a Frenkel exciton gives a strong wave-function overlap between the two particles and increases the probability of recombination. Also, the localized nature of Frenkel excitons does not allow a band-to-band type of transport in molecular solids, site to site hopping becomes the domi-

nant transport process. Typically, without an external mechanism to dissociate the exciton to free charges, the lifetime of the Frenkel exciton in organic compounds can vary from 100 ps to few ns.

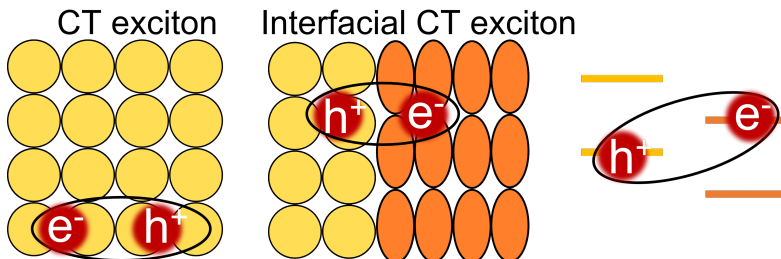


Figure 1.5: Schematics of CT excitons in molecular solids. Frenkel excitons are typically localized on one molecule where as CT excitons are delocalized on two or more molecules. When CT exciton is formed on the surface between the two different molecules it is called an interfacial charge transfer exciton.

One way to overcome the limitation of a strongly bound exciton in organic compounds is by utilizing a so-called donor/acceptor interface. Using two organic compounds with different electron work functions creates an energy offset at the interface between two materials like in a heterojunction and this energy offset between work functions is the driving force for the exciton dissociation process into free charges. In such devices, excitons can travel until the recombination process happens and a typical diffusion distance in organic compounds is in the scale of tens of nanometers. However, for efficient light harvesting, hundreds of nanometers of the material thickness is required. To overcome these two conflicting requirements, bulk heterojunctions are used, where donor and acceptor molecules are mixed together, creating a continuous network of heterojunctions in the bulk of the material so that excitons can be split more efficiently [21]. An important ingredient in the exciton splitting in organic semiconductors is the intermediate state between bound Frenkel exciton and free charges. It is called charge transfer exciton which is an intermediate case between delocalized Wannier type exciton and localized Frenkel exciton. In the CT exciton electron and hole are delocalized on different molecules and the state has a partially ionic character.

1.2.3 Optical transitions in organic compounds

Generally, in organic compounds, the wavefunction, describing the nuclear and electronic subsystem can be separated. This is valid only when the mass of nucleus is larger than the electron mass, which is the case in all compounds. According to the Born-Oppenheimer approximation, the electron cloud responds to the motion

of nuclei simultaneously and the total wavefunction can be described as product of electronic and nuclear motion terms

$$\Psi_{tot}(r_r, \mathbf{Q}_j) \approx \chi_N(\mathbf{Q}_j) \cdot \Psi_{el}(r_i, \mathbf{Q}_j), \quad (1.5)$$

here $\Psi_{tot}(r_r, \mathbf{Q}_j)$ denotes the total wavefunction, $\chi_N(\mathbf{Q}_j)$ describes the nuclear motion and $\Psi_{el}(r_i, \mathbf{Q}_j)$ describes the electronic wavefunction. This allows to separate nuclear and electronic terms.

Electronic transitions from initial to the final state are faster than atomic reorganization time. Meaning that during the photoexcitation the nuclear framework does not change because the typical reorganization time for nuclear framework is in order of 10^{-13} s compared with the typical transition time of 10^{-15} s.

The strength of the optical transition is determined by the transition dipole matrix element:

$$\mu_{fi} = \langle f | \hat{\mu} | i \rangle, \quad (1.6)$$

because of the Born-Oppenheimer approximation, the dipole operator $\hat{\mu}$ consist of the sum over nuclear and electronic coordinates thus both final and the initial states consists of the nuclear $|\nu\rangle$ and electronic $|\epsilon\rangle$ parts. Combining this together, the matrix element becomes:

$$\mu_{fi} = -e \sum_n \langle \epsilon_f | \mathbf{r}_n | \epsilon_i \rangle \langle \nu_f | \nu_i \rangle, \quad (1.7)$$

this equation is particularly important in explaining optical transition in organic materials. Because the intensity of the optical transition is directly proportional to the transition matrix element squared: $|\mu_{fi}|^2$. Then it follows that strength of an optical transition in organic systems is proportional to the overlap integral between the vibrational wavefunction in the initial electronic state $|\nu_i\rangle$ and the vibrational wavefunction in the final electronic state $|\nu_f\rangle$. Thus it can be written that $|\mu_{fi}|^2 \propto \langle \nu_f | \nu_i \rangle^2$ and it is called the Franck-Condon factor. Using this factor, spectroscopic properties and various photophysical processes in organic materials can be explained as it is visualized in figure 1.6.

Using the Franck Condon factor one can show that strong optical transitions occur from where molecular vibrations in the initial and final state are overlapping, and these kind of transitions where vibrational and electronic transitions are coupled together are called vibronic transitions. Electronic transitions in organic compounds are strongly coupled to molecular vibrations. The typical energy of these vibrations

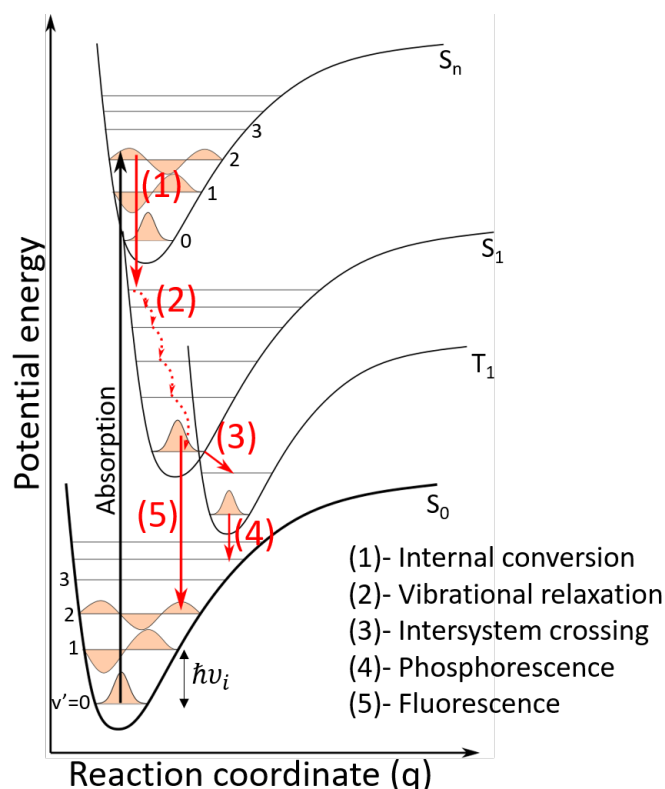


Figure 1.6: Franck-Condon principle in a diatomic molecular system. Absorption from the ground state singlet state S_0 to the higher singlet state S_n appears when their vibrational wavefunctions overlap more significantly. In the illustrated case, the 0-2 vibronic transition occurs, meaning from the zero-phonon level ($\nu' = 0$) to the double phonon level ($\nu'' = 2$). The transition which involves both the electronic and vibrational wavefunctions to overlap is called the vibronic transition. The showed molecular system undergoes an internal conversion (1) from the S_n to the lower singlet state S_1 . The excitation is rapidly decaying to the bottom of the S_1 via phonon emission (vibrational relaxation (2)). System can also undergo an intersystem crossing process (3) and cross from the singlet to the triplet state. The triplet can relax back to the ground state only after the spin flip (Phosphorescence (4)). The singlet state relaxes back to the ground state via fluorescence process (5) to the higher vibrational state (0-2 transition).

is relatively high compared to the room temperature. For example the stretching mode of a carbon double bond in a polymethine is 150 meV, far exceeding the kT energy and according to the Boltzmann distribution, only the lowest vibrational level is populated at room temperature. The Franck Condon principle for a simple diatomic molecule with its potential energy surfaces is illustrated in figure 1.6. The x axis denotes the intermolecular displacement distance and y axis is the potential energy. In the figure the initial state is denoted as S_0 (ground state singlet state) and the final state is shown as S_n (n_{th} singlet state). The shape of the S_0 S_1

and S_n potential surfaces are almost identical, however the excited state is shifted horizontally. This shift is caused by the molecular reorientation which appears because electronic cloud is causing the molecule to reorganize to a new optimal position. The absorption process (figure 1.6) occurs when the the Frank-Condon factors is largest- when electronic and vibrational wavefunctions overlap. In the illustration it is the 0-2 vibronic transition. The used transition notation 0-2 allows to show the vibrational quantum number ν of the initial and final state. After the absorption process carrier rapidly decays to the bottom of the S_n state via *vibrational relaxation* and then to the lower electronic singlet state S_1 via process, called *internal conversion*(process (1) in the figure 1.6). After that, multiple phonon emission (vibrational relaxation) (2) to the bottom of the S_1 level follows. From this level the excitation can undergo the transition to the ground state level (S_0) via fluorescence (5). The fluorescence from the S_1 to the S_0 also follows the intensity of the Franck-Condon factor S . In figure 1.6 maximum vibrational wavefunction overlap and therefore maximum fluorescence intensity is achieved for the 0-3 transition. This shows that in the fluorescence measurements one can probe the vibrational structure of ground state and in the absorption experiment, the vibrational structure of the excited state.

Another important process in photoexcited compounds is the so called *intersystem crossing* (3). This is a non-radiative process between two electronic transitions which involve a change in the spin multiplicity. The intersystem crossing is illustrated in figure 1.6 from the singlet (S_1) to the triplet (T_1) state. The energy of the triplet state is lower compared to the singlet state because the system energy is lowered by the spin flip process. Because of the angular momentum conservation law, triplet state cannot directly decay to the ground state, it must change the spin back to a singlet configuration before decaying. This appears in the *phosphorescence* (4) process and is one of the slowest decay process because of slow probability of a spin flip process.

1.3 Fundamental properties of hybrid perovskite materials

In recent years, a new class of materials for solar cell applications has emerged. These are materials that have both organic and inorganic components and crystallize in a 3D perovskite ABX_3 structure and therefor are called hybrid perovskite (HP) materials. This type of materials derive their name from the structure of the mineral $CaTiO_3$. In this type of materials, the A-site is replaced by organic amine cations

or a combination of organic/ inorganic components. There is a variety of organic and inorganic cations which can be used to form hybrid perovskite crystals on the A-site. Few widely used examples are methylammonium CH_3NH_3 , formamidinium $\text{CH}(\text{NH}_2)_2$, guanidinium $\text{C}(\text{NH}_2)_3$ and cesium (Cs^+). In the ideal cubic structure, the organic cation on the A site has a 12 fold cuboctahedral symmetry. The B-site is typically occupied by lead (Pb^{2+}), tin (Sn^{2+}) or germanium (Ge^{2+}) ions, while the X-site typically has iodide (I^-), bromine (Br^-) or chloride (Cl^-) anions [22]. The variety of constituents make the hybrid perovskites a versatile system in which one can easily tune the (photo-) physical and chemical properties. The structure of a hybrid perovskite is depicted in figure 1.7. The rotation and tilting of $[\text{BX}_6]^{4-}$ polyhedra in perovskites leads to a variety of different crystal polymorphs, such as cubic, orthorhombic, tetragonal, trigonal or monoclinic [23].

The real breakthrough in the hybrid perovskite field happened after the first evidence that hybrid perovskites can be used as solar cell materials both in electrolyte and in solid state forms. This caused a sharp increase of the research in the field concerning the transport, semiconducting and photovoltaic properties of hybrid perovskites.

Typical conventional semiconductors, used in photovoltaic technology such as Si or GaAs are crystals, which are bounded by strong covalent bonds, but hybrid perovskite materials are ionic crystals, exhibiting semiconducting properties. The ionic and semiconducting nature of hybrid perovskites allows tuning of their absorption properties over a wide energy range. In hybrid perovskites this is primarily achieved by chemically changing the composition of the material on the X site of the crystal. By varying the molar ratio between different halides such as I, Br, or Cl the band gap can be tuned continuously.

1.3.1 High optical absorption in hybrid perovskites

One of the most important aspects of this type of material, is their extraordinary absorption properties. Despite solution processing, which results in a quasi-amorphous structure with many structural defects, the absorption spectrum has a steep absorption edge. This sharp absorption edge with an optical gap of 1.6 eV in a traditional methylammonium lead iodide $\text{CH}_3\text{NH}_3\text{PbI}_3$ (known as MAPbI_3) perovskite is well suited as an absorber in solar cell materials as it was shown in the Shockley-Queisser efficiency graph in figure 1.3. These materials are also characterized by good charge transport properties both for electrons and holes, which helps for a more efficient charge extraction in solar cell applications [24]. The carrier diffusion length exceeds $175 \mu\text{m}$ [25–27] with the carrier mobility up to $70 \text{ cm}^2\text{V}^{-1}\text{s}^{-1}$ [28].

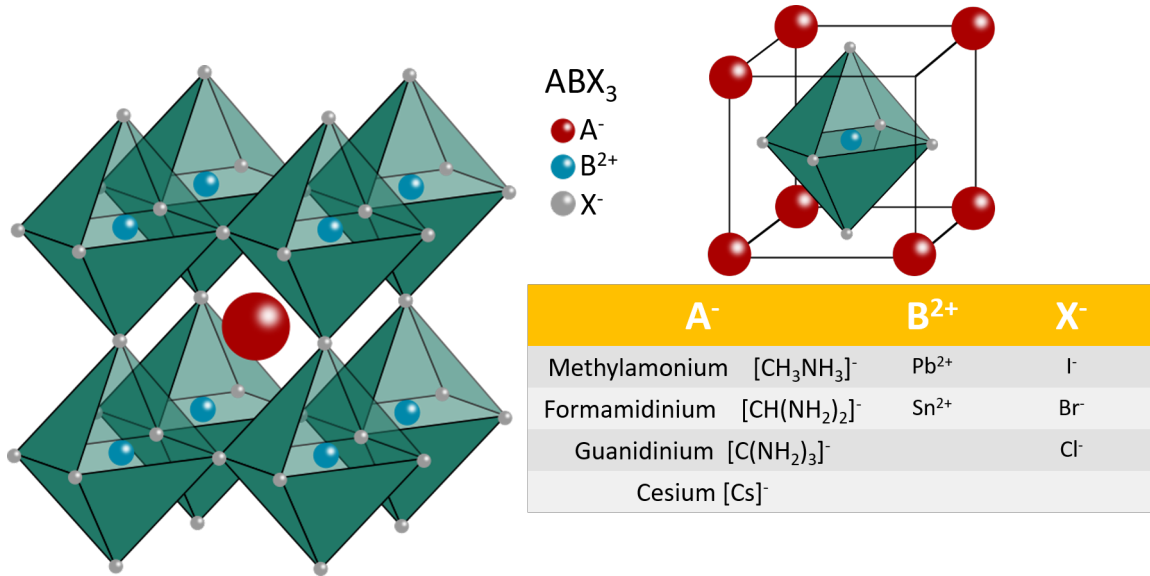


Figure 1.7: An ideal structure of the 3D cubic perovskite. It consists of a network of $[BX_6]^{4-}$ edge sharing octahedra with its unit cell. The structure has an ABX_3 chemical formula. Where in hybrid perovskite A^+ site is typically occupied by an organic cation such as methylammonium (MA^+), formamidinium (FA^+) or guanidinium (GA^+) B^{2+} site is Pb^{2+} and X^- site can be different types of halides such as I^- or Br^- .

In a solar cell configuration, the typical active perovskite layer is 500 nm, which is enough to achieve power conversion efficiencies exceeding 15% and in some cases even 20% [29]. This is not that far from amorphous/crystalline silicon photovoltaics with efficiencies up to 26% [5].

The optical absorption of a semiconductor is typically determined by two fundamental factors: the transition matrix element between valence and conduction bands and the joint density of states (JDOS) between them. The first factor determines the probability of the optoelectronic transition and the JDOS determines the density of possible transitions. These two factors are strongly related to the electronic structures of the material.

The absorption mechanisms for different photovoltaic devices of different generations is sketched in figure 1.8. The fundamental absorption in semiconductors takes place between the band edges of the conduction and valence bands. For silicon, this transition is optically weak since this is an indirect semiconductor. The optical matrix element in this case is typically two orders of magnitude smaller as compared to the direct semiconductor case. To compensate for weak absorption, thick silicon wafers 500 μm are typically used with the charge diffusion length setting the upper limit for the thickness. To overcome this, direct gap semiconductors are preferred such as GaAs or hybrid perovskites, giving large transition matrix elements and

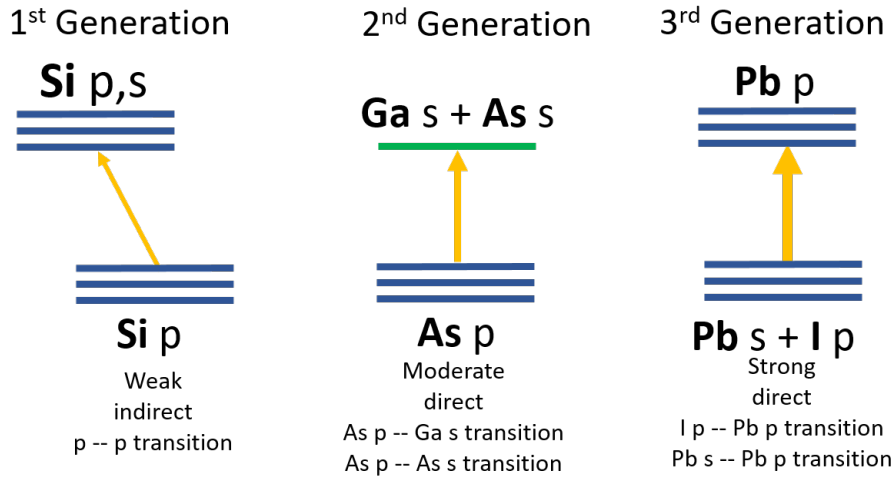


Figure 1.8: Schematics of different mechanisms of optical absorption in semiconductors, used in solar cell applications. Reproduced after [30].

therefore a larger absorption coefficient. The electronic structure of these two semiconductors is different. In case of GaAs, the conduction band edge is derived from delocalized s bands of gallium and arsenic and top of valence band is derived from arsenic p and gallium s orbitals. In a typical hybrid perovskite crystals (MAPbI₃) the bandgap is generally formed between two molecular orbitals Pb(6s)-I(5p) and Pb(6p)-I(5p) [31–34].

1.3.2 Electronic properties of hybrid perovskites

The electronic structure with a bonding diagram of the [PbI₆]⁴⁻ cluster is depicted in figure 1.9. Lowest unoccupied molecular orbitals consist of σ antibonding Pb 6p – I 5s and Pb 6p – I 5p hybridized orbitals. The highest occupied molecular orbitals consist of hybridized Pb 6s – I 5p σ antibonding orbitals. The band structure of the crystal of hybrid perovskite adopts the same electronic characteristic features as the [PbI₆]⁴⁻ octahedra, and it was shown by theoretical calculations that in a typical MAPbI₃ perovskite crystal the valence band consists of approximately 70% I 5p and 25% Pb 6s² orbitals. The conduction band is formed by Pb 6p orbitals hybridized with iodide 5s and 5p orbitals [32, 35].

This type of electronic structure of hybrid perovskites where antibonding orbitals are at the conduction band minimum and the valence band maximum is quite unusual and of great importance for defect tolerance in this material as it is shown in the figure 1.10. In halide perovskites it is expected to have many point defects to be present due to the low temperature, spin coating based preparation techniques

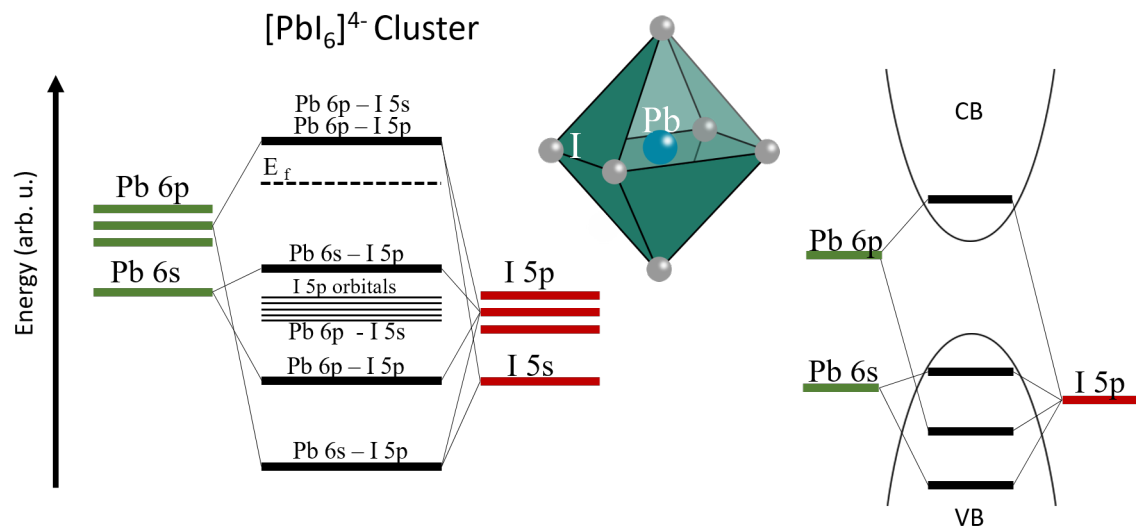


Figure 1.9: Bonding diagram of $[\text{PbI}_6]^{4-}$ cluster and a simplified sketch of optical transition in a typical hybrid perovskite crystal. Reproduced from [36].

but these defects do not limit the performance of solar cell as expected. It turns out many of these point defects are shallow defects which are "inert" and contribute to the good performance of the solar cell device [37].

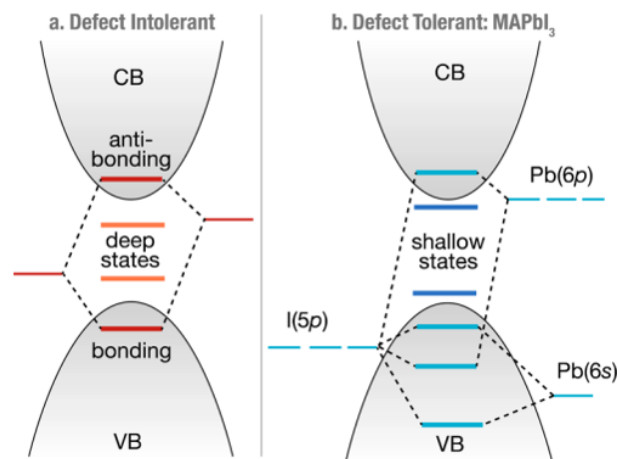


Figure 1.10: a) The electronic structure of a typical III-V, II-VI semiconductor; b) The electronic structure of MAPbI_3 hybrid perovskite. Reproduced from [37].

Theoretical calculations (using DFT (density functional theory)) predicting the band structure in the first Brillouin zone of the high temperature cubic $\text{Pm}3\text{m}$ MAPbI_3 is given in figure 1.11 [38]. Because of the orientational disorder of the organic cations in the crystal structure, most density functional theory computations of hybrid perovskites use the CsPbI_3 structure. As it was mentioned before, conduction and valence bands are formed by I and Pb hybridized molecular orbitals,

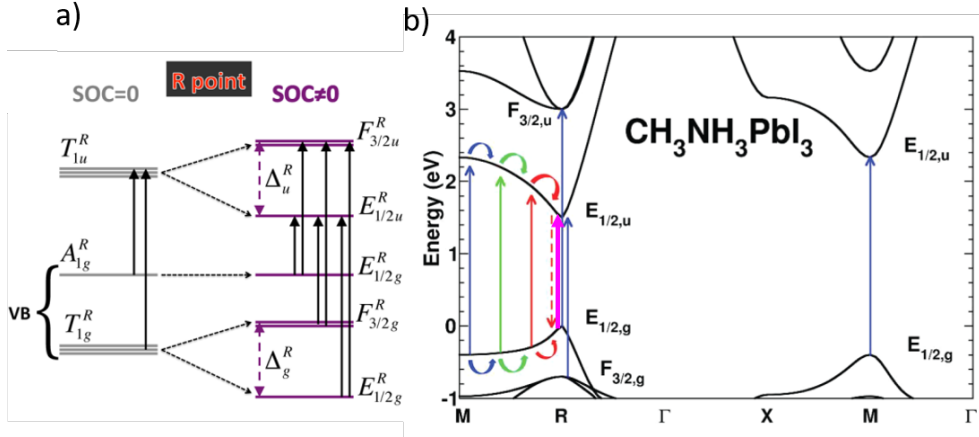


Figure 1.11: a) Schematic energy level diagram for the high symmetry R point of the Pm3m Brillouin zone at the room temperature, SOC denotes the spin orbit coupling b) Electronic band structure of the high temperature cubic phase of MAPbI_3 . Vertical arrows indicate optically allowed transitions. Reproduced from [38].

therefore the Cs^+ cation does not substantially influence the electronic states at the conduction band minimum (CBM) and valence band maximum (VBM). It is clear from the band structure that it has a direct gap at the high symmetry point R of the Brillouin zone. The electronic band structure is also highly impacted by a strong spin orbit coupling, caused by the heavy lead atom in the crystal structure. This interaction is strongest in the conduction band and lifts the degeneracy of the CBM. Due to this interaction, a secondary, conduction band (spin orbit split off band) above the main conduction band appears as illustrated in the figure 1.11.

The symmetry analysis of the electronic states at the R point in the first Brillouin zone can be used to analyze allowed optical transitions in the energy level diagram shown in figure 1.11a. Due to the strong spin orbit coupling (SOC) the T_{1u}^R energy level of the conduction band is split in to doubly degenerate $E_{1/2u}^R$ and a 4-fold degenerate $F_{3/2u}^R$ state. The main optical transition from the ground state is the transition from doubly degenerate $E_{1/2g}^R$ valence band to $E_{1/2u}^R$ conduction band state [38]. This optical transition is also depicted in the calculated band structure diagram in the figure1.11b (pink arrow).

Optically allowed transitions can appear both at the R and M points as well as between the bands along M and R as shown in figure 1.11b. The relatively flat shape of the valence band leads to an enhancement of the JDOS, and hence contributes to the large optical density in the material.

The band structure also plays a role in the carrier transport properties. Based on the deformation potential scattering theory, the carrier mobility is inversely proportional to effective masses of electrons and holes. These are predetermined by the

curvature of the band at conduction and valence edges. Because both the conduction and valence bands consist of two parabolas with similar effective masses (band curvature) a well-balanced transport of holes and electrons in hybrid perovskites can be achieved [38].

1.3.3 Excitons in hybrid perovskites

In hybrid perovskites the initial excitation forms an exciton with a finite coupling energy. From the absorption data of the MAPbI_3 , shown in figure 1.14, a strong excitonic onset at the band gap energy can be observed. The exciton binding energy in polycrystalline MAPbI_3 is currently still discussed in the literature. Reports range from 16 to 60 meV, and seem both to depend on the preparation procedures as well as on the experimental technique [22, 39, 40]. Most importantly, the absorption spectra, measured at room temperature, confirm the existence of excitons with a binding energy similar to kT . According to exciton binding energy estimates in polycrystalline MAPbI_3 the Wannier-Mott model is sufficient to describe excitons in hybrid perovskites. These types of excitons are hydrogen like, combining the electron in the conduction band with a hole in the valence band. Wannier excitons are usually formed in materials with high dielectric screening leading to large exciton radius. Therefore, excited states in hybrid perovskites are more similar in nature to those in inorganic semiconductors such as Si, or GaAs than to those in organic solids.

1.4 Tailoring halide perovskite properties by chemical engineering

Until recently, most reports on hybrid perovskite solar cell materials are concerned with methyl-ammonium lead iodide $\text{CH}_3\text{NH}_3\text{PbI}_3$ (MAPbI_3). Despite high reported efficiencies exceeding the 20% mark [41], hybrid perovskites still have intrinsic disadvantages such as degradation in humid conditions and instability at higher temperatures. Moreover, MAPbI_3 undergoes a reversible structural phase transition from tetragonal to cubic at 55°C and reduces the optical gap, limiting the external quantum efficiency [42]. This is concerning and limiting its application as a solar cell material because it's in the working regime of a working device.

Recent theoretical work by Giorgi *et al.* suggested that guanidinium ($\text{C}(\text{NH}_2)_3$) ions (Ga^+) has nearly zero dipole moment due to its symmetry and could form $\text{GaPbI}_3/\text{FAPbI}_3$ intermediate alloys which are insensitive to ion migration in the

presence of an external electric field, thereby minimizing the usual hysteresis effects in hybrid perovskites [43]. Hysteresis effects in hybrid perovskite are observed with applied electrical field and are caused by ion migration toward electrodes and could increase the recombination rate at perovskite/electrode surface [44]. In a multi crystalline material such as hybrid perovskite, defect density and the recombination through defect states are a major issue. One way to minimize this type of recombination is to reduce the amount of deep defect states. Some authors have show that incorporation of Ga^+ can drastically decrease the concentration of deep defect states leading to better transport properties[45].

1.4.1 Formamidinium and methyammonium cations

Recently, formamidinium ($\text{HC}(\text{NH})_2$)₂ (Fa^+) as an alternative to replace the methyl ammonium cation in hybrid perovskites was suggested by some authors [46, 47]. FAPbI_3 perovskites offer better light harvesting properties because of the reduced optical band gap from 1.55eV in MAPbI_3 to 1.47eV [46]. It was also shown that it has longer carrier diffusion length and better photo-stability [48, 49]. However, there are still some disadvantages with FA cation based perovskites. One of them is the intrinsic structural instability caused by Fa^+ rotation in the unit cell. Due to this, FAPbI_3 crystallizes either into cubic (trigonal P63m1) phase (also known as α - FAPbI_3) or a hexagonal P_{63}mc phase(also known as δ - FAPbI_3), depending on the heat treatment in the growing process [50].

In the literature these two polymorphs are also called black and yellow phases because of drastically different optical properties. The undesired, yellow phase has an indirect optical gap of 2.43eV limiting its use for solar cell applications [51]. This phase is also a non-3D perovskite, which limits charge carrier migrations properties. It is known that under the ambient humid atmosphere FAPbI_3 slowly undergoes a phase transition from the black delta δ - FAPbI_3 to the yellow α - FAPbI_3 polymorph. In addition, the FA cation itself has been reported to dissociate into sym-triazine and NH_3 [52]. To stabilize the black FAPbI_3 phase, a mixed cation system with substitution of FA with MA cations was found to be effective with lower optical gap than δ - FAPbI_3 [53]. This stabilization has been attributed to the higher dipole moment of the MA cations and a resulting stronger interaction with the PbI_6 octahedral cage [54].

Strong interaction with PbI_3 octahedra is driven by hydrogen bonding between iodide ions and ammonium. The number of hydrogen bonds is proportional to the number of hydrogens on the cation and the strength of the hydrogen bonding depends on the dipole moment of the molecule. In the pseudo-cubic α - FAPbI_3

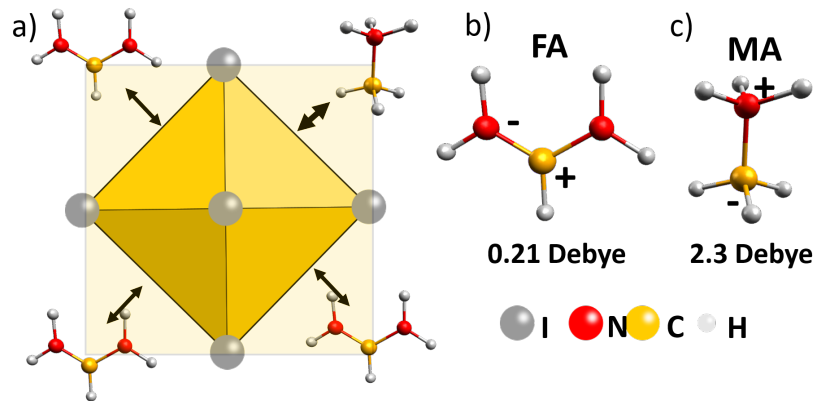


Figure 1.12: a) Sketch of the interaction strength between BX_6 octahedron interaction with organic cation in MA^-/FA^- type perovskite b) formamidinium cation c) methylammonium cation and their dipole moments.

structure there are 4 FA cations, each of them having 5 hydrogen atoms and a dipole moment of 0.21 Debye [55]. Methylammonium on hand has 6 hydrogen atoms and a dipole moment of 2.3 Debye and can stabilize the crystal structure through hydrogen bonding much better [55–57]. In the FA cation, the low dipole moment is thought to originate from the resonance stabilization of the structure, where the charge is evenly distributed over the nitrogen-carbon-nitrogen bond [56], whereas in MA it is concentrated at the Nitrogen atom. Also the larger dipole moment of MA leads to a stronger Coulomb interaction between BX_6 octahedron and organic cation [56].

1.4.2 Incorporation of cesium atoms

Another way to stabilize the crystal structure of $\alpha - FAPbI_3$ perovskite is to replace some of the FA^- molecules with cesium atoms Cs. The ionic radius of cesium is 181 pm which is smaller than that of the of formamidinium (253 pm). Insertion of a smaller cation such as cesium in the hybrid perovskite leads to a reduction of the volume of the A-site surrounded by eight PbI_6 corner sharing octahedra in the unit cell [54, 55, 58].

This leads to an increased interaction between the Pb and I ions in the BX_6 octahedron, similar to FA/ MA mixed cation perovskites [54, 58]. Because of different interatomic interactions between Pb 6s and I 5p hybridized orbitals, the optical gap of the material also is lowered as a function of Cs. Incorporation of cesium also increases photo and moisture stability of the material stabilizing the "black" phase of $FAPbI_3$ [58].

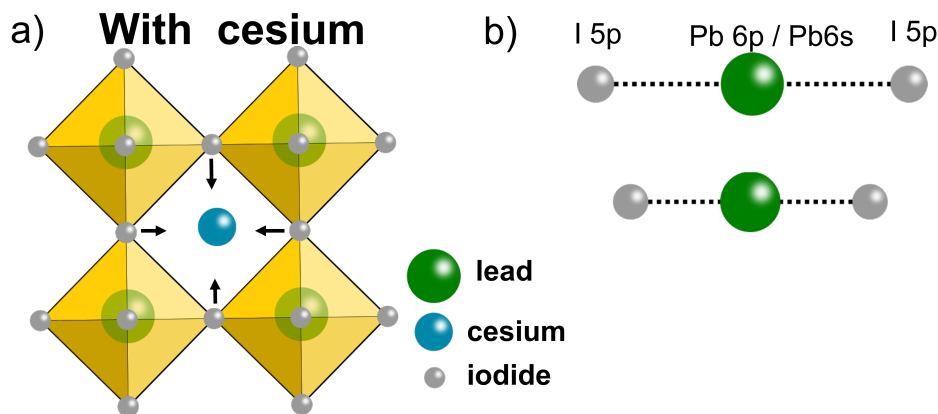


Figure 1.13: Addition of cesium to the crystal structure of the hybrid perovskite make the lattice to contract b) The contraction of the lattice decreases distances between X-site (I) and B-site(Pb) atoms in ABX_3 type perovskite.

1.4.3 Effect of bromine substitution on the electronic structure of hybrid perovskite

Another important element which can be used to tailor the photophysical properties of the hybrid perovskites is the X-site element in the ABX_3 structure. In typical perovskites this site is occupied by mono-valent iodine anions (I^-). Some authors have shown that bromine (ionic radius 1.96 Å versus 2.2 Å for iodine) ions can also be used here, because of the similar ionic radius [59]. Recently it was shown that the iodide bromine mixture alloying can be used to continuously alter the optical gap of a perovskite with the band gap increasing for increasing iodide content [49, 60]. For example, in the Formamidinium (FA) lead iodide bromine compounds $HC(NH_2)_2Pb(I_{1-x}Br_x)_3$, also known as $FAPb(I_{1-x}Br_x)_3$, the band gap energy is changing continuously depending on the content of bromine (see figure 1.14b). For a pure $FAPbI_3$ the band gap is at 1.49 eV (830 nm) and in pure $FAPbBr_3$ it is 2.25 eV (550 nm). The addition of a smaller atom on the X-site in the ABX_3 structure reduces distances between atoms in the crystal lattice, leading to a stronger interaction between the element on the X - site (in this case Br) and B - site (Pb), similar to cesium or MA on the A - site. The introduction of bromine also decrease angles across X-Pb-X direction on the corner sharing BX_6 octahedra [61] and makes the X-Pb-X bonding stronger and increases the band gap.

Bromine also changes the crystal structure of the material. $FAPbI_3$ perovskite undergoes a gradual transition from a cubic structure when it's bromine rich ($x > 0.5$) to tetragonal in the iodide rich case ($y < 0.5$) as shown in figure 1.14b. The tetragonal phase arises from the tilting of octahedra [47].

By adding bromine, the exciton binding also changes substantially and can be

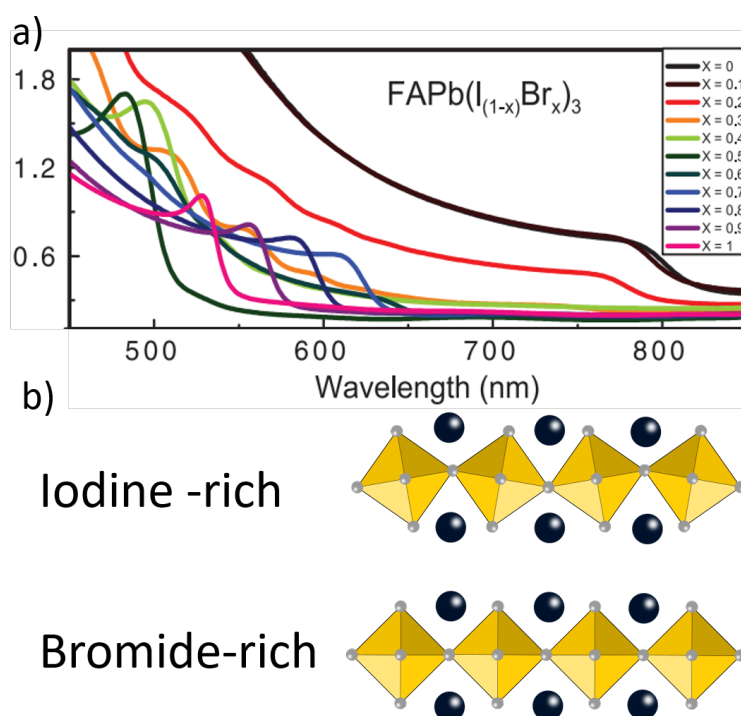


Figure 1.14: a) Absorption edge shift as a function of a molar ratio between iodide and bromine; Reproduced from [49] b) Influence on octahedra angle change BX_6 by replacing iodide with bromine in the hybrid perovskite. The change in the octahedra orientation alters the crystal structure and influences electronic properties of the materials causing the band gap to increase.

seen as a strong excitonic onset at the band gap as shown in figure 1.14a. The excitonic binding energy in $MAPbBr_3$ at room temperature has been estimated to be 70-90 meV [32, 62]. The increase in exciton binding energy for bromine containing hybrid perovskites is assigned to a change in dielectric constant which reduces the Coulomb screening between electron and hole [32].

1.4.4 Guanidinium and domain wall passivation

Hybrid perovskites have a multi domain structure and domain walls can act as defect states and reduce the carrier transport efficiency. The defect passivation at domain boundaries is therefore important and could increase carrier transport properties. One of the materials which is used for defect passivation is guanidinium $C(NH_2)_3$ (GA). Recently it was found that even 0.6wt% GA can drastically improve device efficiency of hybrid perovskite solar cells originating from the reduced trap density, an increased carrier lifetime, as well as an increased grain size [45]. Other authors have shown that incorporation of Ga^+ can drastically increase the defect tolerance (reducing mid gap defect formation and lowers the defect density) of halide per-

ovskites leading to improved transport properties [45]. Defect tolerance is a crucial ingredient for efficiency in hybrid perovskites because low temperature manufacturing can induce high defect density and it is believed that in Ga^+ doped perovskites only shallow defect states are dominant [45].

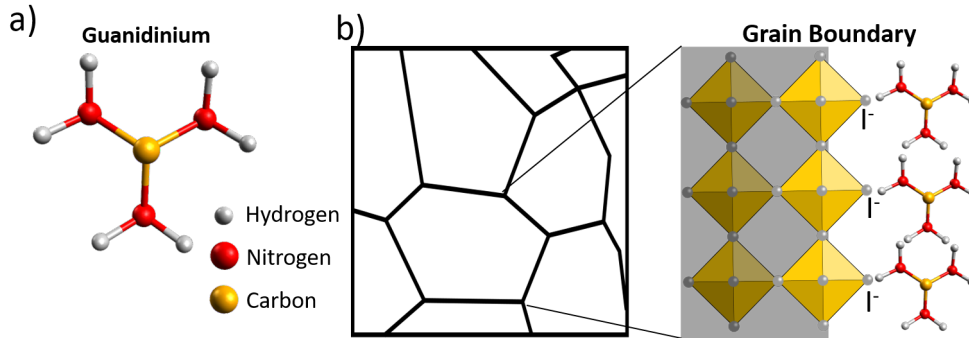


Figure 1.15: a) guanidinium molecular structure b) guanidinium molecules are accumulating on grains and can passivate negatively charged iodide defects on the grain boundaries.

Some authors also suggest that because of the symmetry of amine groups in GA it could form six hydrogen bonds thus greatly enhancing the structural stability. Grain boundaries in hybrid perovskites can have dangling bond defects which usually are negatively charged iodide ions. Hydrogen bonding could affect the partially negatively charged iodide ions on PbI_6^{4-} octahedra, which are exposed at each grain boundary and can interact with partially positively charged ammonium anion of guanidinium. This process should reduce the amount of dangling bonds type of defects at grain boundaries and increase the lifetime of charge carriers [45, 63–65]. The grain boundary passivation also is linked to the fact that according to Goldschmidt tolerance factor GA cannot form a stable 3D perovskite structure. The Goldschmidt tolerance factor is dimensionless quantity which describes the distortion and stability of a crystal structure so incorporation of GA can induce strain and bending of the structure or can be concentrated on grain boundaries [64].

Another important physical property of GA^+ is the diminished dipole moment, compared to the dipole moments of 0.21 D and 2.3 D in FA and MA cations [63, 66]. The close to zero dipole moment can be explained from the symmetry perspective of the molecule (D_{3h} when planar). It has a threefold rotation symmetry, and the electronic cloud is distributed equally along all three C-N bonds. Having a close to zero dipole moment by symmetry is thought to be responsible for reducing the ionic and hysteresis effect in perovskite with guanidinium additives [43, 63].

References

1. Othonos, A. Probing ultrafast carrier and phonon dynamics in semiconductors. *J. Appl. Phys.* **83**, 1789–1830 (1998).
2. Coddington, O., Lean, J. L., Pilewskie, P., Snow, M. & Lindholm, D. A solar irradiance climate data record. *Bull. Am. Meteorol. Soc.* **97**, 1265–1282 (2016).
3. Andreani, L. C., Bozzola, A., Kowalczewski, P., Liscidini, M. & Redorici, L. Silicon solar cells: Toward the efficiency limits. *Adv. Phys. X* **4** (2019).
4. Shockley, W. & Queisser, H. J. Detailed Balance Limit of Efficiency of p-n Junction Solar Cells. *J. Appl. Phys.* **32**, 510–519 (1961).
5. Yoshikawa, K., Kawasaki, H., Yoshida, W., Irie, T., Konishi, K., Nakano, K., Uto, T., Adachi, D., Kanematsu, M., Uzu, H. & Yamamoto, K. Silicon heterojunction solar cell with interdigitated back contacts for a photoconversion efficiency over 26%. *Nat. Energy* **2**, 17032 (2017).
6. Polman, A., Knight, M., Garnett, E. C., Ehrler, B. & Sinke, W. C. Photovoltaic materials: Present efficiencies and future challenges. *Science* **352** (2016).
7. Kayes, B. M., Nie, H., Twist, R., Spruytte, S. G., Reinhardt, F., Kizilyalli, I. C. & Hignashi, G. S. 27.6% conversion efficiency, a new record for single-junction solar cells under 1 sun illumination, 4–8 (2011).
8. Jackson, P., Hariskos, D., Wuerz, R., Kiowski, O., Bauer, A., Friedlmeier, T. M. & Powalla, M. Properties of Cu(In,Ga)Se₂ solar cells with new record efficiencies up to 21.7%. *Phys. status solidi - Rapid Res. Lett.* **9**, 28–31 (2015).
9. Gsänger, M., Bialas, D., Huang, L., Stolte, M. & Würthner, F. Organic Semiconductors based on Dyes and Color Pigments. *Adv. Mater.* **28**, 3615–3645 (2016).
10. Koch, N. Organic Electronic Devices and Their Functional Interfaces. *ChemPhysChem* **8**, 1438–1455 (2007).
11. Chalabi, N. F. & Guen-Bouazza, A. Polymer/fullerene bulk heterojunction solar cells. *EEA - Electroteh. Electron. Autom.* **67**, 5–12 (2019).
12. Meng, L., Zhang, Y., Wan, X., Li, C., Zhang, X., Wang, Y., Ke, X., Xiao, Z., Ding, L., Xia, R., Yip, H. L., Cao, Y. & Chen, Y. Organic and solution-processed tandem solar cells with 17.3% efficiency. *Science* **361**, 1094–1098 (2018).
13. Audenaert, M., Gusman, G. & Deltour, R. Electrical conductivity of I₂-doped polyacetylene. *Phys. Rev. B* **24**, 7380–7382 (1981).

14. Tang, C. W. Two-layer organic photovoltaic cell. *Appl. Phys. Lett.* **48**, 183–185 (1986).
15. Tsumura, A., Koezuka, H. & Ando, T. Polythiophene field-effect transistor: Its characteristics and operation mechanism. *Synth. Met.* **25**, 11–23 (1988).
16. Burroughes, J. H., Jones, C. A. & Friend, R. H. New semiconductor device physics in polymer diodes and transistors. *Nature* **335**, 137–141 (1988).
17. Horowitz, G., Fichou, D., Peng, X., Xu, Z. & Garnier, F. A field-effect transistor based on conjugated alpha-sexithienyl. *Solid State Commun.* **72**, 381–384 (1989).
18. Tang, C. W. & Vanslyke, S. A. Organic electroluminescent diodes. *Appl. Phys. Lett.* **51**, 913–915 (1987).
19. Burroughes, J. H., Bradley, D. D. C., Brown, A. R., Marks, R. N., Mackay, K., Friend, R. H., Burns, P. L. & Holmes, A. B. Light-emitting diodes based on conjugated polymers. *Nature* **347**, 539–541 (1990).
20. Clarke, T. M. & Durrant, J. R. Charge photogeneration in organic solar cells. *Chem. Rev.* **110**, 6736–6767 (2010).
21. Yu, G., Gao, J., Hummelen, J. C., Wudl, F. & Heeger, A. J. Polymer Photovoltaic Cells: Enhanced Efficiencies via a Network of Internal Donor-Acceptor Heterojunctions. *Science* **270**, 1789–1791 (1995).
22. Jena, A. K., Kulkarni, A. & Miyasaka, T. Halide Perovskite Photovoltaics: Background, Status, and Future Prospects. *Chem. Rev.* **119**, 3036–3103 (2019).
23. Glazer, A. M. The classification of tilted octahedra in perovskites. *Acta Crystallogr. Sect. B Struct. Crystallogr. Cryst. Chem.* **28**, 3384–3392 (1972).
24. Miyano, K., Tripathi, N., Yanagida, M. & Shirai, Y. Lead Halide Perovskite Photovoltaic as a Model p – i – n Diode. *Acc. Chem. Res.* **49**, 303–310 (2016).
25. Dong, Q., Fang, Y., Shao, Y., Mulligan, P., Qiu, J., Cao, L. & Huang, J. Electron-hole diffusion lengths > 175 μm in solution-grown $\text{CH}_3\text{NH}_3\text{PbI}_3$ single crystals. *Science* **347**, 967–970 (2015).
26. Stranks, S. D., Eperon, G. E., Grancini, G., Menelaou, C., Alcocer, M. J. P., Leijtens, T., Herz, L. M., Petrozza, A. & Snaith, H. J. Electron-Hole Diffusion Lengths Exceeding 1 Micrometer in an Organometal Trihalide Perovskite Absorber. *Science* **342**, 341–344 (2013).

27. Rehman, W., Milot, R. L., Eperon, G. E., Wehrenfennig, C., Boland, J. L., Snaith, H. J., Johnston, M. B. & Herz, L. M. Charge-Carrier Dynamics and Mobilities in Formamidinium Lead Mixed-Halide Perovskites. *Adv. Mater.* **27**, 7938–7944 (2015).
28. Kim, D. H., Park, J. J. S., Li, Z., Yang, M., Park, J. J. S., Park, I. J., Kim, J. Y., Berry, J. J., Rumbles, G. & Zhu, K. 300% Enhancement of Carrier Mobility in Uniaxial-Oriented Perovskite Films Formed by Topotactic-Oriented Attachment. *Adv. Mater.* **29**, 1–8 (2017).
29. Yang, W. S., Noh, J. H., Jeon, N. J., Kim, Y. C., Ryu, S., Seo, J. & Seok, S. I. High-Performance Photovoltaic Perovskite Layers Fabricated through Intramolecular Exchange. *Science* **348**, 1234–1237 (2015).
30. Yin, W.-J., Yang, J.-H., Kang, J., Yan, Y. & Wei, S.-h. Halide perovskite materials for solar cells: a theoretical review. *J. Mater. Chem. A* **3**, 8926–8942 (2015).
31. Mosconi, E., Amat, A., Nazeeruddin, M. K., Grätzel, M. & De Angelis, F. First-principles modeling of mixed halide organometal perovskites for photovoltaic applications. *J. Phys. Chem. C* **117**, 13902–13913 (2013).
32. Tanaka, K., Takahashi, T., Ban, T., Kondo, T., Uchida, K. & Miura, N. Comparative study on the excitons in lead-halide-based perovskite-type crystals $\text{CH}_3\text{NH}_3\text{PbBr}_3$ $\text{CH}_3\text{NH}_3\text{PbI}_3$. *Solid State Commun.* **127**, 619–623 (2003).
33. Even, J., Pedesseau, L., Jancu, J. M. & Katan, C. Importance of spin-orbit coupling in hybrid organic/inorganic perovskites for photovoltaic applications. *J. Phys. Chem. Lett.* **4**, 2999–3005. arXiv: arXiv:1309.4215v1 (2013).
34. Brivio, F., Walker, A. B. & Walsh, A. Structural and electronic properties of hybrid perovskites for high-efficiency thin-film photovoltaics from first-principles. *APL Mater.* **1**, 10–15. arXiv: 1309.4215 (2013).
35. Yin, W. J., Shi, T. & Yan, Y. Superior photovoltaic properties of lead halide perovskites: Insights from first-principles theory. *J. Phys. Chem. C* **119**, 5253–5264 (2015).
36. Brandt, R. E., Stevanović, V., Ginley, D. S. & Buonassisi, T. Identifying defect-tolerant semiconductors with high minority-carrier lifetimes: Beyond hybrid lead halide perovskites. *MRS Commun.* **5**, 265–275 (2015).

37. Brandt, R. E., Poindexter, J. R., Gorai, P., Kurchin, R. C., Hoye, R. L., Nienhaus, L., Wilson, M. W., Polizzotti, J. A., Sereika, R., Žaltauskas, R., Lee, L. C., Macmanus-Driscoll, J. L., Bawendi, M., Stevanović, V. & Buonassisi, T. Searching for "defect-Tolerant" Photovoltaic Materials: Combined Theoretical and Experimental Screening. *Chem. Mater.* **29**, 4667–4674 (2017).
38. Even, J., Pedesseau, L., Katan, C., Kepenekian, M., Lauret, J. S., Saponi, D. & Deleporte, E. Solid-state physics perspective on hybrid perovskite semiconductors. *J. Phys. Chem. C* **119**, 10161–10177 (2015).
39. Zhao, Z., Chen, X., Wu, H., Wu, X. & Cao, G. Probing the Photovoltage and Photocurrent in Perovskite Solar Cells with Nanoscale Resolution. *Adv. Funct. Mater.* **26**, 3048–3058 (2016).
40. Kanemitsu, Y. Luminescence spectroscopy of lead-halide perovskites: materials properties and application as photovoltaic devices. *J. Mater. Chem. C* **5**, 3427–3437 (2017).
41. Jung, H. S. & Park, N. G. Perovskite solar cells: From materials to devices. *Small* **11**, 10–25 (2015).
42. Quarti, C., Mosconi, E., Ball, J. M., D’Innocenzo, V., Tao, C., Pathak, S., Snaith, H. J., Petrozza, A. & De Angelis, F. Structural and optical properties of methylammonium lead iodide across the tetragonal to cubic phase transition: implications for perovskite solar cells. *Energy Environ. Sci.* **9**, 155–163 (2016).
43. Giorgi, G., Fujisawa, J.-I., Segawa, H. & Yamashita, K. Organic–Inorganic Hybrid Lead Iodide Perovskite Featuring Zero Dipole Moment Guanidinium Cations: A Theoretical Analysis. *J. Phys. Chem. C* **119**, 4694–4701 (2015).
44. Zhang, F., Ma, W., Guo, H., Zhao, Y., Shan, X., Jin, K., Tian, H., Zhao, Q., Yu, D., Lu, X., Lu, G. & Meng, S. Interfacial Oxygen Vacancies as a Potential Cause of Hysteresis in Perovskite Solar Cells. *Chem. Mater.* **28**, 802–812 (2016).
45. Yao, J., Wang, H., Wang, P., Gurney, R. S., Intaniwet, A., Ruankham, P., Choopun, S., Liu, D. & Wang, T. Trap passivation and efficiency improvement of perovskite solar cells by a guanidinium additive. *Mater. Chem. Front.* **3**, 1357–1364 (2019).
46. Koh, T. M., Fu, K., Fang, Y., Chen, S., Sum, T. C., Mathews, N., Mhaisalkar, S. G., Boix, P. P. & Baikie, T. Formamidinium-Containing Metal-Halide: An Alternative Material for Near-IR Absorption Perovskite Solar Cells. *J. Phys. Chem. C* **118**, 16458–16462 (2014).

47. Eperon, G. E., Stranks, S. D., Menelaou, C., Johnston, M. B., Herz, L. M. & Snaith, H. J. Formamidinium lead trihalide: a broadly tunable perovskite for efficient planar heterojunction solar cells. *Energy Environ. Sci.* **7**, 982 (2014).
48. Lee, J.-W., Seol, D.-J., Cho, A.-N. & Park, N.-G. High-Efficiency Perovskite Solar Cells Based on the Black Polymorph of $\text{HC}(\text{NH}_2)_2\text{PbI}_3$. *Adv. Mater.* **26**, 4991–4998 (2014).
49. McMeekin, D. P., Sadoughi, G., Rehman, W., Eperon, G. E., Saliba, M., Horantner, M. T., Haghighirad, A., Sakai, N., Korte, L., Rech, B., Johnston, M. B., Herz, L. M. & Snaith, H. J. A mixed-cation lead mixed-halide perovskite absorber for tandem solar cells. *Science* **351**, 151–155 (2016).
50. Stoumpos, C. C., Malliakas, C. D. & Kanatzidis, M. G. Semiconducting Tin and Lead Iodide Perovskites with Organic Cations: Phase Transitions, High Mobilities, and Near-Infrared Photoluminescent Properties. *Inorg. Chem.* **52**, 9019–9038. arXiv: arXiv:1011.1669v3 (2013).
51. Ma, F., Li, J., Li, W., Lin, N., Wang, L. & Qiao, J. Stable α/δ phase junction of formamidinium lead iodide perovskites for enhanced near-infrared emission. *Chem. Sci.* **8**, 800–805 (2017).
52. Juarez-Perez, E., Sanchez, R., Badia, L., Garcia-Belmonte, G., Kang, Y., Mora-Sero, I. & Bisquert, J. Photoinduced giant dielectric constant in lead halide perovskite solar cells. *J. Phys. Chem. Lett.* **5**, 2390–2394. arXiv: arXiv:1011.1669v3 (2014).
53. Pellet, N., Gao, P., Gregori, G., Yang, T.-Y., Nazeeruddin, M. K., Maier, J. & Grätzel, M. Mixed-Organic-Cation Perovskite Photovoltaics for Enhanced Solar-Light Harvesting. *Angew. Chemie Int. Ed.* **53**, 3151–3157 (2014).
54. Binek, A., Hanusch, F. C., Docampo, P. & Bein, T. Stabilization of the Trigonal High-Temperature Phase of Formamidinium Lead Iodide. *J. Phys. Chem. Lett.* **6**, 1249–1253 (2015).
55. Amat, A., Mosconi, E., Ronca, E., Quarti, C., Umari, P., Nazeeruddin, M. K., Grätzel, M. & De Angelis, F. Cation-Induced Band-Gap Tuning in Organohalide Perovskites: Interplay of Spin–Orbit Coupling and Octahedra Tilting. *Nano Lett.* **14**, 3608–3616 (2014).
56. Frost, J. M., Butler, K. T., Brivio, F., Hendon, C. H., van Schilfgaarde, M. & Walsh, A. Atomistic Origins of High-Performance in Hybrid Halide Perovskite Solar Cells. *Nano Lett.* **14**, 2584–2590. arXiv: 1402.4980 (2014).

57. Li, W., Thirumurugan, A., Barton, P. T., Lin, Z., Henke, S., Yeung, H. H., Wharmby, M. T., Bithell, E. G., Howard, C. J. & Cheetham, A. K. Mechanical Tunability via Hydrogen Bonding in Metal–Organic Frameworks with the Perovskite Architecture. *J. Am. Chem. Soc.* **136**, 7801–7804 (2014).
58. Lee, J.-W., Kim, D.-H., Kim, H.-S., Seo, S.-W., Cho, S. M. & Park, N.-G. Formamidinium and Cesium Hybridization for Photo- and Moisture-Stable Perovskite Solar Cell. *Adv. Energy Mater.* **5**, 1501310 (2015).
59. Edri, E., Kirmayer, S., Cahen, D. & Hodes, G. High Open-Circuit Voltage Solar Cells Based on Organic–Inorganic Lead Bromide Perovskite. *J. Phys. Chem. Lett.* **4**, 897–902 (2013).
60. Hoke, E. T., Slotcavage, D. J., Dohner, E. R., Bowring, A. R., Karunadasa, H. I. & McGehee, M. D. Reversible photo-induced trap formation in mixed-halide hybrid perovskites for photovoltaics. *Chem. Sci.* **6**, 613–617 (2015).
61. Tanaka, K. & Kondo, T. Bandgap and exciton binding energies in lead-iodide-based natural quantum-well crystals. *Sci. Technol. Adv. Mater.* **4**, 599–604 (2003).
62. Kunugita, H., Hashimoto, T., Kiyota, Y., Udagawa, Y., Takeoka, Y., Nakamura, Y., Sano, J., Matsushita, T., Kondo, T., Miyasaka, T. & Ema, K. Excitonic Feature in Hybrid Perovskite $\text{CH}_3\text{NH}_3\text{PbBr}_3$ Single Crystals. *Chem. Lett.* **44**, 852–854 (2015).
63. Marco, N. D., Zhou, H., Chen, Q., Sun, P., Liu, Z., Meng, L., Yao, E. P., Liu, Y., Schiffer, A. & Yang, Y. Guanidinium: A Route to Enhanced Carrier Lifetime and Open-Circuit Voltage in Hybrid Perovskite Solar Cells. *Nano Lett.* **16**, 1009–1016 (2016).
64. Pham, N. D., Zhang, C., Tiong, V. T., Zhang, S., Will, G., Bou, A., Bisquert, J., Shaw, P. E., Du, A., Wilson, G. J. & Wang, H. Tailoring Crystal Structure of FA 0.83 Cs 0.17 PbI₃ Perovskite Through Guanidinium Doping for Enhanced Performance and Tunable Hysteresis of Planar Perovskite Solar Cells. *Adv. Funct. Mater.* **29**, 1806479 (2019).
65. Kubicki, D. J., Prochowicz, D., Hofstetter, A., Saski, M., Yadav, P., Bi, D., Pellet, N., Lewiński, J., Zakeeruddin, S. M., Grätzel, M. & Emsley, L. Formation of Stable Mixed Guanidinium–Methylammonium Phases with Exceptionally Long Carrier Lifetimes for High-Efficiency Lead Iodide-Based Perovskite Photovoltaics. *J. Am. Chem. Soc.* **140**, 3345–3351 (2018).

66. Giorgi, G. & Yamashita, K. Zero-dipole molecular organic cations in mixed organic–inorganic halide perovskites: possible chemical solution for the reported anomalous hysteresis in the current–voltage curve measurements. *Nanotechnology* **26**, 442001 (2015).

Chapter 2

Experimental methods

This chapter introduces some basic principles of time resolved spectroscopy as well as a detailed discussion of the transient absorption spectroscopy used in much of the experimental work presented in this thesis. In addition, a short introduction to photoemission spectroscopy and two-photon photoemission is given.

2.1 Introduction to ultrafast spectroscopy

For studying dynamical processes such as charge recombination and transfer or short-lived intermediate states in molecular systems and solids, a time resolved spectroscopy is usually employed. These processes occur in the time scale from fs (10^{-15} s) to ps (10^{-9} s). To achieve this type of temporal resolution, a stroboscopic approach, like the one used in high-speed cameras can be used, where a continuous dynamical image can be represented by a series of instantaneous probes. In time resolved spectroscopy, ultrafast femtosecond laser pulses are used and the duration of the pulse becomes the only limiting factor of the temporal resolution. There are many different ultrafast spectroscopy techniques but most of them are built on the framework of the pump-probe method involving two short laser pulses. The first pulse (also called pump pulse) excites the investigated system, and the second pulse is used to measure some distinct properties of the material in its non-equilibrium state. These two pulses are delayed relative to one another in the time domain in a controlled manner. This allows to map the temporal evolution of the system in the time domain. The underlying principle of a generic pump - probe experiment is depicted in the figure 2.1 . Phenomenologically, the pump-probe signal can be written as $P(\tau) = P_0 + \Delta P(\tau)$, where $P(t)$ is the evolution of the physical property P , P_0 is equilibrium value and ΔP is the change from the equilibrium state measured at a specific delay time τ between pump and probe. By varying the time delay between pump probe and measuring P at every delay time τ a full mapping of the $P(\tau)$ in the time domain can be done. There are many variations of this technique such as: transient absorption, reflectivity, dichroism, time resolved photoemission, etc.

2.1.1 Transient absorption

In our study, most of experiments were performed using the so-called transient absorption technique: a pump-probe method to measure the change of the absorption coefficient as a function of delay between pump and probe pulses. The absorption coefficient of the investigated sample can be written as $\alpha(t) = \alpha_0 + \Delta\alpha(\tau)$, where τ denotes the delay between pump and probe pulses. The change of the absorption coefficient can be expressed as the convolution between optical intensity $I(t)$ at the pump pulse and a causal impulse response function $h^{(\alpha)}(t)$:

$$\Delta\alpha(t) = - \int dt' I(t') h^{(\alpha)}(t - t') \quad (2.1)$$

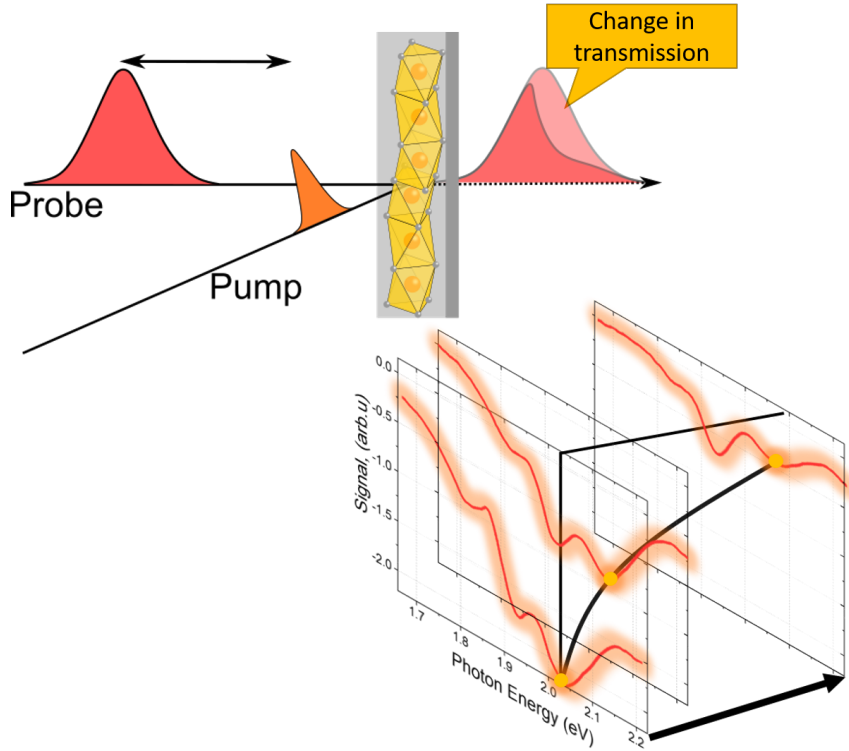


Figure 2.1: a) A typical layout of a pump-probe approach to measure time dependent change in transmission in the photoexcited medium. In this approach a delay between two pulses is introduced and the change of transmission signal as a function of a delay is measured. The detectable change in transmission can be plotted as a function of a delay. b) Using the supercontinuum as a probe pulse, photon energy dependency of the transmission change can be mapped.

The minus sign is added because in the usual experiment, the pump pulse induces a reduction or bleaching of the absorption strength. Field of the probe pulse after the transmission can be expressed as:

$$E_{out} = E_{in}e^{-\alpha L/2} \approx E_{in}[1 - (\alpha_0 + \Delta\alpha)L/2] \quad (2.2)$$

where L is the thickness of the sample. This formalism only works if some assumptions are made. 1. Pump intensity is small enough, so that the induced absorption signal is linear with the intensity. 2. Dispersion effects are small so that the pulse shapes are unchanged going through the sample. We also assume having a slow detector, which will measure only the average power of the transmitted probe beam. In a typical pump probe experiment, the pump induced intensity change is measured. The change is normalized to the intensity of the probe beam and expressed as $\Delta I_{pr}/I_{pr}$. The change in intensity can be expressed as a change in absorption coefficient α .

$$\alpha(\omega) = \sigma_{ij}(N_j - N_i) \quad (2.3)$$

here σ_{ij} is a cross section for a transition from initial (i) to final (j) state, N_i and N_j are populations at the initial and final state. The excitation or pump pulse changes the equilibrium population by ΔN . As a consequence this decreases the population at the ground state creating a ground state bleach effect. The pump induced intensity change as measured by the probe can be expressed as:

$$\frac{\Delta I_{pr}}{I_{pr}} = -\alpha(\omega)\Delta Nd \quad (2.4)$$

it is derived from beer Lambert law, here d is the sample thickness. Depending on the probe frequency (energy), different effects on the transmitted pulse are possible. A ground state depletion when the transmitted pulse intensity is higher or excited state absorption effect - when the transmission intensity is lower.

2.1.2 Supercontinuum generation

Another way to perform the pump-probe experiment is by implementing a white light continuum spectrum as a probe beam. When high intensity laser pulses travel through a transparent medium, a strong spectral broadening is usually observed. This effect sometimes is referred to as a white light generation or supercontinuum generation [1]. This effect can be observed in different materials and in different phases such as in gases, liquids or solids. The continuum spectra is usually used in time resolved pump-probe spectroscopy but also could be used in other fields, such as a tunable seed pulse for optical parametric amplification. The main mechanism for the supercontinuum generation involved three main steps: self-focusing, self-phase modulation and multiphoton ionization.

First, self-focusing process of the pulse in the medium takes place. Very tight focusing of the laser pulse at the peak intensity leads to a self-phase modulation and eventual spectral broadening effect. Spectrally broadened pulses disperse in time due to the group velocity mismatch. Another effect which is involved in the continuum generation process is the multiphoton ionization process at the spatial position of the self-focused laser pulse, which can reduce the self-focusing effect due to free electron generation causing a negative contribution to the refractive index [2].

2.1.3 Transient absorption method

The before mentioned pump-probe technique with a supercontinuum can be used to probe the absorption spectrum of a material of a very broad spectral range spanning from ultraviolet up to infrared. The main object of this type of spectroscopy is to track the optical density of the material as a function of a delay. This kind of experiment allows to obtain information on various dynamical processes in the material, both spectrally and temporally [3]. These processes include charge carrier and exciton relaxation/transfer and hot charge carrier effects [3]. In a typical transient absorption experiment a very weak white light probe pulse is sent through the sample at certain delay time after the excitation pulse. The spectral information of the probe is analyzed by the spectrometer. From the Beer-Lambert law, change in the optical density is given by:

$$\Delta OD(\lambda) = OD_{ex}(\lambda) - OD_{unex}(\lambda) = \log_{10} \left[\frac{I_{unex}(\lambda)}{I_{ex}(\lambda)} \right] \quad (2.5)$$

In some cases the ΔOD is also written as ΔA or being converted to a $\Delta T/T$ using

$$\Delta T/T \approx 1 - (1 - 2.3\Delta OD)$$

Here OD_{ex} and OD_{unex} are optical densities measured in excited and unexcited state the studied material. In the actual transient absorption measurement the intensity of the transmitted probe pulse is measured by the spectrometer. The intensity of the transmitted beam is measured at each delay time, giving a time resolution to the optical density, so that $\Delta OD(\lambda, \tau)$ can be viewed as a 2D matrix as depicted in the figure 2.2. Here depicted is an example of a photoexcited behavior of a perovskite MAPbI_3 . Top panel shows the transient at 1.7eV energy, right panel is the transient spectrum at 70ps, and middle panel is the 2D plot the total transient spectrum. The negative part of the spectrum is called the spectral bleach and the positive is commonly called the photoinduced absorption signal. Details of different types of transient signals will be discussed later in the section "transient spectral fingerprints".

Another difficulty with measuring a spectrally resolved data at high frequency is the speed of the photo detection. In a typical spectrometer, detection is performed using either a photodiode and a rotating grating or a photodiode array. In the former case, the detection speed doesn't exceed 2 kHz, because the readout from each diode linearly creates a certain delay. So, for high repetition rate systems, when the laser repetition rate exceeds spectrometer read out speed, an averaged value of I_{ex} and I_{unex} over multiple laser pulses is used. The averaging is usually

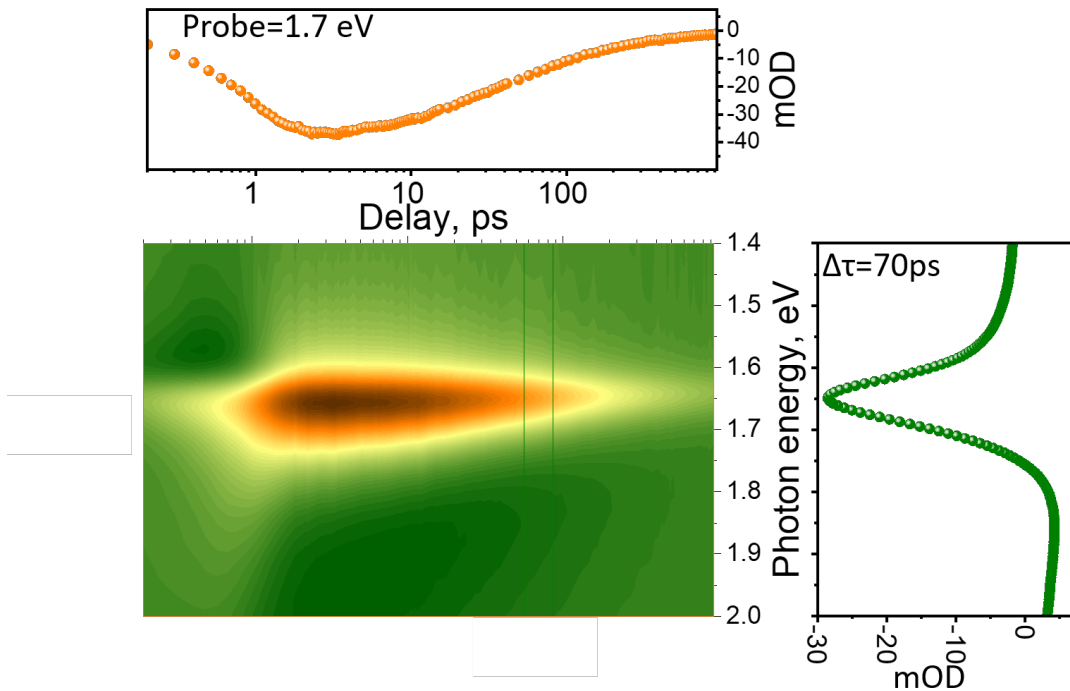


Figure 2.2: Typical transient absorption fingerprint of a photoexcited $MAPbI_3$ using 3 eV as the excitation and supercontinuum as a probe in a transmission geometry. The temporal cut at 1.6 eV probe energy (top) as well as the energy cut at 30 ps delay time (right) are shown. The signal is represented in optical density units (mOD). The negative component at 1.7 eV represent the state filling effect.

performed electronically over certain amount of laser pulses and the differentiation between excited and unexcited spectra is done using a slowly rotating mechanical chopper.

2.1.4 Experimental layout

One of the crucial components for performing time resolved spectroscopy is a laser system. To perform time resolved spectroscopy studies on various materials we have used a Pharos (Light Conversion) laser-based system to generate ultrashort laser pulses. This is a Yb:KGW based regenerative amplifier system, generating 1030 nm pulses with 290 fs temporal width and 0.1 mJ pulse energy. It also has an integrated Pockels cell based pulse picker, allowing to continuously vary laser repetition rate up to 250 kHz. It is combined with a non-collinear optical parametric amplifier (NOPA), which not only compresses pulses for up to 40 fs but also allows to use the signal and idler outputs of 800 nm and 1400 nm, corresponding to photon energies of 1.5 eV and 0.88 eV.

In our study we were focused on transient dynamics in a broad range of photon

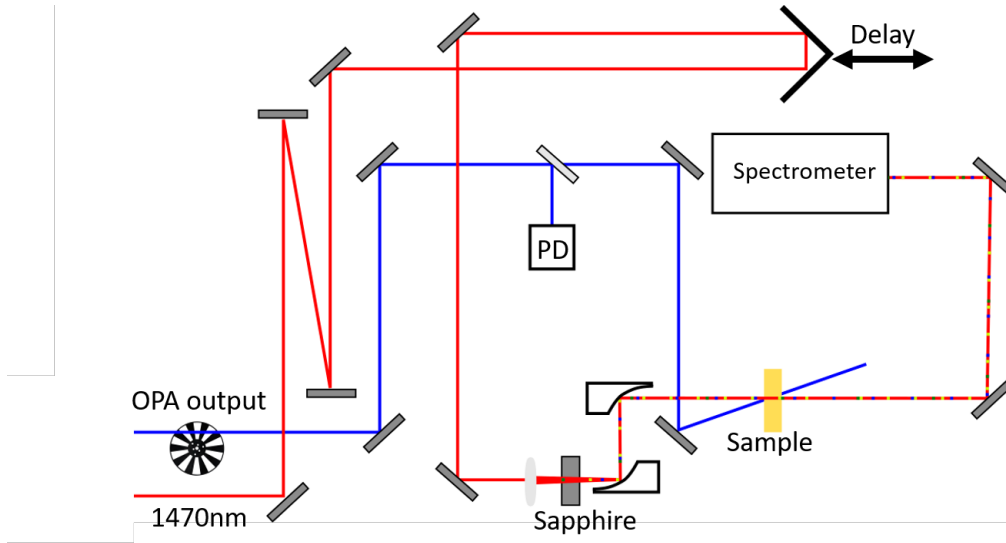


Figure 2.3: The actual layout of a transient absorption setup used in this work. Pump beam (blue), probe beam (red line), PD - a photo-diode.

energies. For this reason, a time resolved broadband pump probe experimental setup was needed, so a commercially available transient absorption spectrometer HARPIA (Light Conversion Ltd.) was used and the layout of it is displayed in the figure 2.3. For white light generation the infrared (0.88 eV) laser output pulse is used and focused on a 4 nm thick sapphire crystal. The generated continuum extends from 2.63 eV (470 nm) to around 0.68 eV (1800 nm). Such spectrally broad pulses cannot efficiently be focused using glass optics without causing large dispersion effects, therefore metallic parabolic focusing mirrors are used. For detecting the probe spectrum in the visible range, Silicon based diode array was used and for near infrared - InGaAs based detector. Our detection scheme involves a separation of measured spectrum to excited and non-excited ones. This was done using a mechanical chopper and additional photo diode, which can detect the chopper blade ON and blade OFF situations. Probe spectra, measured at chopper blade ON are later assigned to the I_{ex} and other ones to I_{unex} .

2.1.5 Types of transient spectral fingerprints

In time resolved spectra both spectral and temporal dynamics can be studied. By probing the spectral degree of freedom, one can say more about the underlying mechanism behind the dynamic phenomena. Depending on the sign and a shape of a spectral component multiple physical phenomena can be deduced. Few examples of spectral shifts and how they can be observed in the transient ΔOD spectra is shown in the figure 2.4. This process leads to a first derivative-like shape of the

ΔOD spectrum.

Spectral shift After the initial excitation pulse, photo excited carriers can cause a change in the material properties and introduce a shift in the optical transition energy. One example of such a process is a band gap renormalization effect caused by photodoping [4]. In molecular systems such a shift can be observed in various different ways, for example a shift in the photoinduced peak due to an ultrafast carrier thermalization or a slow shift in the absorption peak due to thermal or reorientation effects [5].

Spectral bleach In some cases the photoexcitation could lead to a so called bleach effect. In this case carriers fill the bottom of the conduction band and the transition strength of edge states is reduced by the Pauli blocking. In molecular systems, this effect is originating from actual depletion of available electrons in the ground state because usually in molecules, the amount of available state is lower [6]. The bleaching effect causes a reduction in the absorption strength so in the ΔOD spectrum, a negative component is observed.

Photoinduced state The photoexcitation of carriers can introduce an additional optical transition which is not observable in the equilibrium state. This could include a transition from the conduction band bottom to higher states or a new intermediate state. In molecular systems excitation can also create photoproducts which can be optically active, for example a photoisomerization process [6].

Broadening effects The spectral shape of the transition also could be altered by the photoexcitation. For example, the full width at half maximum (FWHM) of the optical transition can be increased by broadening effects. These could arise due to simple temperature effects. The shape of the transient spectrum is shaped like the second derivative of the broadened signal. (figure 2.4 d).

Another important aspect in the time resolved absorption spectroscopy is the process of stimulated emission. This is one of the contributions for a negative spectral component in the ΔOD spectra together with a ground state bleach. In a two level system the Einstein coefficient from the ground to the excited state (A_{12}) which corresponds to the absorption, is same as the transition from excited to the ground state (A_{21}) - stimulated emission. In the transient absorption a stimulated emission (SE) occurs when the probe pulse passes the sample in the excited state. This type of transition overlaps with the fluorescence region because it comes from the same emitting states. The SE signal amplitude is negative in the transient spectrum because of the way the measurement is performed. When the number of photons which reach the detector at certain energy increase, giving same signal as the decrease in the absorption [7].

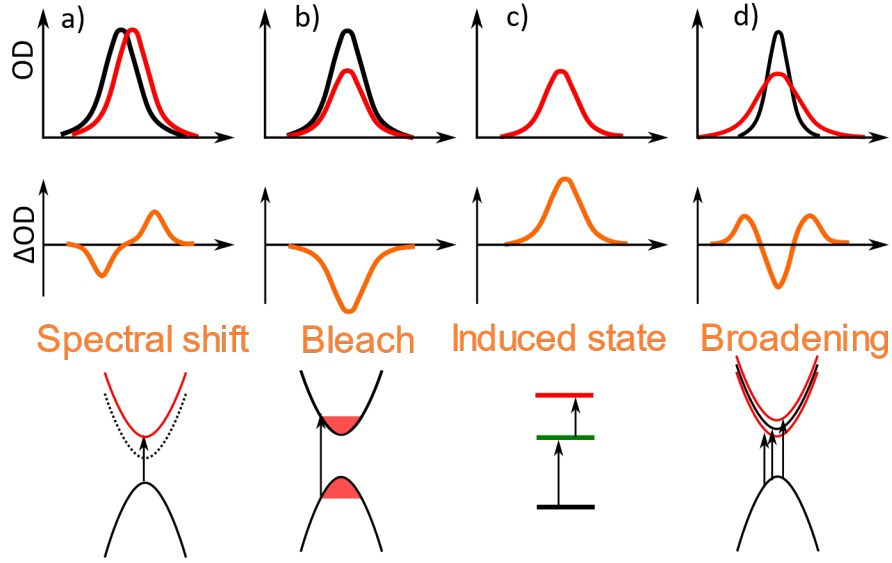


Figure 2.4: Spectral fingerprints of transient absorption spectra, caused by different photophysical processes in a materials: a) The energetical shift of the optical transition b) population of the conduction or valence band caused the edge transitions to be bleached c) new photoinduced transition causes a peak in the time resolved spectrum b) broadening of the optical transition causing reduction of the transition and increase in the absorption near transition edges.

Band gap renormalization and Burstein-Moss effects

Heavy doping of a semiconductor with impurities is known to reduce the bang gap of the energy gap of the materials, and this process is called band-gap renormalization (BGR), due to self-energy effects and screening which are causing the conduction band edge to go down in energy and the valence band energy to go up [8, 9].

The BGR effect (figure

$$\Delta E_{ee} = -\frac{e^2 k_f}{2\pi^2 \epsilon_0 \epsilon_S} - \frac{e^2 k_{TF}}{8\pi \epsilon_0 \epsilon_S} \left[1 - \frac{4}{\pi} \arctan \left(\frac{k_F}{k_{TF}} \right) \right] \quad (2.6)$$

and electron-ion interaction can be approximated with:

$$\Delta E_{ei} = -\frac{e^2 n}{\epsilon_0 \epsilon_S a_{B-}^* k_{TF}^3} \quad (2.7)$$

here the k_F denotes the Fermi vector $k_F = (3\pi^2 n)^{1/3}$ and $k_{TF} = 2\sqrt{k_f / (\pi a_{B-}^*)}$ is the inverse Thomas-Fermi screening length, a_{B-}^* is the screened Bohr radius, also known as the effective Bohr radius, ϵ_S is the static dielectric function of the material. After the photoexcitation the number of carriers in the excited state of the studied material change, and this alter the Fermi vector k_F and the Thomas-Fermi screening length k_{TF} , because they have the electron density term n [4]. This effect can be

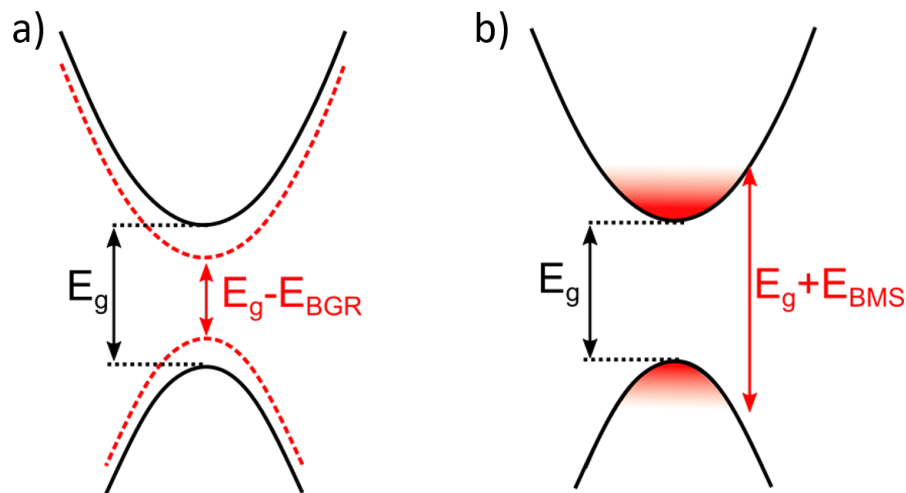


Figure 2.5: a) The band gap renormalization (BGR) process, causing the band gap E_g to shrink due to screening effects; b) Burstein-Moss state filling effect, causing the optical band gap to increase and is caused by Pauli blocking of edge states.

understood in terms of changing of Coulomb screening between particles.

In addition to the band gap shrinkage, electrons, filling the conduction band minimum can increase the band gap energy.

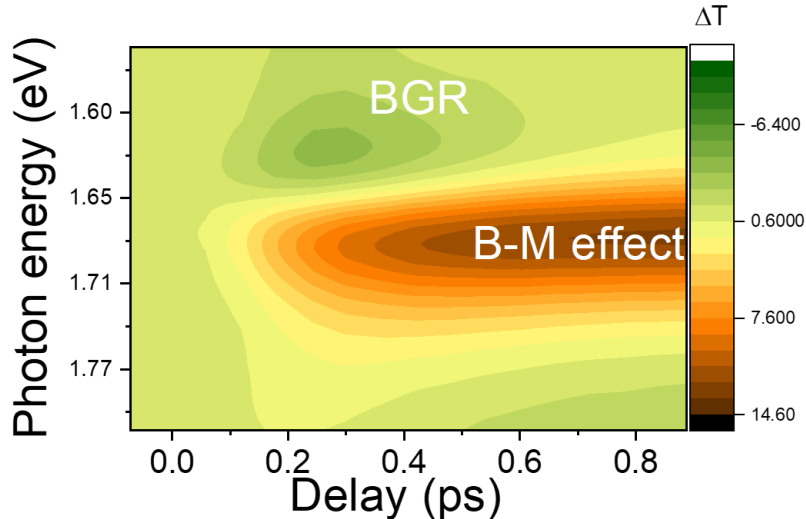


Figure 2.6: Differential absorption spectra of the photo excited $\text{GA}_{0.014}\text{Cs}_{0.043}\text{MA}_{0.13}\text{FA}_{0.73}\text{Pb}(\text{I}_{0.815}\text{Br}_{0.185})_3$ film using 2.5 eV excitation pulse and white light continuum as a probe. In early delay time a band gap renormalization (BGR) spectral feature is highlighted, giving a negative component due to the shrinking of the band gap caused by many body effects. At later delay times Burstein Moss effect becomes dominant and giving rise to the positive spectral component (due to spectral hole burning in the band gap area).

The essence of this is the existence of the Pauli blocking for incoming electrons,

when the bottom of the conduction band is already filled. This effect is known as a Burstein-Moss effect (also known as state filling). The Burstein-Moss shift can analytically be described as:

$$\Delta E_{BMS} = \frac{\hbar^2}{2m_{eh}^*} (3\pi^2 n)^{(2/3)} \quad (2.8)$$

here m_{eh}^* is the reduced effective electron mass. It has the electron density dependent term n . After the photoexcitation electrons and holes acquire a quasi-stable Fermi-Dirac distribution on parabolic bands near band edges. The spectral response of a such a system with a new quasi-Fermi level for electrons of holes can be modeled by removing "filled" states from the overall density of states and would give a Gaussian like response near the band edge. This kind of response is typically what is observed in a differential spectra of hybrid perovskites and was also experimentally confirmed in our study (figure 2.6)

In the transient absorption experiment both BGR and Burstein-Moss effects can be seen as strong spectral features in the band gap region of the material. A typical transient response of the photo-excited quadruple perovskite film is shown in the figure 2.6.

2.2 Photoemission spectroscopy

The underlying phenomena of electron photoemission is based on the so called photoelectric effect, which was discovered by Hertz [10] in 1887 and further explained by Einstein [11] in 1905. This effect occurs when electrons are emitted from the surface when the electromagnetic radiation hits the surface of a material. These emitted electrons are called photoelectron and are being excited by the incoming photon with the energy of $h\nu$. According to classical electromagnetism theory, the photoelectron effect is the transfer of energy from incoming photons to the electrons. Photoelectrons can leave the surface of the material only if the energy of incoming photon $h\nu$ is greater than the work function of the surface ϕ .

The phenomena of photoemission can be used for determining the electronic structure of materials. Depending of the energy of the incoming photons different experimental approaches can be applied. For example the ultraviolet photoelectron spectroscopy (UPS) can be used to investigate valence electrons of the material and X-ray photoelectron spectroscopy (XPS) can be used to investigate core level electrons in the material [12, 13]. One of the most important aspects of this type of spectroscopy is that each photoelectron carries the fundamental information of the

solid by means of the energy and angle of the photoemission. Each electronic state with the binding energy E_B in the photoelectron spectrum would occur at the energy E_{kin} . By applying the energy and momentum conservation law for photoemission [14]:

$$E_{kin} = h\nu - \phi - |E_B| \quad (2.9)$$

$$\mathbf{P}_{||} = \hbar\mathbf{k}_{||} \quad (2.10)$$

Here E_{kin} and $P_{||}$ are measured energy and momentum of the photoelectron and E_B , $k_{||}$ can be used to describe the total band structure of the solid. By knowing the photon energy $h\nu$ and the work function of the material ϕ , material relevant properties can be extracted. In these equations the photon momentum $\hbar k_{h\nu}$ is neglected when photon energy is much smaller than electron momentum. It is also worth noting that in equation 2.10 only the parallel to the sample surface component is conserved. The perpendicular momentum component k_{\perp} of the the electron is conserved in the bulk of the material and the conservation is lost when electron travel through the interface between sample and air and is due to the lack of translational symmetry along the normal direction toward the surface. Experimentally it is also important to use a monochromatic light as the light source to get the precise electronic structure of the material, because the spectral width of incident photons is the limiting factor for the spectral resolution, considering high resolution detectors (100 meV and less). For this reason, lamp, laser or synchrotron light sources are primarily being used for photoemission experiments. The example of the photoemission spectrum of a metal is shown in the figure 2.7. The intensity of the measured spectrum is directly proportional to the density of States (DOS) in the solid. After the photon absorption, the electron is being emitted and correspond to the peak in the photoemission spectrum. As it is seen from the figure 2.7 there is a strong background in the spectrum which is highest at the "secondary electrons". Most of the background and the "secondary electrons" are coming from inelastic scattering which come from the collisions with lattice and other electrons [14]. Electrons participating in the secondary scattering process are electrons with the lowest energy after the ejection from the surface. The Fermi edge which is shown in the figure 2.7 is the Fermi level of the solid and represents the maximum kinetic energy which electrons in the Fermi sea can obtain at 0 K. From the sketch of the photoemission one also can see that the energy of the incoming photon $h\nu$ is equal to the sum of work function Φ and the width of the spectrum, so therefore the work function can be easily deduced from the spectrum: $\Phi = h\nu - (E_{fe} - E_{se})$, where E_{fe} and E_{se} are Fermi edge and

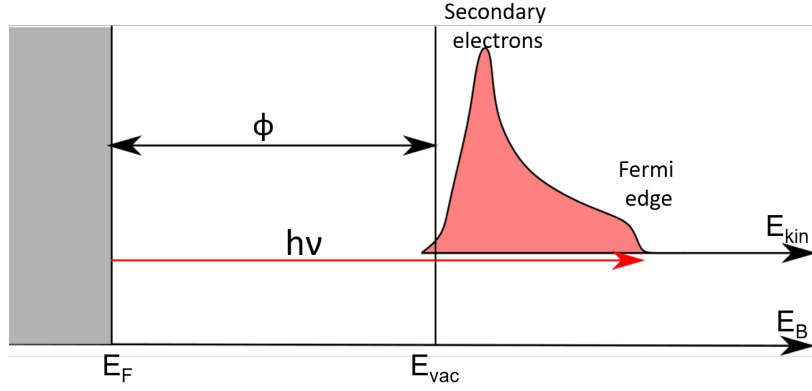


Figure 2.7: Sketch of a typical photoelectron spectrum of a metal. The red arrow indicates the photon energy of photoemission. In the spectrum the edge at higher energy correspond to the fermi level of the material: the highest kinetic energy achievable by electrons. A peak in the lower end of the spectrum correspond to secondary electrons - electrons which lose some energy because of inelastic scattering events. The work function of the material can be obtained by subtracting the width of the spectrum from the energy of the incoming photons.

secondary edge energies respectively.

To gain more insight to the details of the photoemission process in solids, a three-step model is widely being used: i) electron is being excited from the ground to the excited state ii) electron traveling from the bulk to the surface of the sample iii) electron escapes the sample surface and is detected by the electron analyzer. During the first step, electron carries the most information about the solid. During the second step electron is scattered elastically and inelastically within the solid. In the third step electrons overcome the work function of the solid and change the k_{\perp} . Mathematically the photoemission spectrum can be described by the spectral function of removing one electron from the system times cross product of the photon-electron interaction and cut-off by the Fermi distribution function. The spectral function of removing or adding one electron to the system can be written as:[12]

$$A^{\pm}(\mathbf{k}, \omega) = \sum_m |\langle \Psi_m^{N\pm 1} | \Psi_i^{N-1} \rangle|^2 \delta(\omega - E_m^{N\pm 1} + E_i^N) \quad (2.11)$$

here $A(\mathbf{k}, \omega)$ denotes a one particle spectral function, $\Psi_i^{N-1} = c_{\mathbf{k}} \Psi_i^N$, where $c_{\mathbf{k}}$ is the annihilation operator. The energy terms correspond to: $E_m^{N-1} = E_f^N - E_{kin}$ and $E_i^N = E_i^{N-1} - E_B^{no}$, where f and i denote the final and initial states.

The Intensity of the photoemission spectrum in the full form can be written as:

$$I(k, \omega) \propto \sum_{f,i} |M_{f,i}^k|^2 f(\omega) A^-(\mathbf{k}, \omega) \quad (2.12)$$

here the $M_{f,i}^{\mathbf{k}} \propto \langle \phi_f^{\mathbf{k}} | \mathbf{A} \cdot \mathbf{p} | \phi_i^{\mathbf{k}} \rangle$ is the dipole matrix element of the photon-electron interaction. This shows that intensity of the photoemission spectrum also strongly depends on the energy and polarization of the incoming photon through the photon-electron matrix element. At different photon energies the cross section of certain electronic transition can drop, so a tunable source for the photoemission experiment is preferred.

2.2.1 Two photon photoemission (2PPE)

Previously discussed photoemission experiment involve only a one photon process, where a single photon is used to eject electrons from the sample to the detector. However, employing two photons for the photoemission experiment and using a pump-probe type of layout of two photons, a temporal information of electronic properties can be gathered. Since the delay between two pulses can be precisely controlled, a temporal evolution can be mapped [15].

In the two-photon photoemission (2PPE) experiment the first pulse is promoting electron to the excited state and the secondary pulse is used to eject electrons from the sample by a photoemission process. Generally, the energy of both pulses is set to be smaller than the work function of the material, to avoid the single photon photoemission by one of the pulses. By changing the temporal delay between two pulses a direct evolution of excited electrons can be measured. In this type of experiment the photon energy term $h\nu$ in Equation 2.9 can be replaced by the sum of photon energy two separate pulses $h\nu = h\nu_1 + h\nu_2$. Unlike in the simple one photon photoemission, in 2PPE the photoemission can arise both from occupied and unoccupied states, whereas in the simple photoemission only occupied states can be monitored. Worth noting is that in 2PPE experiment the intermediate does not have to be a real state, it also could be a virtual state. The virtual intermediate state can be observed when both pump and probe pulses temporally overlap.

A typical spectrum of the 2PPE emission can have spectral components which are not present in the conventional photoemission spectrum. These could come both from the electron population in the initial state or due to the existence of a real intermediate state. Because in the 2PPE experiment an additional dimension of time can be obtained, the distinction between real or virtual intermediate state can be obtained from time dynamics.

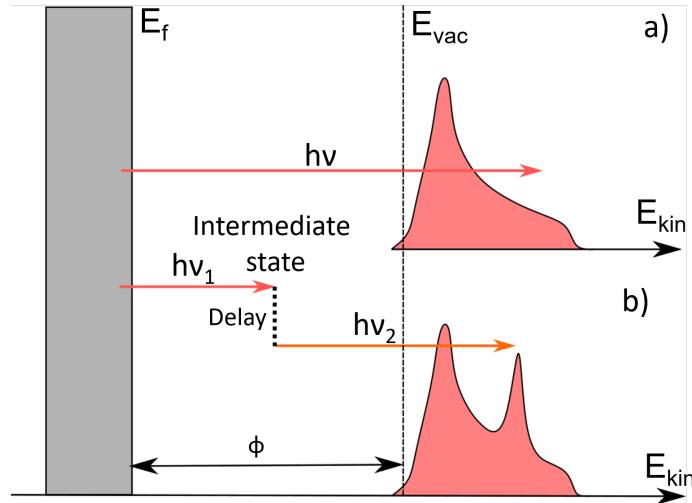


Figure 2.8: Comparison between a conventional single photon photoemission (a) and the two photon photoemission experiment (b); In the 2PPE approach two photons with a possible temporal delay between them are used and additional peak in the photoemission spectrum could be corresponding both to the intermediate and the initial state occupation.

2.2.2 Experimental details of 2PPE spectroscopy

In our study, the two photon photoemission experiments were carried out using a conventional Ti:Sapphire crystal based laser system (RegA by Coherent), having a $6 \mu\text{J}$ energy per pulse and a repetition rate of 250 kHz. A small fraction of the fundamental (1.55 eV) laser output is converted to the second harmonic (3.1 eV) by using the β -BBO non-linear crystal and the rest of the energy is used to generate the third harmonic pulses (4.7 eV in a second BBO crystal). The shortest achievable time resolution of the 2PPE experiment is 50 fs. The 4.7 eV laser pulses are used for the photoelectron generation, while the 3.15 eV pulses were used to promote electron to the higher electronic state. Photoemitted electrons were detected using a hemispherical energy analyzer with $5^\circ \times 1^\circ \text{ deg}^2$ acceptance angle around the normal emission direction. Due to the short pulse duration of laser pulses which are the limiting factor for the achievable resolution, the spectral resolution of the setup was 60 meV.

References

1. Prasankumar, R. P. & Taylor, A. J. *Optical techniques for solid-state materials characterization* 748 (CRC press, 2011).

2. Rothenberg, J. E. Pulse splitting during self-focusing in normally dispersive media. *Opt. Lett.* **17**, 583–585 (1992).
3. Andrew M. Weiner. *Ultrafast optics* (John Wiley & Sons, Ltd, 2008).
4. Feneberg, M., Osterburg, S., Lange, K., Lidig, C., Garke, B., Goldhahn, R., Richter, E., Netzel, C., Neumann, M. D., Esser, N., Fritze, S., Witte, H., Bläsing, J., Dadgar, A. & Krost, A. Band gap renormalization and Burstein-Moss effect in silicon- and germanium-doped wurtzite GaN. *Phys. Rev. B* **90**, 075203 (2014).
5. Vogt, G., Nuernberger, P., Gerber, G., Improtta, R. & Santoro, F. Femtosecond study on the isomerization dynamics of NK88. II. Excited-state dynamics. *J. Chem. Phys.* **125**, 044513 (2006).
6. Materials, M., Copyright, G. L., Gmbh, W.-v. V. & Isbn, W. *Photophysics of Molecular Materials* (ed Lanzani, G.) (Wiley, 2005).
7. Grattan, K. *Charge and Energy Transfer Dynamics in Molecular Systems* **8**, 657 (2003).
8. Mahan, G. D. Energy gap in Si and Ge: Impurity dependence. *J. Appl. Phys.* **51**, 2634 (1980).
9. Berggren, K. F. & Sernelius, B. E. Band-gap narrowing in heavily doped many-valley semiconductors. *Phys. Rev. B* **24**, 1971–1986 (1981).
10. Hertz, H. Ueber einen Einfluss des ultravioletten Lichtes auf die elektrische Entladung. *Ann. der Phys. und Chemie* **267**, 983–1000 (1887).
11. Einstein, A. Über einen die Erzeugung und Verwandlung des Lichtes betreffenden heuristischen Gesichtspunkt. *Ann. Phys.* **322**, 132–148 (1905).
12. Schattke, W. & Van Hove, M. A. *Solid-state photoemission and related methods: Theory and experiment* (John Wiley & Sons, 2008).
13. Reinert, F. & Hüfner, S. Photoemission spectroscopy - From early days to recent applications. *New J. Phys.* **7** (2005).
14. Damascelli, A., Hussain, Z. & Shen, Z. X. Angle-resolved photoemission studies of the cuprate superconductors. *Rev. Mod. Phys.* **75**, 473–541. arXiv: 0208504 (2003).
15. Petek, H. & Ogawa, S. Femtosecond time-resolved two-photon photoemission studies of electron dynamics in metals. *Prog. Surf. Sci.* **56**, 239–310 (1997).

Main goals and achievements

Main goal of this thesis was to investigate charge carrier and exciton dynamics in organic/inorganic materials used for solar cell applications in order to better understand the underlying microscopic mechanisms influencing efficiency of solar cells. Studied solar cell materials ranged from organic, small molecules (merocyanine and PC₆₁BM)) to organic/inorganic hybrid perovskite materials such as MAPbI₃ and more complex perovskites with different organic cations and halides. The wide range of studied materials allowed to have a broader view on charge transfer mechanisms in different compound groups.

Experimentally, dynamics of charge and exciton transfer was studied using different ultrafast spectroscopy techniques such as transient absorption and transient photoemission. Studied materials were also characterized by standard optical techniques such as absorption and photoluminescence. For merocyanine molecules it was found that intermolecular interactions and packing behavior plays a major role in charge transfer exciton formation. The specific orientation at which the merocyanine and PC₆₁BM molecules pack can increase the exciton delocalization.

In MAPbI₃ films the charge (holes) extraction to a PEDOT:PSS layer was investigated using transient absorption spectroscopy. By simulating the hole diffusion in MAPbI₃ layer with a conventional 1D diffusion model the hole mobility was extracted.

In quadruple cation mixed halide perovskite (GA_{0.014}CS_{0.043}MA_{0.13}FA_{0.73}Pb(I_{0.815}Br_{0.185})₃) charge dynamics from femtosecond to microsecond was studied using time resolved spectroscopy techniques. In time resolved photoemission and transient absorption experiments, a 0.5 ps excitation decay component, representing the band gap renormalization was observed. A fluence dependent study allowed to extract the effective mass of electrons and holes. In this study the new quadruple cation mixed halide perovskite was characterized both chemically (NMR) and structurally (XRD).

Chapter 3

Hole diffusion in MAPbI₃ films

Carrier diffusion processes in hybrid perovskite materials play a crucial part in understanding fundamental properties of perovskite based devices. This chapter present a study of intrinsic carrier transport properties and excited carrier dynamics of the MAPbI₃ / PEDOT:PSS / ITO multilayer structure using time resolved absorption spectroscopy.

Parts of this chapter was published in: Budzinauskas, K., Ewertowski, S., Olthof, S., Budzinauskas, K., Ewertowski, S., Olthof, S., Meerholz, K., Van Loosdrecht, P. H. Charge carrier migration and hole extraction from MAPbI₃. J. Phys. Conf. Ser. **1220** (2019)

3.1 Introduction

Despite the rapid increase in efficiency, the exact origin for the extraordinary photovoltaic properties of hybrid perovskites are still under debate. It is postulated that these are strongly correlated with anomalous MAPbI₃ carrier transport properties. Diffusion lengths in disordered MAPbI₃ films exceed 1 micrometer but mobilities are very modest, giving bimolecular recombination rates as small as in well studied single-crystalline inorganic semiconductors such as GaAs or Si:H and 5 orders lower than the mobility limited Langevin recombination model[1]. Some authors claim, that charge carriers in MAPbI₃ are screened by large polarons which prohibit carrier recombination and are the reason for the long carrier lifetimes observed in MAPbI₃[2]. Other arguments for the lifetime are based on the extraordinary defect tolerance due to the unique band structure of this material; both the conduction band and the valence band are formed from antibonding mixed Pb-I orbitals with strong ionic character, and within the band gap only shallow (benign) defects can be formed[3]. Up to now, there are widespread inconsistencies in the estimation of transport properties such as carrier mobility and diffusion constants in hybrid perovskites. mobility values in MAPbI₃ films vary from 0.6 cm²(Vs)⁻¹ to 80 cm²(Vs)⁻¹ depending on the both sample preparation method and the measurement technique[4, 5]. Such a wide range of measured mobilities shows how strongly the sample morphology and implemented measurement technique can influence the outcome of the mobility measurement. A good way to overcome this is to apply contactless, optical techniques to measure carrier transport properties in state-of-the-art perovskite materials in a pre - device structure. In this study, we employ optical spectroscopy to measure carrier transport in MAPbI₃ films, using a transient absorption method; this allows us to estimate intrinsic carrier diffusion constants by using a selective charge extraction layer of PEDOT:PSS which enables the efficient hole extraction.

3.1.1 Experimental setup

For a successful charge extraction experiment, an effective charge extraction layer is needed. The sample structure is shown in the figure 3.1a. First, PEDOT:PSS (Clevis 4083, Heraeus) was spin coated onto an ITO (indium tin oxide) covered quartz glass slide. Next, a solution containing PbI₂ (Sigma-Aldrich) and MAI (prepared according to literature)[6] in a molar ratio of 1:1 was prepared and 18 mg/ml of the additive NH₄Cl were added[7]. Studied materials were grown by our collaborator Dr. Selina Olthof (Department of chemistry, University of Cologne). For the 170 nm

sample, a concentration of 310 mg/ml in DMF was used, while for the thinner one it was reduced to 80 mg/ml. All films were spin coated inside a nitrogen filled glovebox at 6000 rpm for 50 s and then heated at 110 °C for 30 s. Small amounts of toluene were dropped around the spin-coater to create a solvent atmosphere. Tin oxide covered glass was used in order to reproduce the perovskite growing condition close to the device level, because it serves as a transparent conductor layer in a functioning device.

Time resolved absorption as well as static absorption experiments were performed under ambient pressure at room temperature. Transient spectrometer was used as described in the introduction section. Photoexcitation with the energy of 1.77 eV was used in order to create photo carriers above the band gap. A typical optical band gap value of the MAPbI₃ is around 1.58-1.6 eV. For carrier density calculations, the initial excitation density and the excitation profile throughout the sample was calculated using a conventional Beer-Lamberts law. The total carrier population was calculated by integrating.

3.2 Experimental results and discussion

Linear and transient absorption plots of both samples are shown in the figure 3.1. From tauc type plots, the extrapolation of the transition edge yields an optical band gap of 1.6 eV and 1.62 eV for the thicker and thinner MAPbI₃ film, respectively; the extracted absorption coefficient of both MAPbI₃ layers at the 1.75 eV is $2.5 \cdot 10^4 \text{ cm}^{-1}$, which is in good agreement with literature values for spin coated MAPbI₃. [8] Absorption spectra near the band gap of both 40 nm and 170 nm samples showed a typical excitonic offset in the band gap region.

To determine the excitonic transition contribution, the absorption spectra were modeled using a simplified Elliot formula [10], which can be used to model the absorption spectrum of MAPbI₃ [11]. The absorption coefficient in a band to band transition when the Coulomb interaction between electron and hole is neglected is proportional to $(\alpha_{free} = \hbar\omega - E_g)^{1/2}$. When excitonic effects are present, the Coulomb interaction between electron and hole must be taken into consideration. To derive a proper absorption coefficient taking Coulomb interactions into account, the exciton can be treated as a two-particle system (hole and electron) moving with a center of mass (CM). The motion of the CM can be described as a free particle with no Coulomb interaction. The relative motion inside this particle is like a hydrogen atom where electron moves around a positively charged nucleus. The solution of this type of motion yields discrete states, with quantum number of $n = 1, 2, \dots$ and

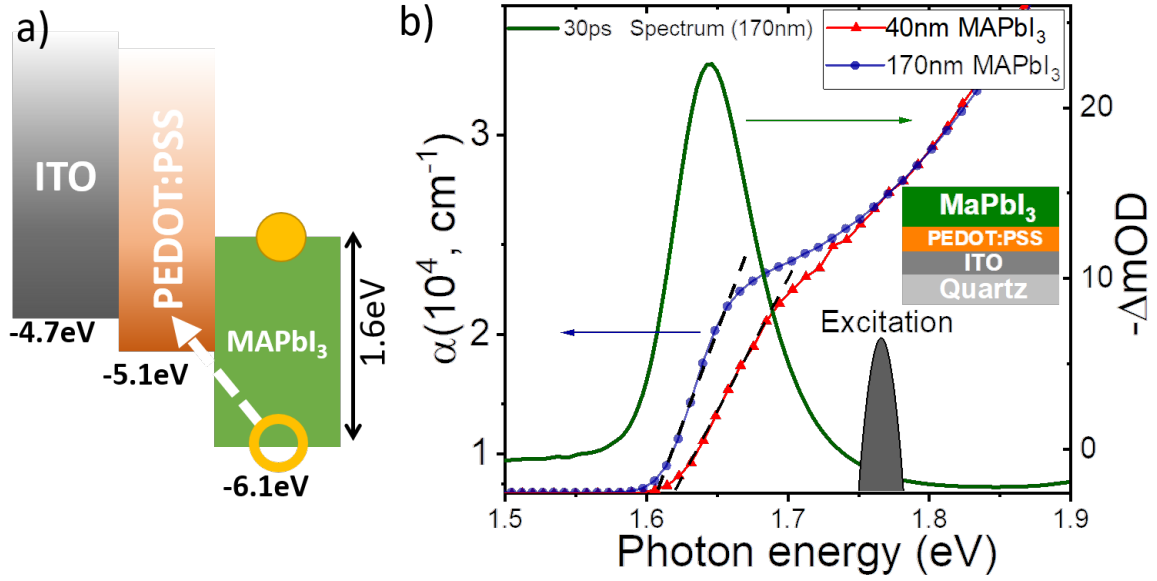


Figure 3.1: a) Energy level diagram of the studied perovskite structure; b) Tauc plots of linear absorption for perovskite films with different thickness. Extrapolated lines indicate optical gap of investigate perovskite films transient absorption spectra (green) at 30 ps after optical excitation with 1.77 eV pulse with a bleach signal at 1.65 eV of 170 nm thick film.

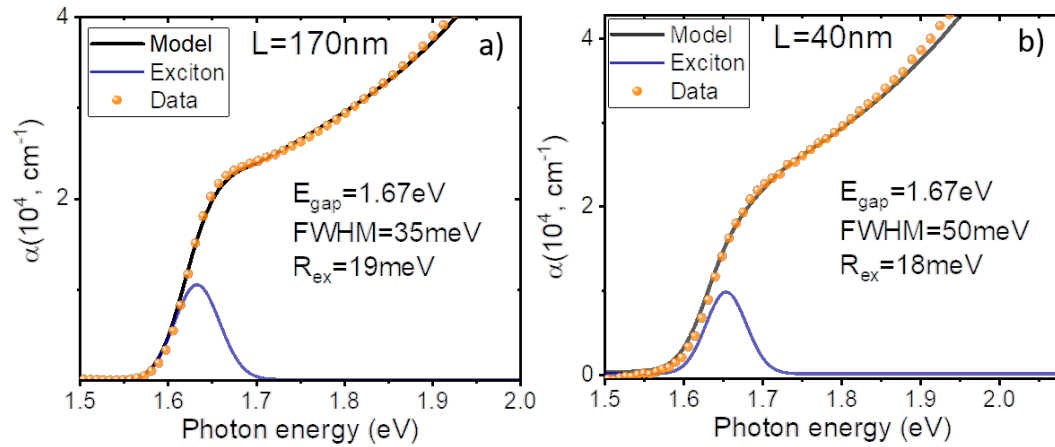


Figure 3.2: Optical absorption spectra of perovskite films with different thickness and modeled absorption spectrum of each sample. Blue lines represent the excitonic transition, computed using the second term of the Elliot formula (equation 3.4), black represent the full modeled absorption spectrum using Elliot formalism (excitonic + continuum of states terms in the equation 3.4), dots represent the actual measured absorption data. Model parameters are shown in the inset of each graph. Reproduced from [9].

continuum of states when $n \rightarrow \infty$. According to the Elliot's theory "excitons can be considered to be ionized into free electrons and free holes but their wave functions are still modified by their Coulomb interaction" [12]. The Coulomb interaction on

the continuum of states in the absorption spectrum leads to a so called "Coulomb enhancement" [13]. The absorption of the continuum of states compared to the band to band type of absorption is modified by the so called Sommerfeld-enhancement factor $S(\hbar\omega)$:

$$\alpha_{con} = S(\hbar\omega)\alpha_{free} \quad (3.1)$$

where $S(\hbar\omega)$ is described as

$$S(\hbar\omega) = \frac{\pi x \cdot \exp(\pi x)}{\sinh(\pi x)}. \quad (3.2)$$

In this equation the x term is expressed as

$$x = \sqrt{\frac{E_b}{\hbar\omega - E_g}}, \quad (3.3)$$

where E_b represents the binding energy of the exciton. The full description of the absorption spectrum using Elliot formalism is then given by:

$$\alpha(\hbar\omega) = A \cdot \left([\theta(\hbar\omega - E_g) \cdot D_{cv}(\hbar\omega)] \cdot \left[\frac{\pi x e^{\pi x}}{\sinh(\pi x)} \right] + E_b \sum_{n=1}^{\infty} \frac{4\pi}{n^3} \delta\left(\hbar\omega - E_g + \frac{E_b}{n^2}\right) \right) \quad (3.4)$$

Here E_g represents the band gap of the material, Θ a step function, and D_{cv} the joint density of states of two parabolic bands $(\hbar\omega - E_g)^{1/2}$, δ is the delta function. The left part of the first term is a square root dependency mitigating the joint density of state between two parabolic bands. The right part of this term reflects the influence of the Coulomb interaction that enhances the entire continuum of states especially near the gap. The second term of the Elliot equation describes the excitonic transitions with intensity of each excitonic line n dropping as $1/n^3$ and the energetic distance between different exciton lines n varying as E_b/n^2 .

To describe the spectrum of a real material inhomogeneous increase effects as well as instrumental resolution must be considered. Since in our case the instrumental resolution is better than the inhomogeneous broadening, it can be neglected. Incorporation of broadening effects into the model can be done by convolution with a Gaussian distribution function. Figure 3.2 shows the results of fitting the Elliot model (black lines) to our data (yellow bullets) and the exciton peak (blue lines). The model yield estimates for the exciton binding energy of $E_b = 19 \pm 3$ meV and 18 ± 3 meV for the two films. The observed slight differences in broadening effects

(FWHM of 35 and 50 meV) can be attributed to the different disorder in MAPbI₃ films of different thicknesses.

Transient absorption experiments were carried out using above band gap excitation at 1.77 eV. The fluence dependent measurements have shown a strong fluence dependency of the decay of the transient signal, indicating that carrier-carrier interactions play an important role in the carrier recombination processes. This is demonstrated in the figure 3.3, which shows the transient data of the 170 nm thick sample for three different excitation densities at the probe energy of 1.65 eV. For carrier density calculations a care was taken to have the same induced carrier density in both samples of different thickness. In addition, experiments have been performed at the lowest possible fluence regime ($2 \cdot 10^{15} \text{ cm}^{-3}$) to minimize the influence of bi-particle recombination processes. It is worth noting that lower than $2 \cdot 10^{15} \text{ cm}^{-3}$ carrier densities could not be experimentally measured because it is close to the signal to noise limitation of the transient absorption setup.

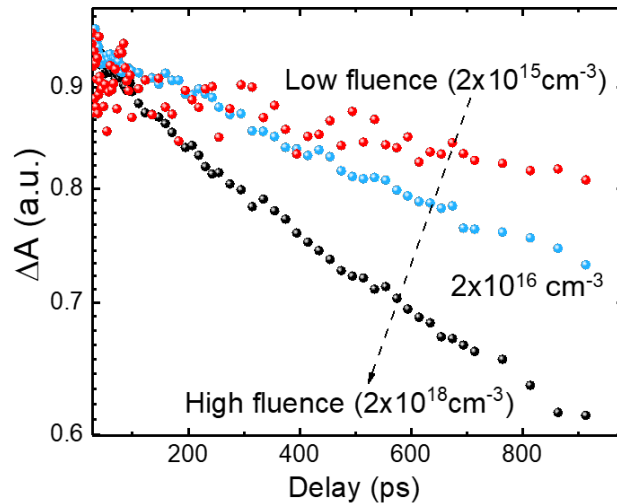


Figure 3.3: Fluence dependent decay dynamics of 170 nm thick *MAPbI*₃ film shown on a semilog scale. For optical excitation 1.77 eV photon energy was used. The decay dynamics shows a strong dependence on the carrier density (varied here between $2 \cdot 10^{15} \text{ cm}^{-3}$ and $2 \cdot 10^{16} \text{ cm}^{-3}$) demonstrating the importance of multiparticle decay processes.

A typical TA spectrum is shown in the figure 3.1b; after the excitation, electrons and holes occupy the bottom of the conduction and top of the valence band, resulting in a transient population with a new quasi Fermi levels. This leads to a diminished number of available states for an optical transition resulting in a strong transient absorption peak in the region close to the band gap edge. The amplitude of the state filling peak, assuming a rigid band picture and Pauli blocking of charges

with equivalent spins, is directly proportional to the number of photo-generated carriers. Quantitatively the state filling (Burstein Moss) shift of the optical gap can be described as: $\Delta E_{BMS} = \frac{\hbar^2}{2m_{eh}^*} (3\pi n)^{(2/3)}$. This picture is valid only at delay times > 5 ps, when most of photo-excited electrons and holes have equilibrated and populate the conduction band minimum and valence band maximum. At earlier times, in the presence of high hot carrier densities, also band-gap renormalization plays a role in the transient response[11]. By monitoring the amplitude of a state filling peak in the transient absorption spectrum one can get insight into the excited carrier dynamics in the material.

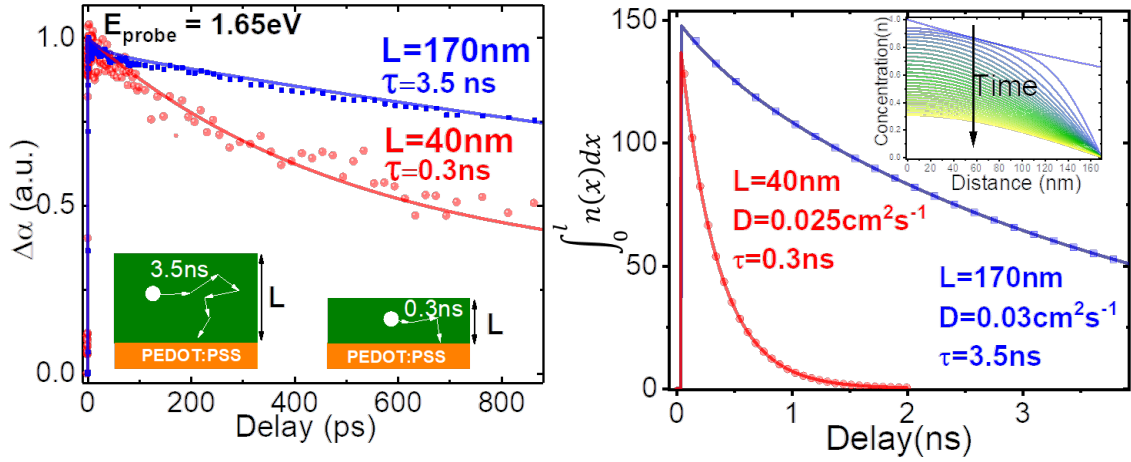


Figure 3.4: a) Excited state dynamics of perovskite films with different thicknesses at a probe photon energy of 1.65 eV; b) model dynamics of the carrier population in the sample volume using a 1D diffusion model (see text) with specific diffusion constants. Simulation with different diffusion constants show a good agreement between experiment theory.

The decay dynamics of both films are shown in the figure 3.4 a. Most notably, the carrier dynamics show a strong MAPbI₃ layer thickness dependency. It was shown in our fluence dependent studies that with a carrier density of $(2 \cdot 10^{15} \text{ cm}^{-3})$ bi-particle recombination processes don not play a major role in the recombination dynamics. Thus we can conclude that carriers decay mainly on the MAPbI₃/PEDOT:PSS interface and the recombination process is diffusion limited. To prove this, a generic 1D diffusion model can be used to recreate the carrier decay dynamics at different thickness MAPbI₃. This model would not only show that carrier decay is diffusion limited but also provide information on intrinsic carrier diffusion and mobility properties.

The carrier decay at different thicknesses was fitted using a single exponential decay model with a non-decaying component C , $A \cdot e^{-\frac{t}{\tau}} + C$, and convolved with a Gaussian instrument response function and a step function:

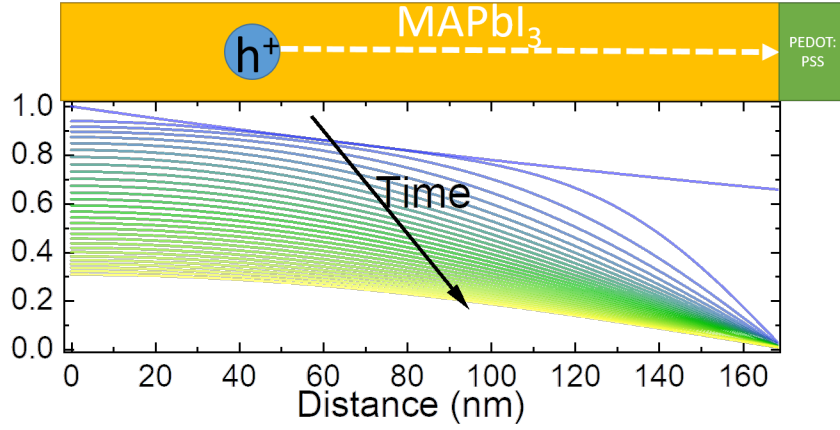


Figure 3.5: Cross section of the numerically simulated carrier distribution in the MAPbI₃ layer. The initial condition was a carrier distribution calculated from the Beer-Lambert law .

$$\frac{A}{2} \left[1 + \operatorname{erf} \left(\frac{t - \frac{g^2}{\tau}}{g\sqrt{2}} \right) \right] \cdot \left[e^{-\frac{t}{\tau}} \cdot e^{\frac{g^2}{2\tau^2}} \right] + \frac{C}{2} \left[1 + \operatorname{erf} \left(\frac{t - \frac{g^2}{\tau}}{g\sqrt{2}} \right) \right] \quad (3.5)$$

In this expression g (80 fs) represents the experimental resolution which is used to fit the initial growing component of the decay signal. For both samples the amplitude of A and C are very similar, which is expected for a hole only diffusion driven process. Here we assume that the carrier decay mechanism is dominated by a hole transfer from a MAPbI₃ layer to the PEDOT:PSS while electrons remain in the MAPbI₃ film and contribute to the non-decaying component C . Interestingly, we find one order of magnitude difference in the carrier lifetimes in two films with different thicknesses, $\tau = 0.30$ ns for 40 nm and $\tau = 3.5$ ns for 170 nm, even though they are prepared from the same material using the same procedure, so the bulk recombination contribution should remain the same. Since the carrier density in both cases was also kept identical, the recombination time differences must originate from differences in carrier diffusion to the interface with PEDOT:PSS. We postulate that this gives a strong dependency to different MAPbI₃ layer thickness: carrier have to travel longer distance from MAPbI₃ to reach the interface between PEDOT:PSS and MAPbI₃, hole transfer could occur. To confirm this theory, a numerical simulation 1D diffusion was used and the diffusion constant D was varied to replicate the carrier recombination dynamics as measured by the transient absorption.

$$\frac{\partial n(x, t)}{\partial t} = D \frac{\partial^2 n(x, t)}{\partial x^2} \quad (3.6)$$

The Beer-Lambert law $e^{-L\alpha}$ carrier distribution was chosen as the initial carrier

distribution condition. The absorption coefficient α was extracted from the linear absorption measurements data and L corresponds to the MAPbI₃ layer thickness. The layer thickness was evaluated experimentally using different spin coating time and measured non-directly using absorption spectra. In the 1D diffusion model, one boundary (the excitation facing surface) is assumed fully reflecting: $\frac{\partial n}{\partial x} = 0$ and the other side of film (covered with PEDOT:PSS) fully absorbing: $n = 0$.

Results of the numerical diffusion simulation for both samples are shown in the figure 3.4b. In the inset of the figure 3.4b, a carrier distribution cross section in the film at each time step is shown. The overall carrier population at each time step was calculated by integrating all carriers in the volume. The extracted time dependent carrier population was then plotted and fitted with a single exponential decay function $e^{-\frac{t}{\tau}}$. The best match with experimental decay values was found using diffusion constants of $0.025 \text{ cm}^2\text{s}^{-1}$ and $0.030 \text{ cm}^2\text{s}^{-1}$ for the 40 nm and 170 nm thick films respectively, with estimated errors of $\pm 0.003 \text{ cm}^2\text{s}^{-1}$. A good agreement between experimental results and diffusion model confirms our theory that at sufficiently low carrier densities the major contribution to carrier dynamics is the recombination at the interface with hole extraction material PEDOT:PSS.

From diffusion modeling results we were able to extract the hole mobility μ through the Einstein relation: $\mu = D \cdot e \cdot k_B \cdot T$, where e is the electron charge $1.6 \cdot 10^{-12} \text{ C}$ and $k_B = 1.3810^{-23} \text{ m}^2\text{kg} \cdot \text{s}^{-2}\text{K}^{-1}$ the Boltzmann constant. Using this equation, a hole mobility of $1 \text{ cm}^2(\text{Vs})^{-1}$ was estimated which again is in good agreement with mobility values, estimated from optical measurements such as photoluminescence decay[14].

3.3 Conclusions

In this study, we have shown a simple way to extract the intrinsic carrier diffusion and carrier mobility parameters using transient absorption experiment, combined with a generic 1D carrier diffusion model. By employing a hole extraction layer of PEDOT:PSS we were able to gain insight into the hole transport through the excited carrier relaxation time. It was found that a difference in MAPbI₃ film thickness does not affect the carrier transport properties significantly, meaning that the film quality remains the same. We estimated the hole diffusion constant of $0.025 \text{ cm}^2\text{s}^{-1}$ for the 40 nm and $0.030 \text{ cm}^2\text{s}^{-1}$ for the 170 nm thick MAPbI₃ film. Using calculated diffusion constant values and the Einstein relation, resulted in an estimation for the hole mobility of $1 \text{ cm}^2(\text{Vs})^{-1}$.

Collaborations

The work presented in this chapter has been performed in a collaboration with Dr. Selina Olthof and Prof. Klaus Meerholz (sample growth and preparation procedures).

References

1. Wehrenfennig, C., Eperon, G. E., Johnston, M. B., Snaith, H. J. & Herz, L. M. High Charge Carrier Mobilities and Lifetimes in Organolead Trihalide Perovskites. *Adv. Mater.* **26**, 1584–1589 (2014).
2. Zhu, X.-Y. & Podzorov, V. Charge Carriers in Hybrid Organic–Inorganic Lead Halide Perovskites Might Be Protected as Large Polarons. *J. Phys. Chem. Lett.* **6**, 4758–4761. arXiv: arXiv:1507.02179v1 (2015).
3. Brandt, R. E., Poindexter, J. R., Gorai, P., Kurchin, R. C., Hoye, R. L., Nienhaus, L., Wilson, M. W., Polizzotti, J. A., Sereika, R., Žaltauskas, R., Lee, L. C., Macmanus-Driscoll, J. L., Bawendi, M., Stevanović, V. & Buonassisi, T. Searching for "defect-Tolerant" Photovoltaic Materials: Combined Theoretical and Experimental Screening. *Chem. Mater.* **29**, 4667–4674 (2017).
4. Stranks, S. D., Eperon, G. E., Grancini, G., Menelaou, C., Alcocer, M. J. P., Leijtens, T., Herz, L. M., Petrozza, A. & Snaith, H. J. Electron-Hole Diffusion Lengths Exceeding 1 Micrometer in an Organometal Trihalide Perovskite Absorber. *Science* **342**, 341–344 (2013).
5. Kim, D. H., Park, J. J. S., Li, Z., Yang, M., Park, J. J. S., Park, I. J., Kim, J. Y., Berry, J. J., Rumbles, G. & Zhu, K. 300% Enhancement of Carrier Mobility in Uniaxial-Oriented Perovskite Films Formed by Topotactic-Oriented Attachment. *Adv. Mater.* **29**, 1–8 (2017).
6. Etgar, L., Gao, P., Xue, Z., Peng, Q., Chandiran, A. K., Liu, B., Nazeeruddin, M. K. & Grätzel, M. Mesoscopic CH₃NH₃PbI₃/TiO₂ Heterojunction Solar Cells. *J. Am. Chem. Soc.* **134**, 17396–17399. arXiv: ja307789s (2012).
7. Budzinauskas, K., Ewertowski, S., Olthof, S., Meerholz, K. & Van Loosdrecht, P. H. Charge carrier migration and hole extraction from MAPbI₃. *J. Phys. Conf. Ser.* **1220** (2019).
8. Kanemitsu, Y. Luminescence spectroscopy of lead-halide perovskites: materials properties and application as photovoltaic devices. *J. Mater. Chem. C* **5**, 3427–3437 (2017).

9. Budzinauskas, K., Versteeg, R. B., Montagnese, M., Luo, X., Cheong, S. W. & Loosdrecht, P. H. M. V. Spectroscopic investigation of the microscopic origin of the high carrier mobility of the transparent conducting oxide BaSnO₃:La Raman measurements High mobility. **102**, 172112 (2013).
10. Grosso, G. & Parravicini, P. *Solid State Physics* 857. arXiv: arXiv:1011.1669v3 (2014).
11. Yang, Y., Ostrowski, D. P., France, R. M., Zhu, K., van de Lagemaat, J., Luther, J. M. & Beard, M. C. Observation of a hot-phonon bottleneck in lead-iodide perovskites. *Nat. Photonics* **10**, 53–59 (2015).
12. Cardona, Peter Y. Yu. *Fundamentals of semiconductors: Physics and materials properties* (1997).
13. Elliott, R. J. Intensity of optical absorption by excitons. *Phys. Rev.* **108**, 1384–1389 (1957).
14. Li, Y., Yan, W., Li, Y., Wang, S., Wang, W., Bian, Z., Xiao, L. & Gong, Q. Direct Observation of Long Electron-Hole Diffusion Distance in CH₃NH₃PbI₃ Perovskite Thin Film. *Sci. Rep.* **5**, 14485 (2015).

Chapter 4

Charge carrier recombination dynamics in quadruple cations perovskites

In this chapter, a detailed study of carrier dynamics in photo-excited mixed halide, quadruple cation hybrid perovskites: $\text{GA}_{0.014}\text{Cs}_{0.043}\text{MA}_{0.13}\text{FA}_{0.73}\text{Pb}(\text{I}_{0.815}\text{Br}_{0.185})_3$ will be presented. We will discuss how different organic cations and halides affect both the crystal structure optoelectronic properties of the material. The crystal structure and chemical composition of the material was characterized using standard XRD and NMR methods. In our study optical spectroscopy methods were used to analyze equilibrium properties of the material such as the optical gap. The time resolved absorption was used to study dynamic processes in the material both in the femtosecond and in the microsecond domain. Using transient data and applying a parabolic band approximation, the reduced effective mass of $m^* = 0.14$ from the Burstein moss shift was deduced. By performing a fluence dependent study we were able to deduce intrinsic recombination properties of carriers with bi-molecular recombination rate of $1.2 \cdot 10^{-9} \text{ cm}^{-3}$ [1]. In the femtosecond domain it was shown that the lifetime of hot carriers is less then 500 fs. This finding was also confirmed by time resolved electron photoemission measurements (tr-PES).

Parts of this chapter was published in: E. Jung, K. Budzinauskas, S. Oez *et al.*, Femto - to microsecond dynamics of excited electrons in quadruple cation perovskite, ACS Energy Lett., **5**, 785-792 (2020).

4.1 Experimental results and discussion

4.1.1 Optical properties of mixed halide 4 cation perovskite

Our study was conducted on a $\text{GA}_{0.014}\text{Cs}_{0.043}\text{MA}_{0.13}\text{FA}_{0.73}\text{Pb}(\text{I}_{0.815}\text{Br}_{0.185})_3$ hybrid perovskite. It is a novel semiconducting material which allows both high stability and high carrier lifetime. To further elucidate on physical properties of such a material, optical spectroscopy methods were implemented. First, an optical absorption spectroscopy was performed to characterize the optical gap of the material by analyzing the absorption edge of the material. For this experiment, the perovskite material was spin coated on a quartz substrate according to the preparation procedure ascribed in [2].

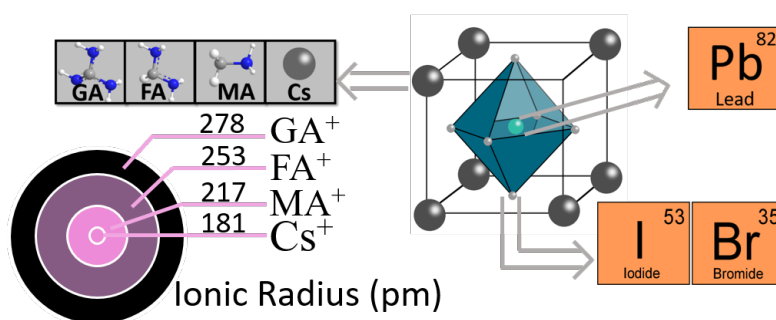


Figure 4.1: Schematic representation of the unit cell of organic-inorganic ABX_3 perovskite. A = organic or inorganic cations ($\text{MA}^+ = (\text{CH}_3\text{NH}_2)^{3+}$, $\text{FA}^+ = \text{formamidinium } \text{HC}(\text{NH}_2)^{2+}$, $\text{GA}^+ = \text{guanidinium } (\text{C}(\text{NH}_2)^{3+})$, Cs^+), B = Pb^{2+} and X = I^- , Br^- and ionic radius of different A⁺ site components.

The absorption spectrum of the 100 nm thick perovskite film of investigated perovskite is shown in the figure 4.2. From the absorption spectrum an optical gap of approximately 1.6 eV was deduced using the extrapolation to the x-axis. For the sake of clarity, the below gap absorption is not shown because of a strong Fabry-Perot oscillatory behavior near the gap which is typical for thin film samples. The gap energy is higher than a typical 1.47 eV [3] of a FAPbI_3 perovskite. The shift of the band gap is caused by halide and cation substitution. In the investigated perovskite, two halides were used: iodine (81.5%) and bromine (18.5%) and states of both elements strongly contribute to the optical transition at the band gap energy. A 3D crystal of a hybrid perovskite adopts similar electronic structure as the $[\text{Pb}(\text{I}/\text{Br})_6]^{4-}$ cluster (figure 4.2b) and can be used to simplify the electronic structure of the whole crystal. States from the bromine (Br) 4p as well as iodine (I) 5p orbitals with hybridization with lead (Pb) 6s are forming the electronic ground state of the perovskite. By applying a conventional Beer-Lambert law on absorption

spectrum of a sample with known thickness an absorption coefficient of 10^5 cm^{-1} was deduced similar to values found in the literature.[6] High absorption coefficient of hybrid perovskite in the visible range and UV range is partially responsible for its applicability as an absorber in the field of photovoltaic.

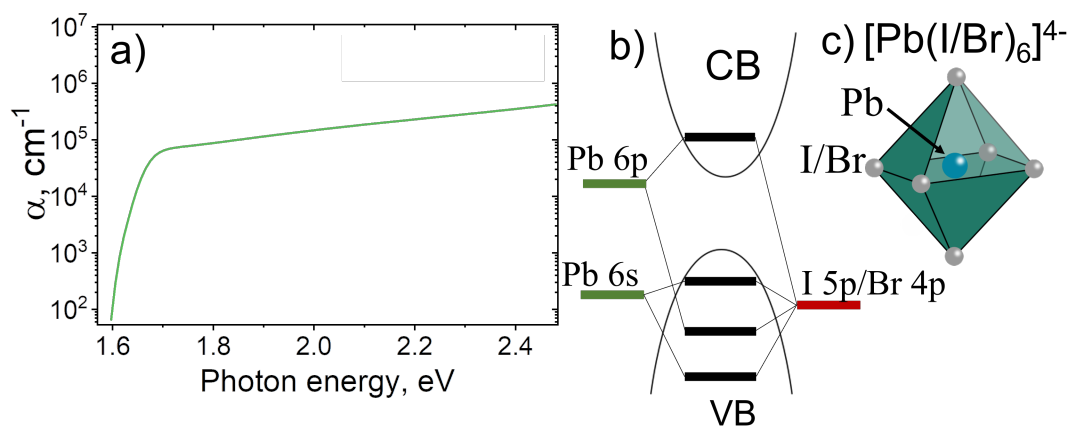


Figure 4.2: a) room temperature absorption spectrum of the 100 nm thick layer of GACsMAFA halide perovskite film, deposited on a quartz substrate b) orbitals, involved in the band gap transition in the studied perovskite c) a typical $[\text{Pb}(\text{I}/\text{Br})_6]^{4-}$ cluster.

4.2 Micro to nanosecond dynamics of excited electrons in quadruple cations perovskite

Metal-halide hybrid perovskites represent a family of crystalline compounds that possess crystal structure similar to the parent mineral CaTiO_3 . These materials can be thus generally described by the ABX_3 formula, where the A^+ and B^{2+} sites are occupied by monovalent, divalent or tetravalent cations and the X-site is occupied by negatively charged anions. Since their first demonstration in photovoltaic devices ten years ago as solution processed polycrystalline thin films, they have proven to be valuable in a wide range of optoelectronic applications such as light emission, lasing, radiation detection and even as media for energy storage, far beyond the classic solar light harvesting [4–9]. Nonetheless, most of these compounds face inherent as well as externally induced stability issues, which impair and retard their potential commercial applications despite several attempts made to overcome this inherent problem. The most promising results for polycrystalline thin films have been obtained by optimally intermixing different cations on the A-site and halide anions on the X-site of the ABX_3 hybrid perovskite structure. A

careful compositional engineering can result in to a cubic phase that: i) is stable within the operation temperature range of a photovoltaic device, ii) maintains a reasonably low band gap value and iii) displays low carrier recombination rates [10–15]. Such an approach allowed the fabrication of small area solar cells having high photoconversion efficiency and stable power output under 1000 hours of 1 sun (100 mW/cm^2) continuous irradiation [16, 17]. Most notably, the addition of guanidinium cations could modulate morphology and drastically alter charge recombination dynamics in hybrid perovskites by means of larger grain size, trap passivation and reduced hysteresis effects [12, 13, 17, 18]. Being inspired by recent reports, we have designed and realized a quadruple cation organic-inorganic mixed lead halide perovskite active layer, as well as single crystals, by mixing formamidinium (FA), methylammonium (MA), guanidinium (GA), and cesium (Cs) cations in the desired ratio ($\text{GA}_{0.014}\text{Cs}_{0.043}\text{MA}_{0.13}\text{FA}_{0.73}\text{Pb}(\text{I}_{0.815}\text{Br}_{0.185})_3$).^{8,9,11,16} The photovoltaic performances of GACsMAFA have been tested by fabricating a n-i-p type perovskite solar cell architecture with spiro-OMeTAD as the hole transporting material and compact-TiO₂/mesoporous TiO₂ layer as the electron selective contact. By optimization of the charge extraction at the electron-selective interface, we could achieve a photoconversion efficiency above 20% and negligible hysteresis. Due to the optimal mixing of different cations, the photovoltaic cells displayed a greatly improved operational stability with respect to $\text{CH}_3\text{NH}_3\text{PbI}_3$.

It is still an ongoing debate whether the introduction of multiple cations to the perovskite structure could alter the charge carrier dynamics and in particular the effect of trap passivating properties of guanidinium cations are not understood [13, 17]. When compared to the previous reports, the main novelty of this work lies in a thorough analysis of the carrier kinetics ranging from femtoseconds to microseconds in multiple cation mixed halide GACsMAFA crystals and films. By applying complementary pump-probe techniques, we show that an initial photo carrier induced reduction of the optical gap (also known as the band gap renormalization), takes place while carriers are in a highly non equilibrium state. We find no evidence of hot carriers having sizable excess energy and living on picosecond timescale in our quadruple cation samples. This controversial issue has recently been the focus of many experimental studies [19–21] on $\text{CH}_3\text{NH}_3\text{PbI}_3$ and has so far not been addressed in lead halide perovskites with multiple cations. After an ultrafast thermalization, the carriers recombine via radiative pathways at high photoexcitation density or by trap-assisted mechanisms in the low photoexcitation regime. The radiative recombination rate is comparable to the one of standard semiconductors with direct band gap and does not have significant effect in perovskite devices as long as

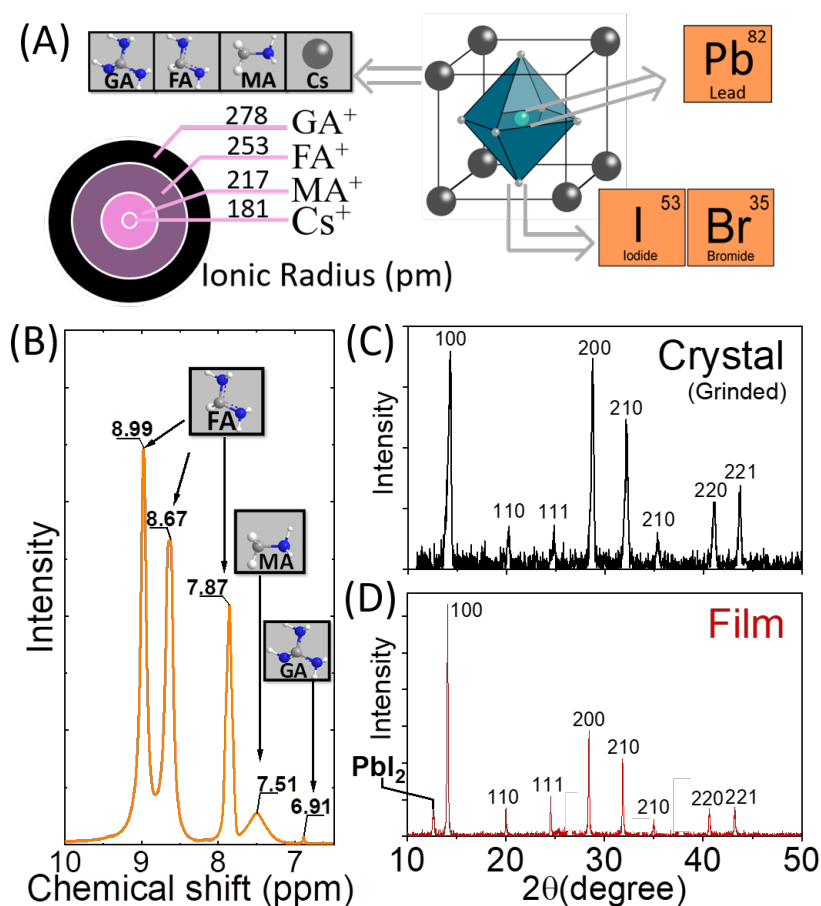


Figure 4.3: (A) Schematic representation of the unit cell of organic-inorganic ABX_3 perovskite. A = organic or inorganic cations (MA = $(CH_3NH_3^+)$, FA = formamidinium $(HC(NH_2)_2^+)$, GA = guanidinium $(C(NH_2)_3^+)$, Cs⁺), B = Pb²⁺ and X = I⁻, Br⁻ and ionic radius of different A⁻ site components. (B) Proton nuclear magnetic resonance (¹H NMR) spectra of single crystals dissolved in DMSO-d₆ show chemical shifts of the hydrogen signal characteristic for each of the organic cations. (C) Powder X-Ray Diffraction pattern (XRD) of the $GA_{0.014}Cs_{0.043}MA_{0.13}FA_{0.73}Pb(I_{0.815}Br_{0.185})_3$ ground single crystals. (D) XRD of the $GA_{0.014}Cs_{0.043}MA_{0.13}FA_{0.73}Pb(I_{0.815}Br_{0.185})_3$ thin film. The extra Bragg peak visible around 12.65 degrees is due to excess PbI₂ (5%). Reproduced from [1].

the carrier mobility remains high [22]. In agreement with previous reports,[4–7, 10] we found that inclusions of guanidinium cations in the perovskite mixture passivate the grain boundaries of thin films and increase the non-radiative recombination time up to the microsecond timescale. Finally, the evolution of band filling as a function of photoexcitation density has been employed to estimate the reduced effective mass near to the band edges. The derived value is comparable [23, 24] to the one reported for $CH_3NH_3PbI_3$ and suggests that excited electrons are large polarons with moderate or weak interaction with the lattice polarization [25].

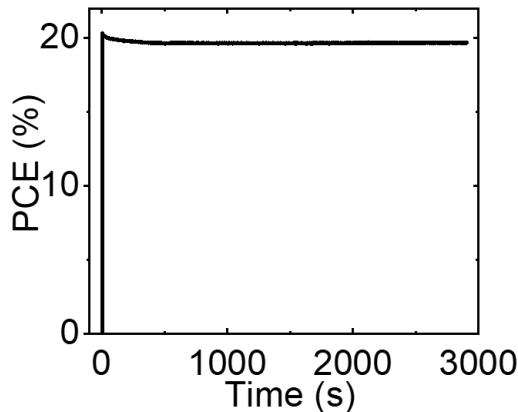


Figure 4.4: Maximum Power Point (MPP) tracking during the first hour under illumination AM1.5G 100 mW/cm². Reproduced from [1].

The quadruple cation $\text{GA}_{0.014}\text{Cs}_{0.043}\text{MA}_{0.13}\text{FA}_{0.73}\text{Pb}(\text{I}_{0.815}\text{Br}_{0.185})_3$ (GACsMAFA) perovskite (figure 4.3) has been synthesized as single crystals and as thin films. Each one of the cations covers a functional role in the active layer. The most studied perovskite is based on methylammonium (MA) cation, which is an excellent light harvester but suffers from its low thermal and chemical stability. As an example, direct contact of MA based perovskite with basic metal oxides like ZnO or Cu₂O can lead to deprotonation and subsequent formation of methylamine gas along with other products [26]. Formamidinium (FA) displays a broader absorption of the solar spectrum [27, 28] due to its lower band gap and high probability of forming hydrogen bonds [29]. In addition, the FA cation is less prone to deprotonation, when compared to MA, mostly due to the resonance stabilization effects. The optimal embedment of such cation stabilizes the pseudo-cubic or trigonal structure with respect to the tetragonal one that is observed for MAPbI₃ under standard conditions. Nonetheless, the FAPbI₃ perovskite is also prone to undergo phase transition into the non-photoactive hexagonal δ -phase [30]. This undesirable phase leads to a large bandgap insulator with unsuitable absorption properties for a photoactive layer. However, it is possible to hinder the formation of the δ -phase by incorporating small amounts of cesium cations as was recently demonstrated by Saliba *et al.* [30] The latter increases the structural stiffness, suppresses formation of undesired phases, improves thermal stability and distributes the halide mixture evenly throughout the material. Finally, guanidinium (GA) cation suppresses the formation of halide vacancies, and minimizes the non-radiative charge carrier recombination at grain boundaries [10]. GA cation is also very stable since the high pK_a (logarithmic acid dissociation constant) value of 13.6 makes any deprotonation process practically impossible. In our study, samples were prepared with 18.5%

of bromine and 81.5% of iodine. The chosen bromine and iodine ratio optimizes the optical gap while preserving a cubic structure. The relative concentration of the different cations plays a primary role on the crystal structure as well as on the endurance of the solar cells. We have designed the quadruple cation perovskite in order to achieve the highest possible structural stability. The effective Goldschmidt tolerance factor t_{eff} has been maintained very near to the recommended value for the crystallization in a cubic phase. The t_{eff} factor indicates the stability and distortion of the ABO_3 structure and can be calculated by using the radius of the A and B atom in the lattice: $t_{\text{eff}} = \frac{r_A + r_O}{\sqrt{2}(r_B + r_O)}$. We obtained $t_{\text{eff}} = 0.968$ from an optimal mix of cations in $\text{GA}_{0.014}\text{Cs}_{0.043}\text{MA}_{0.13}\text{FA}_{0.73}\text{Pb}(\text{I}_{0.815}\text{Br}_{0.185})_3$. After synthesis, the stoichiometry of the compound was verified by performing ^1H Nuclear Magnetic Resonance (NMR) spectroscopy on dissolved single crystals. The single crystal was washed with isopropyl alcohol before dissolve in DMSO-d6 to ensure removal of surface bound residues. The resonance peaks in the spectrum of figure 4.3b unambiguously identified FA, MA, and GA through the chemical shift of protons belonging to the respective $-\text{NH}_2$, $-\text{CH}$, $-\text{NH}_3^+$ and $-\text{CH}_3$ (not shown) groups of the hosting cations. The protons of $-\text{NH}_3^+$ (MA) group were observed at 7.51 ppm, while two peaks with identical integral were observed for the $=\text{NH}_2^{+/-}\text{NH}_2$ groups of the formamidinium cation at 8.99 and 8.67 ppm, respectively. The double peak structure of the $=\text{NH}_2^{+/-}\text{NH}_2$ resonance was only resolvable in a multiple scan NMR spectrum, which enables a resolution of 0.02ppm (figure 4.3b). The $-\text{CH}$ group of the FA cation peaked at 7.87 ppm. For the guanidinium cation a single peak at 6.91 ppm was detected, as expected for three chemically equivalent $-\text{NH}_2^{1/3+}$ groups. An accurate quantification of the individual components by peak integration indicated an excellent match with the intended composition.

The phase purity as well as the crystallinity of the compound has been investigated by X-ray diffractometry. The diffraction pattern of single crystal powders in figure 4.3c is compatible with a Pm-3m cubic structure with lattice parameter $a = 6.2185 \text{ \AA}$ ($V = 240.4677 \text{ \AA}^3$), which were derived from single crystal X-ray diffraction analysis performed using Mo- $K\alpha$ irradiation. We could not detect any signature of the undesirable δ -phase compound. As shown in the figure 4.3d, the X-ray diffraction plot of thin films is nearly identical to the one of the crystalline powders with only notable difference being an extra diffraction peak around 12.65 degrees that is ascribed to excess PbI_2 inclusions. Such minor PbI_2 component has been generated on purpose during the thin film synthesis, by adding an excess quantity of PbI_2 . In agreement with previous reports, [31] the enrichment with PbI_2 hinders the accumulation of organic species at the grain boundaries, favors an optimal embedding

of the grains and improves the transport of charge carriers.

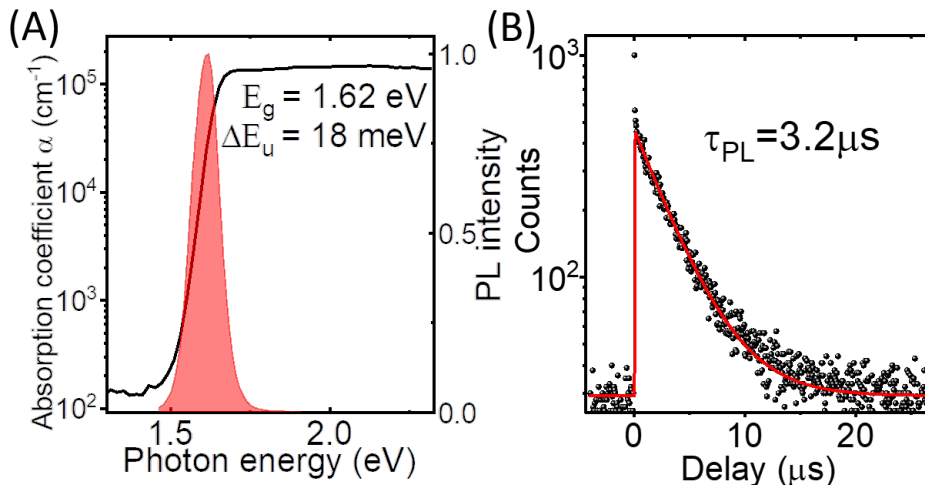


Figure 4.5: (A) The black solid line indicates the Photothermal Deflection Spectroscopy (PDS) measurement of the absorption coefficient as a function of the incident photon energy. The spectrum indicates a gap energy $E_g = 1.62$ eV and an Urbach energy $\Delta E_u = 18$ meV. The red area represents the photoluminescence intensity measured at room temperature as a function of emitted photon energy. (B) Time resolved photoluminescence, acquired at photon energy 1.62 eV and at room temperature as a function of delay time from the photoexcitation. Reproduced from [1].

4.2.1 Optical characterization

The GACsFAMA absorber has been characterized by different optical techniques. Photo-thermal Deflection Spectroscopy (PDS) has been performed to measure the light absorption of the perovskite films. The PDS spectrum in the figure 4.5a shows a sharp drop in absorption coefficient at the band gap value $E_g = 1.62$ eV (determined from photothermal deflection data by extrapolating the absorption edge). This finding is in agreement with recent reports on quadruple cations perovskites [11, 12]. Below 1.5 eV, the absorption coefficient is close to 10^2 cm⁻¹ while it reaches 10^5 cm⁻¹ at 1.7 eV. Below gap absorption coefficient is attributed to the photon absorption by shallow tail states. The exponential rise of absorption coefficient near the bandgap results in an Urbach energy $\Delta E_u = 18.5$ meV. For a typical MAPbI₃ perovskite the Urbach energy usually is 13 meV to 15 meV, indicating increased degree of disorder in GACsMAFA samples [32]. The steady-state photoluminescence (PL) shown in the figure 4.5a peaks at the band gap (1.62 eV) and leads to a sharp emission line. Figure 4.5b shows the temporal evolution of the photoluminescence

intensity measured at the gap value after a photoexcitation pulse with a density of $10^{12} - 10^{13} \text{ cm}^{-2}$. The curve can be well fitted by a step function multiplied with a single exponential decay function with a decay time of $\tau_{PL} = 3.2 \mu\text{s}$ together. The luminescence lifetime value is comparable to the relaxation time that has been previously reported for halide perovskite thin films incorporating guanidinium.[15] The increase of τ_{PL} in the presence of guanidinium confirms the efficient passivation of non-radiative recombination centers at the grain boundaries of the quadruple cation mixed halide perovskite. Overall, the suitable band gap, high absorption coefficient, small Urbach tail, and long carrier lifetime are favorable parameters for an efficient harvesting of the solar energy.

4.2.2 Transient absorption and photoemission

The initial dynamics of charge carriers after an ultrafast photoexcitation has been characterized by two different pump-probe experiments. Two-photon photoemission (2PPE) has been performed to observe the temporal evolution of the excited state in terms of kinetic energy of electrons [33]. Single crystals of GACsFAMA were cleaved and measured in ultrahigh vacuum. The entire experiment has been performed at the temperature of 180 K, in order to avoid the alteration of surface composition by possible sublimation of iodine or organic cations from the surface. The surface of the freshly cleaved crystal was photoexcited with a pump fluence of $8 \mu\text{J}/\text{cm}^2$, centered at 3 eV and the population of photoelectrons was probed with a subsequent pulse, centered at 4.5 eV. Figure 4.6a shows the pump-on minus pump off photoelectron intensity as a function of kinetic energy and pump-probe delay. The kinetic energy E_k has been referred to the vacuum level of the GACsFAMA surface but should be increased by 0.4 eV if referred to the spectrometer vacuum level. Around zero delay, primary electrons extend up to high kinetic energy and relax their excess energy until reaching the Conduction Band Minimum (CBM) at $E_k = 0.8 \text{ eV}$.

The characteristic timescale of such electronic cooling is 0.25 ps and matches the value measured in $\text{CH}_3\text{NH}_3\text{PbI}_3$ [34]. Such fast relaxation of the excited electrons is ascribed to highly dissipative collisions between electrons with large excess energy and the $-\text{NH}_2$, $-\text{CH}$, $-\text{NH}_3^+$, $-\text{CH}_3$ groups of the organic cations [34]. This efficient carrier cooling hinder any viable application of halide perovskites for the realization of hot carrier solar cells. In this context, we stress that a careful analysis of 2PPE spectra must be done to disentangle spurious components out of the measured signal. Beside the primary photoelectrons at $E_k > 0.8 \text{ eV}$, an additional intensity is indeed detected for $0 \text{ eV} < E_k < 0.8 \text{ eV}$. We ascribe this Secondary Electrons Replica (SER) to photoelectrons experiencing inelastic scattering events while propagating

from the sample out in the vacuum region. The SER can be viewed as an artifact of the measurement and carries no information about the energy of excited electrons in the solid. Next, we characterized the ultrafast electron relaxation by time-resolved transient absorption at room temperature. Thin films of GACsFAMA have been probed using a white light continuum and pumped by a femtosecond pulse centered a 2.5 eV. Figure 4.6b shows that band filling effect reduces the absorption around 1.68 eV due to Pauli blocking [23].

In addition to this bleaching effect, a transient increase of optical absorption occurs at 1.62 eV at early delay time. The dynamical screening of the electron-electron interaction in the photoexcited state is the main reason of such Band Gap Renormalization [35]. Remarkably, the good matching between the duration of BGR in the figure 4.6b and the duration of electronic cooling in the figure 4.6a indicates that BGR takes place while the electrons and holes are in a highly non thermal state. This result is somehow expected. Being driven by changes of dielectric function, the BGR is largest when the non-equilibrium electronic distribution opens a large amount intraband scattering channels. This condition is no longer verified after roughly 0.5 ps, once the carriers have been fully thermalized.

On the longer timescale the dynamics is ruled by a reduction of photinduced band filling (PBF) due to carrier recombination. We show in the figure 4.6c the decay of the PBF for different excitation density between $F \leq 3.7 \cdot 10^{16} \text{ cm}^{-3}$ and $F \geq 7.5 \cdot 10^{17} \text{ cm}^{-3}$. The entire data set can be fit globally by standard rate equation $-dN/dt = aN + bN^2$ with a Shockley-Read-Hall trap recombination rate of $a = 3 \cdot 10^5 \text{ 1/s}$ and radiative recombination coefficient $b = 1.2 \cdot 10^{-9} \text{ cm}^3/\text{s}$ [36, 37]. This value of radiative recombination is slightly higher compared to the radiative recombination rate reported in other halide perovskites,[38] however, as it was shown by other authors, carrier recombination rate has less effect on photovoltaic properties in materials with high carrier mobilities [22]. It is often being wrongly argued that the high efficiency of lead-halide perovskite solar cells is due to the exceptionally slow radiative recombination rates, five orders of magnitude lower than predicted by a Langevin model [39]. The latter has been ascribed to a slightly indirect band gap originating from dynamical effects [40]. Due to thermal fluctuations, the rotation of organic cations may induce a momentum mismatch between the band edges [41, 42]. Despite such proposals, recent calculations suggest that the indirect nature of the band gap suppresses the radiative recombination rate by less than a factor of two [43]. This suppression would not affect the efficiency of a perovskite solar cell as long as the carrier mobilities remain modest ($> 4 \cdot 10^{-3} \text{ cm}^2/\text{Vs}$) [22]. In agreement with this finding, we stress that the radiative recombination coefficient of GACsFAMA

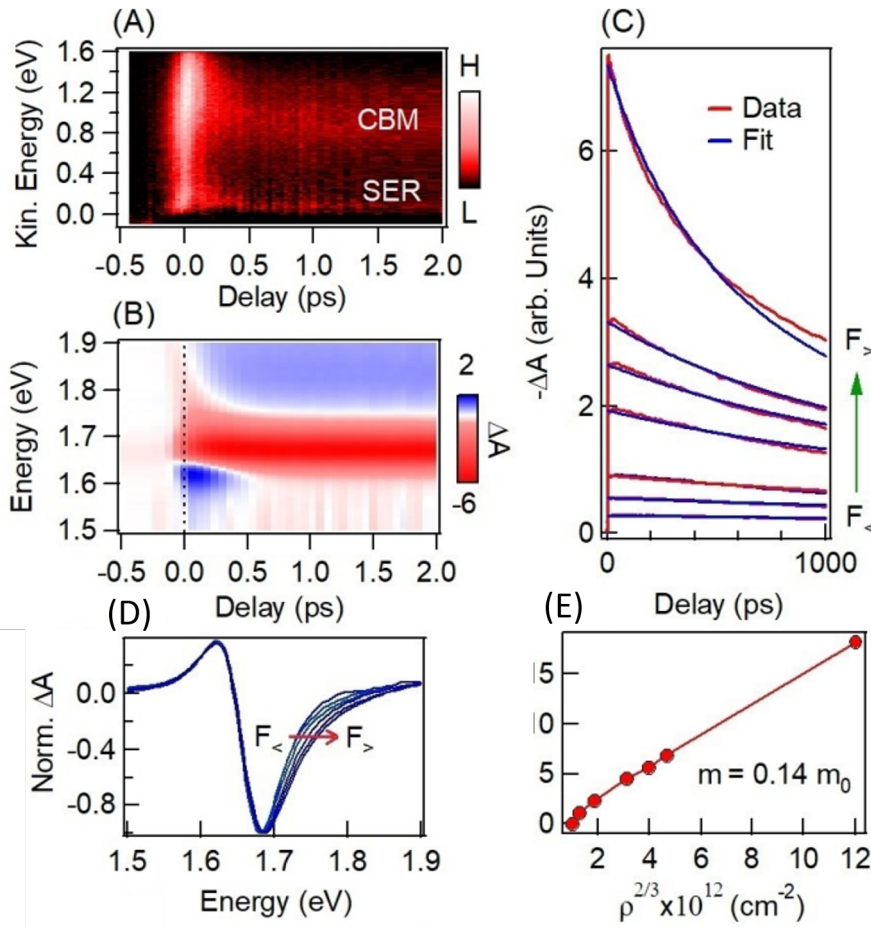


Figure 4.6: Two photon photoemission spectroscopy (2PPE) measured on a GACsFAMA single crystal. The sample is excited with a pulse centered at 3 eV and photoelectrons are emitted by probe pulse centered at 4.5 eV. Pump on minus pump off signal of primary electrons in the Conduction Band Minimum and Secondary Electrons Replica (SER) are marked directly on the image. (B) Differential absorption of a supercontinuum spectrum measured on a GACsFAMA thin film as a function of pump-probe delay. The pump pulse is centered at 2.5 eV and induces an excitation density of $8.7 \cdot 10^{16} \text{ cm}^{-3}$. (C) Differential absorption decay extracted at 1.68 eV after a pump pulse centered at 2.5 eV and with different fluence values. The traces have been acquired for an excitation density spanning from $3.7 \cdot 10^{16}$ to $7.5 \cdot 10^{17} \text{ cm}^{-3}$. Red curves are the experimental data while blue curves are fits obtained via a recombination model. (D) Renormalized traces of the time-resolved transient absorption spectra acquired at pump probe delay of 0.1 ps, for increasing photoexcitation density (E) The broadening of transient absorption peak (red dots) is plot against the photoexcitation density $\rho^{(2/3)}$. Reproduced from [1].

is as high as in Gallium Arsenide (GaAs), which is a traditional semiconductor with direct band gap [44]. Moreover, the long carrier lifetime observed in 4.5b and the high PCE in 4.5 imply that radiative recombination has no impact on the

overall performance of the GACsFAMA solar cell. In the figure 4.6d, we show the normalized transient absorption that has been measured just after photoexcitation at different pump fluence. By increasing photoexcitation density, we observe a blue shift and broadening of the PBF peak [23, 24]. This dynamical Burstein-Moss effect is a consequence of the excited distribution of electron in the conduction band and holes in the valence band. It can be described by an effective filling level leading to Pauli blocking of the optical transitions in an energy interval $\Delta E_{BM} = \frac{\hbar^2}{2m_{eh}^*} (3\pi^2 N)^{2/3}$ from the bandgap value. Here, m_{eh}^* is the reduced effective mass and N is the photoexcitation density. Figure 4.6e shows the experimental broadening of PBF as a function of the excitation density to the power of $2/3$. The curve is non-linear in the low fluence regime, correlated with trap filling mechanism, and linear at elevated fluence, where band-to-band recombination becomes dominant. The linear dependence observed in a wide fluence range is consistent with the simple Burstein Moss model. From the slope of the linear fit we extract a reduced effective mass $m_{eh}^* = 0.14 m_0$ (where m_0 is the bare electron mass). This value is consistent with the $0.1 m_0 - 0.3 m_0$ [23, 24] reported in $\text{CH}_3\text{NH}_3\text{PbI}_3$ or other perovskites. The relatively small value of the reduced mass, long carrier lifetime and modest diffusion rate are in good agreement with ab-initio calculations suggest a moderate dressing of GACsFAMA carriers by the lattice polarization [25].

4.2.3 Conclusions

In conclusion, we reported a detailed chemical and time resolved spectroscopic analysis of a quadruple cation mixed halide $\text{GA}_{0.014}\text{Cs}_{0.043}\text{MA}_{0.13}\text{FA}_{0.73}\text{Pb}(\text{I}_{0.815}\text{Br}_{0.185})_3$ perovskite and comparatively analyze the micro- to femtosecond photodynamics in polycrystalline and single crystal samples. Our solar cells based on this active layer reach photovoltaic efficiencies above 20% and high operational stability. By making use of complementary ultrafast techniques, we show that both hot carrier cooling and bandgap renormalization occur on the sub-picosecond timescale. The radiative recombination of $\text{GA}_{0.014}\text{Cs}_{0.043}\text{MA}_{0.13}\text{FA}_{0.73}\text{Pb}(\text{I}_{0.815}\text{Br}_{0.185})_3$ is higher than the one of $\text{CH}_3\text{NH}_3\text{PbI}_3$ but has no role on the photovoltaic performances of solar cells due to good carrier transport properties [22]. Moreover guanidinium cations passivate recombination centers at the grain boundaries and increases the lifetime of charge carriers up to the microsecond timescale.

Collaborations

The work presented in this chapter has been performed in a collaboration with Dr. Eunwan Jun and Dr. Senol Oez (sample growing, solar cell characterization, NMR), Luca Perfetti and Marie Cheresse (time resolved photoemission experiments), Thomas Kirchartz (photothermal deflection and time resolved luminescence). The text was written by me and Marie Cheresse with input from Luca Perfetti and Senol Oez and Eunwan Jun.

References

1. Jung, E. *et al.* Femto- To Microsecond Dynamics of Excited Electrons in a Quadruple Cation Perovskite. *ACS Energy Lett.* **5**, 785–792 (2020).
2. Aversa, P., Öz, S., Jung, E., Plantevin, O., Cavani, O., Ollier, N., Geffroy, B., Mathur, S. & Corbel, C. Radiative Recombination in Quadruple Cation Organic-Inorganic Mixed Halide Perovskite Layers: Electron Irradiation Induced Ageing Effects (2019).
3. Koh, T. M., Fu, K., Fang, Y., Chen, S., Sum, T. C., Mathews, N., Mhaisalkar, S. G., Boix, P. P. & Baikie, T. Formamidinium-Containing Metal-Halide: An Alternative Material for Near-IR Absorption Perovskite Solar Cells. *J. Phys. Chem. C* **118**, 16458–16462 (2014).
4. Zhang, L., Yang, X., Jiang, Q., Wang, P., Yin, Z., Zhang, X., Tan, H., Yang, Y. M., Wei, M., Sutherland, B. R., Sargent, E. H. & You, J. Ultra-bright and highly efficient inorganic based perovskite light-emitting diodes. *Nat. Commun.* **8**, 1–8 (2017).
5. Kojima, A., Teshima, K., Shirai, Y. & Miyasaka, T. Organometal Halide Perovskites as Visible-Light Sensitizers for Photovoltaic Cells. *J. Am. Chem. Soc.* **131**, 6050–6051 (2009).
6. Leyden, M. R., Meng, L., Jiang, Y., Ono, L. K., Qiu, L., Juarez-Perez, E. J., Qin, C., Adachi, C. & Qi, Y. Methylammonium Lead Bromide Perovskite Light-Emitting Diodes by Chemical Vapor Deposition. *J. Phys. Chem. Lett.* **8**, 3193–3198 (2017).
7. He, Y., Matei, L., Jung, H. J., McCall, K. M., Chen, M., Stoumpos, C. C., Liu, Z., Peters, J. A., Chung, D. Y., Wessels, B. W., Wasielewski, M. R., Dravid, V. P., Burger, A. & Kanatzidis, M. G. High spectral resolution of gamma-rays

- at room temperature by perovskite CsPbBr₃ single crystals. *Nat. Commun.* **9**, 1–8 (2018).
8. Tathavadekar, M., Krishnamurthy, S., Banerjee, A., Nagane, S., Gawli, Y., Suryawanshi, A., Bhat, S., Puthusseri, D., Mohite, A. D. & Ogale, S. Low-dimensional hybrid perovskites as high performance anodes for alkali-ion batteries. *J. Mater. Chem. A* **5**, 18634–18642 (2017).
 9. Ha, S. T., Zhang, Q., Zhao, L., Su, R., Du, W., Liu, X. & Xiong, Q. *Advances in Small Perovskite-Based Lasers* 2017.
 10. Marco, N. D., Zhou, H., Chen, Q., Sun, P., Liu, Z., Meng, L., Yao, E. P., Liu, Y., Schiffer, A. & Yang, Y. Guanidinium: A Route to Enhanced Carrier Lifetime and Open-Circuit Voltage in Hybrid Perovskite Solar Cells. *Nano Lett.* **16**, 1009–1016 (2016).
 11. Wu, S., Li, Z., Zhang, J., Liu, T., Zhu, Z. & Jen, A. K. Efficient large guanidinium mixed perovskite solar cells with enhanced photovoltage and low energy losses. *Chem. Commun.* **55**, 4315–4318 (2019).
 12. Zhang, W., Xiong, J., Li, J. & Daoud, W. A. Guanidinium induced phase separated perovskite layer for efficient and highly stable solar cells. *J. Mater. Chem. A* **7**, 9486–9496 (2019).
 13. Yao, J., Wang, H., Wang, P., Gurney, R. S., Intaniwet, A., Ruankham, P., Chooapun, S., Liu, D. & Wang, T. Trap passivation and efficiency improvement of perovskite solar cells by a guanidinium additive. *Mater. Chem. Front.* **3**, 1357–1364 (2019).
 14. Kubicki, D. J., Prochowicz, D., Hofstetter, A., Sasaki, M., Yadav, P., Bi, D., Pellet, N., Lewiński, J., Zakeeruddin, S. M., Grätzel, M. & Emsley, L. Formation of Stable Mixed Guanidinium–Methylammonium Phases with Exceptionally Long Carrier Lifetimes for High-Efficiency Lead Iodide-Based Perovskite Photovoltaics. *J. Am. Chem. Soc.* **140**, 3345–3351 (2018).
 15. Christians, J. A., Schulz, P., Tinkham, J. S., Schloemer, T. H., Harvey, S. P., Tremolet de Villers, B. J., Sellinger, A., Berry, J. J. & Luther, J. M. Tailored interfaces of unencapsulated perovskite solar cells for > 1,000 hour operational stability. *Nat. Energy* **3**, 68–74 (2018).
 16. Bai, S., Da, P., Li, C., Wang, Z., Yuan, Z., Fu, F., Kawecki, M., Liu, X., Sakai, N., Wang, J. T.-W., Huettner, S., Buecheler, S., Fahlman, M., Gao, F. & Snaith, H. J. Planar perovskite solar cells with long-term stability using ionic liquid additives. *Nature* **571**, 245–250 (2019).

17. Pham, N. D., Zhang, C., Tiong, V. T., Zhang, S., Will, G., Bou, A., Bisquert, J., Shaw, P. E., Du, A., Wilson, G. J. & Wang, H. Tailoring Crystal Structure of $\text{FA}_{0.83}\text{Cs}_{0.17}\text{PbI}_3$ Perovskite Through Guanidinium Doping for Enhanced Performance and Tunable Hysteresis of Planar Perovskite Solar Cells. *Adv. Funct. Mater.* **29**, 1806479 (2019).
18. Hou, X., Hu, Y., Liu, H., Mei, A., Li, X., Duan, M., Zhang, G., Rong, Y. & Han, H. Effect of guanidinium on mesoscopic perovskite solar cells. *J. Mater. Chem. A* **5**, 73–78 (2017).
19. Niesner, D., Zhu, H., Miyata, K., Joshi, P. P., Evans, T. J. S., Kudisch, B. J., Trinh, M. T., Marks, M. & Zhu, X.-Y. Persistent Energetic Electrons in Methylammonium Lead Iodide Perovskite Thin Films. *J. Am. Chem. Soc.* **138**, 15717–15726 (2016).
20. Chen, Z., Lee, M. I., Zhang, Z., Diab, H., Garrot, D., Lédée, F., Fertey, P., Papalazarou, E., Marsi, M., Ponceca, C., Deleporte, E., Tejeda, A. & Perfetti, L. Time-resolved photoemission spectroscopy of electronic cooling and localization in $\text{CH}_3\text{NH}_3\text{PbI}_3$ crystals. *Phys. Rev. Mater.* **1**, 1–6 (2017).
21. Chen, K., Barker, A. J., Morgan, F. L. C., Halpert, J. E. & Hodgkiss, J. M. Effect of carrier thermalization dynamics on light emission and amplification in organometal halide perovskites. *J. Phys. Chem. Lett.* **6**, 153–158 (2015).
22. Kirchartz, T., Krückemeier, L. & Unger, E. L. Research Update: Recombination and open-circuit voltage in lead-halide perovskites. *APL Mater.* **6**, 100702 (2018).
23. Manser, J. S. & Kamat, P. V. Band filling with free charge carriers in organometal halide perovskites. *Nat. Photonics* **8**, 737–743 (2014).
24. Zeng, X.-H., Cheng, L.-W., Tanaka, K., Yang, J.-P., Zhang, X.-Y., Kera, S., Ideta, S., Ueno, N., Yamaguchi, T., Ueba, T. & Meissner, M. Band Dispersion and Hole Effective Mass of Methylammonium Lead Iodide Perovskite. *Sol. RRL* **2**, 1800132 (2018).
25. Park, M., Neukirch, A. J., Reyes-Lillo, S. E., Lai, M., Ellis, S. R., Dietze, D., Neaton, J. B., Yang, P., Tretiak, S. & Mathies, R. A. Excited-state vibrational dynamics toward the polaron in methylammonium lead iodide perovskite. *Nat. Commun.* **9**, 2525 (2018).
26. Yang, J., Siempelkamp, B. D., Mosconi, E., De Angelis, F. & Kelly, T. L. Origin of the Thermal Instability in $\text{CH}_3\text{NH}_3\text{PbI}_3$ Thin Films Deposited on ZnO. *Chem. Mater.* **27**, 4229–4236 (2015).

27. Han, Q., Bae, S.-H., Sun, P., Hsieh, Y.-T., Yang, Y. M., Rim, Y. S., Zhao, H., Chen, Q., Shi, W., Li, G. & Yang, Y. Single Crystal Formamidinium Lead Iodide (FAPbI₃): Insight into the Structural, Optical, and Electrical Properties. *Adv. Mater.* **28**, 2253–2258 (2016).
28. Eperon, G. E., Stranks, S. D., Menelaou, C., Johnston, M. B., Herz, L. M. & Snaith, H. J. Formamidinium lead trihalide: a broadly tunable perovskite for efficient planar heterojunction solar cells. *Energy Environ. Sci.* **7**, 982 (2014).
29. Amat, A., Mosconi, E., Ronca, E., Quarti, C., Umari, P., Nazeeruddin, M. K., Grätzel, M. & De Angelis, F. Cation-Induced Band-Gap Tuning in Organohalide Perovskites: Interplay of Spin–Orbit Coupling and Octahedra Tilting. *Nano Lett.* **14**, 3608–3616 (2014).
30. Saliba, M., Matsui, T., Seo, J.-Y., Domanski, K., Correa-Baena, J.-P., Nazeeruddin, M. K., Zakeeruddin, S. M., Tress, W., Abate, A., Hagfeldt, A. & Grätzel, M. Cesium-containing triple cation perovskite solar cells: improved stability, reproducibility and high efficiency. *Energy Environ. Sci.* **9**, 1989–1997. arXiv: arXiv:1408.1149 (2016).
31. Jacobsson, T. J., Correa-Baena, J.-P., Halvani Anaraki, E., Philippe, B., Stranks, S. D., Bouduban, M. E. F., Tress, W., Schenk, K., Teuscher, J., Moser, J.-E., Rensmo, H. & Hagfeldt, A. Unreacted PbI₂ as a Double-Edged Sword for Enhancing the Performance of Perovskite Solar Cells. *J. Am. Chem. Soc.* **138**, 10331–10343 (2016).
32. De Wolf, S., Holovsky, J., Moon, S. J., Löper, P., Niesen, B., Ledinsky, M., Haug, F. J., Yum, J. H. & Ballif, C. Organometallic halide perovskites: Sharp optical absorption edge and its relation to photovoltaic performance. *J. Phys. Chem. Lett.* **5**, 1035–1039 (2014).
33. Faure, J., Mauchain, J., Papalazarou, E., Yan, W., Pinon, J., Marsi, M. & Perfetti, L. Full characterization and optimization of a femtosecond ultraviolet laser source for time and angle-resolved photoemission on solid surfaces. *Rev. Sci. Instrum.* **83**, 043109 (2012).
34. Chen, T., Chen, W.-L., Foley, B. J., Lee, J., Ruff, J. P. C., Ko, J. Y. P., Brown, C. M., Harriger, L. W., Zhang, D., Park, C., Yoon, M., Chang, Y.-M., Choi, J. J. & Lee, S.-H. Origin of long lifetime of band-edge charge carriers in organic–inorganic lead iodide perovskites. *Proc. Natl. Acad. Sci.* **114**, 201704421 (2017).

35. Chen, Q., De Marco, N., Yang, Y., Song, T. B., Chen, C. C., Zhao, H., Hong, Z., Zhou, H. & Yang, Y. Under the spotlight: The organic-inorganic hybrid halide perovskite for optoelectronic applications. *Nano Today* **10**, 355–396 (2015).
36. Staub, F., Hempel, H., Hebig, J.-C., Mock, J., Paetzold, U. W., Rau, U., Unold, T. & Kirchartz, T. Beyond Bulk Lifetimes: Insights into Lead Halide Perovskite Films from Time-Resolved Photoluminescence. *Phys. Rev. Appl.* **6**, 044017 (2016).
37. Crothers, T. W., Milot, R. L., Patel, J. B., Parrott, E. S., Schlipf, J., Müller-Buschbaum, P., Johnston, M. B. & Herz, L. M. Photon Reabsorption Masks Intrinsic Bimolecular Charge-Carrier Recombination in $\text{CH}_3\text{NH}_3\text{PbI}_3$ Perovskite. *Nano Lett.* **17**, 5782–5789 (2017).
38. Kirchartz, T. High open-circuit voltages in lead-halide perovskite solar cells: experiment, theory and open questions. *Philos. Trans. R. Soc. A Math. Phys. Eng. Sci.* **377**, 20180286. arXiv: 1904.08752 (2019).
39. Wehrenfennig, C., Eperon, G. E., Johnston, M. B., Snaith, H. J. & Herz, L. M. High Charge Carrier Mobilities and Lifetimes in Organolead Trihalide Perovskites. *Adv. Mater.* **26**, 1584–1589 (2014).
40. Liu, S., Zheng, F., Koocher, N. Z., Takenaka, H., Wang, F. & Rappe, A. M. Ferroelectric domain wall induced band gap reduction and charge separation in organometal halide perovskites. *J. Phys. Chem. Lett.* **6**, 693–699 (2015).
41. Zheng, F., Takenaka, H., Wang, F., Koocher, N. Z. & Rappe, A. M. First-Principles Calculation of the Bulk Photovoltaic Effect in $\text{CH}_3\text{NH}_3\text{PbI}_3$ and $\text{CH}_3\text{NH}_3\text{PbI}_{3-x}\text{Cl}_x$. *J. Phys. Chem. Lett.* **6**, 31–37. arXiv: 1503.00684 (2015).
42. Niesner, D., Wilhelm, M., Levchuk, I., Osvet, A., Shrestha, S., Batentschuk, M., Brabec, C. & Fauster, T. Giant Rashba Splitting in CH_3NH_3 Organic-Inorganic Perovskite. *Phys. Rev. Lett.* **117**, 126401. arXiv: 1606.05867 (2016).
43. Zhang, X., Shen, J.-X., Wang, W. & Van de Walle, C. G. First-Principles Analysis of Radiative Recombination in Lead-Halide Perovskites. *ACS Energy Lett.* **3**, 2329–2334 (2018).
44. 't Hooft, G. W. The radiative recombination coefficient of GaAs from laser delay measurements and effective nonradiative carrier lifetimes. *Appl. Phys. Lett.* **39**, 389–390 (1981).

Chapter 5

Molecular H-aggregate formation in merocyanine chromophores

In this chapter a study on solvatochromism and aggregation properties in merocyanine molecules will be presented. The main goal of this study was to understand how different polymethine chains affect molecular properties liquid and solid phase. Solvatochromic behavior of merocyanine dyes with different solvents was investigated using an absorption spectroscopy. The vibronic structure of the molecule was analyzed and modeled. The vibronic energy of 150 meV was assigned to the C-C stretching mode in the polymethine chain. It was found that the solvatochromic behavior in merocyanine molecules follows the classical Onsager formalism and the 0-0 transition position shift in different solvents follows the empirical Reichardt's ET₃₀ scale. By mixing water (bad solvent for merocyanine) with acetone we were able to get H-aggregates of merocyanine molecules and measure their optical properties using absorption spectroscopy. A distinct blue shifted H-aggregate spectral feature allowed to deduce the H-aggregate coupling energy of 250 meV. In films, similar aggregation behavior was observed. It was found that with introduction of PC₆₁BM molecules in merocyanine:PC₆₁BM blend created molecular hindrance effect which hinders the H-aggregate formation.¹

¹Parts of this chapter were published in: K. Budzinauskas *et al.*, Impact of the interfacial molecular structure organization on the charge transfer state formation and exciton delocalization in merocyanine:PC₆₁BM Blends, *J. Phys. Chem. C*, **124**, 21978-21984 (2020).

In recent years, a great scientific effort for better understanding the relationship between chemical structure and device properties was made. For instance, the effect of different sidechains was found to be very important for molecular packing, orientation and highly affecting the overall morphology of bulk hetero junction molecular films [1–3]. One of the most efficient ways for altering molecular packing in BHJ devices is by introducing different alkyl chain branching[4, 5]. Despite numerous efforts, the underlying correlation between chemical structure and morphology of organic films remains hard to address, since the growing process and subtle variations in deposition variables alter the microstructure, morphology and performance of a functioning organic device. Moreover, the correlations between chemical structure and molecular packing are highly dependent on studied molecular compound and usually apply only for a specific molecule or polymer. Despite that, this field of molecular packing focused chemical engineering is very important for gaining insights into the molecular packing induced property changes and can be broadly adapted to design future devices with higher efficiencies.

In the field of organic photovoltaics, the usual fabrication methods involve the solution-processing techniques which could lead to disordered complex structures with varying morphology and domain size. The usual toolbox for tuning these properties via molecular orientation and intermolecular orientation for organic molecules and polymers involve different organic groups attached to the backbone of the molecule or a polymer. In fact, the variety of possible sidechains which could be attached to the organic molecule is important for the scientific community in the field of organic photovoltaics because it gives large degree of tunability in the means of various physical properties. One of the ways for introducing different sidechains is by applying different solvents in the preparation procedure, for example the fluorination in PNDT-DTBT, PBnDT-DTBT and PBnDT-TAZ polymers in bulk heterojunction solar cells by applying chlorobenzene and dichlorobenzene solvents [6]. Molecular orientation study with energy dependent anisotropic scattering from polarized X-ray, revealed differences in fluorinated and non-fluorinated sidechains. It was also reported that a strong correlation between molecular orientation and device properties such as V_{oc} and FF persist. It was found that at the donor/acceptor interface polymers show either face-on or edge-on orientation with respect to the PC₆₁BM and that is one of the reasons for drastic changes in device performance. A continuation of this work by Zhou *et al.* led to the similar results for PTBT-th polymers, where face-on and edge-on orientation were achieved by solvent treatment [7].

5.1 Optical absorption properties of investigated merocyanine films

Cyanine dyes are molecular systems with two nitrogen centers, one of which is positively charged and connected with a polymethine chain with odd number of carbon atoms. Merocyanine molecules are a class of molecules, structurally similar to cyanine dyes. Brookers merocyanine is one of the best known merocyanine molecule. Due to its solvatochromic sensitivity it is used to determine polarity of different solvents and for selective staining of different cells[8]

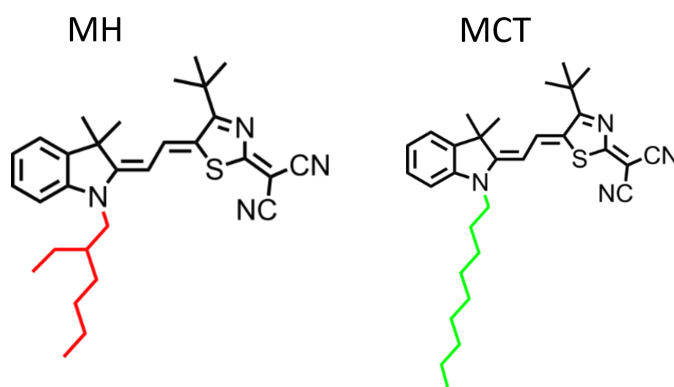


Figure 5.1: Structure of the investigated merocyanine molecule MCT and MH. and MH: 2-((Z)-4-tert-butyl-5-((E)-2-(3,3-dimethyl-1-nonylindolin-2-ylidene)ethylidene)thiazol-2(5H)-ylidene)malononitrile.

Another important aspect of merocyanine molecules is their strong ground state dipole moment which leads to a strong intermolecular interaction. Molecules with a strong intermolecular interaction can self-assemble to H and J type aggregates [9–12]. A complex interaction between individual merocyanine chromophores is of particular importance for supramolecular chemistry, where different merocyanine chromophores are used to make self-assembled molecular devices such as molecular tweezers [12]. In typical push:pull molecules the π system is end-capped with electron donor and acceptor substituents implementing mesomeric effects. Optical properties of these kind of molecules depend on the donor:acceptor strength, which lead to intramolecular charge transfer (ICT) state. The formation of ICT depends on the interaction between donor and acceptor, which can be controlled by the π spacer.

In this study two different merocyanine type push:pull chromophores were used having a linear structure. The difference between two molecules being the additional alkyl sidechains to a push:pull type molecular backbone. The structure of

investigated MCT² and MH³ molecules is shown in the figure 5.1

Polymethine spacer also can be used to control both the transition energy and oscillator strength by means of controlling the interaction between donor and acceptor substituent.[13] Also it is worth mentioning that ICT is responsible for the generation of molecular dipole in push-pull molecules. The same molecular push:pull backbone, responsible for optical transitions in both molecules was used. Difference in attached alkyl chains which are depicted in different colors in the figure 5.1. These additional alkyl chains predetermine the different molecular packing properties of the chromophores. These specially designed molecules will allow to investigate, how different molecular packing can alter both optical and electronic properties of ICT transitions in investigated molecular systems.

5.1.1 Merocyanine molecules and their vibronic properties

In this section we briefly discuss optical properties of merocyanine molecules. To understand photophysics of dye molecules it is critical to understand their optical properties. For this reason, MCT dye was dissolved in methanol at low molar concentration to avoid molecule-molecule interactions. The absorption spectrum of MCT type merocyanine dissolved in methanol CH₃OH with a molar concentration of 10⁻⁵ mol/l is shown in the figure 5.2. In the linear absorption spectrum, clear vibrational repetitions arise.

The optical density spectra of investigated molecule shows a pronounced vibronic repetition with a periodicity of 1290 cm⁻¹ (150 meV). These molecular vibrations arise from the C-C stretching mode of the polymethine chain in the electronic excited state. This highlights that optical properties of merocyanine molecules arise from donor acceptor moieties and are sensitive to the modulation of distance between them. Vibronic transitions with similar frequencies were reported in other cyanine dyes with a polymethine chain connecting donor and acceptor moieties in a push:pull molecule[14, 15].

Another important aspect of merocyanine absorption spectrum to consider is the spectral broadening of larger order vibronic transitions. A progressive linewidth increase with energy is a known phenomenon in systems where a strong intermolecular interaction is present. It was shown by Spano *et al.*, that vibronic repetition of tetraazaterrylene molecules shows a clusterization of closely packed vibronic transitions that emerge to a linewidth and causes a dispersion of vibronic energies[16].

²2-((Z)-4-tert-butyl-5-((E)-2-(3,3-dimethyl-1-(2-ethylhexyl)indolin-2-ylidene)ethylidene)thiazol-2(5H)-ylidene)malononitrile

³2-((Z)-4-tert-butyl-5-((E)-2-(3,3-dimethyl-1-nonylindolin-2-ylidene) ethylidene) thiazol-2(5H)-ylidene) malononitrile

This kind of behavior is expected in systems where main phonon, involved in vibronic transitions can have broadening effects. In case of cyanine dyes, the main vibronic feature is the vibration of the polymethine chain. Its vibration energy depends on a relative tilting or rotation of donor, acceptor moieties of cyanine dye. In case of distribution of several orientations, a similar behavior is expected. Similar linewidths increase with energy was observed in the investigated merocyanine molecules as well. The spectral fit of MCT molecules, dissolved in methanol resulted in linewidth progression $\Delta\Gamma$ of 20 meV so overall spectra follows the $\Gamma + \tilde{\nu}\Delta\Gamma$, where $\tilde{\nu}$ is a vibronic repetition and the linewidth of the 0 – 0 vibronic transition $\Gamma = 45$ meV.

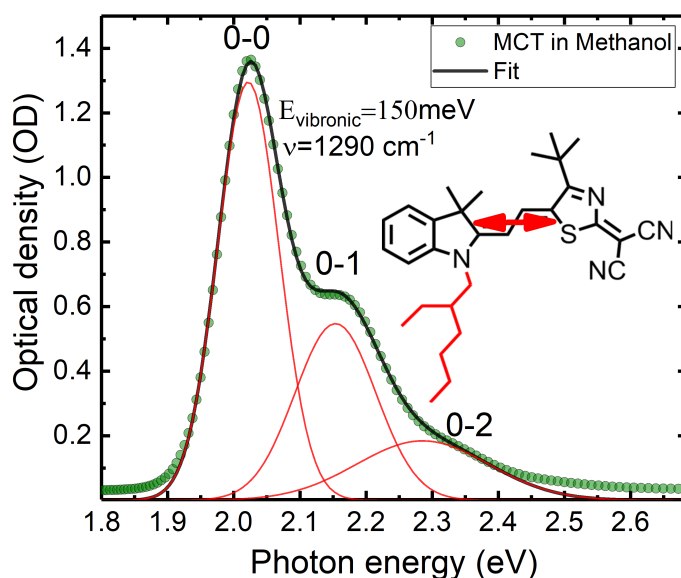


Figure 5.2: Absorption spectra of MCT merocyanine molecule dissolved in methanol. The spectrum was fitted with three Gaussian functions. The extracted vibronic energy (difference between vibronic levels) of 150 meV was extracted from the fit.

5.1.2 Photoluminescence properties of merocyanine dyes

Merocyanine dyes have a luminescence that is strongly dependent on the surrounding properties. In fact merocyanine type dyes are widely used in biology to study membrane potentials because it was shown that the fluorescence lifetime of well-studied M540 type merocyanine is affected by the surrounding polarization field[17]. In our study we have measured photoluminescence spectrum of merocyanine molecules dissolved in methanol solution. For this experiment the molar concentration was

kept at 10^{-5} mol/l to avoid molecular segregation and self-re-absorption of the fluorescence. For an excitation the lamp source with a monochromator fixed at 2.2 eV photon energy was used. For detection, a monochromator in combination with a photo-multiplier tube was used. The Detected light was filtered with 2 eV long pass filter to ensure a complete elimination of the excitation beam scattering to the detector. It was shown in the absorption spectrum of MCT and MH molecules dissolved in different solvents (figure 5.4) that MCT and MH merocyanine have similar optical properties. In fact the optical transitions in these molecules arise from the intramolecular charge transfer state which is hardly affected by the additional alkyl chain. Therefore, photoluminescence properties of both molecules also should be somewhat similar, because of similar electronic structure. The fluorescence spectrum of MCT molecule together with its optical density spectrum (in methanol solution) is shown in the figure 5.3. From this data a stokes shift of 75 meV was derived. To clarify if emission of the excited MCT molecule comes from the S_1 level, excitation spectrum with detection fixed at 1.94 eV was measured. A good overlap between absorption and excitation spectra indicate that fluorescence is originating from the same merocyanine molecule.

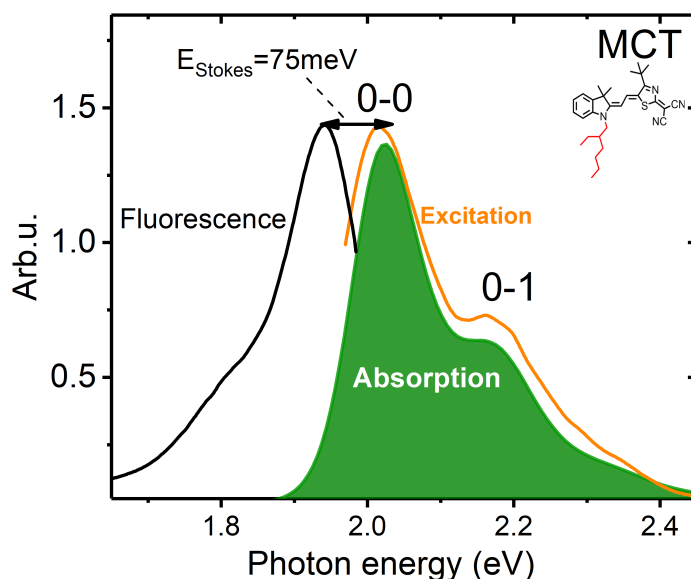


Figure 5.3: Fluorescence, absorption and excitation spectra of MCT molecule, dissolved in methanol solution with 10^{-5} mol/l molar concentration. For fluorescence measurements, 2.2 eV excitation was used and for excitation measurements, the detector was fixed at 1.94 eV. A strong overlap between absorption and excitation spectrum indicates that the S_1 emission was detected and no intermediate emissive state is present.

5.1.3 Solvatochromic behavior of merocyanine dyes

One of the important aspects of merocyanine type molecules, is their strong solvatochromic character. Optical properties of merocyanine type molecules, as well as other D- π -A type chromophores depend on the properties of the surroundings. The oscillator strength of these molecules show a strong dependence to the distance between polymethine chain separated donor/acceptor moieties. This in turn is sensitive to the surrounding properties such as dielectric constant, making merocyanine molecules very sensitive to different solvents.

Solvatochromism - a brief description of Onsager reaction field model

The first pioneering work on solvatochromism from the electrostatic perspective was done by Onsager [18]. The key idea is that electrons in solvent would rapidly readjust to a new charge distribution after electronic excitation (about 10^{-15} s), whereas nuclei need more time to equilibrate to the new electronic environment (about 10^{-12} to 10^{-10} s) which follows the Franck-Condon principle. The nuclear relaxation degree of freedom is reflected in the static dielectric function and far-infrared spectrum whereas the electronic response - in the optical refractive index. These contributions are very sensitive to the dielectric properties of the surrounding medium.

In case of polar molecules, solvent - solute interactions would stabilize the polar solute. According to the reaction field model, introduced by Onsager[18]. The basic assumption of this model is that the molecule is placed in a spherical cavity inside the solvent. The spherical cavity can be described as a homogeneous, polarizable medium with a constant dielectric constant. The ground state dipole moment of the molecule induces a so-called reaction field (\vec{E}_g), which directly affects and orients the solvent to stabilize the polar solute.

$$\vec{E}_g = \frac{2(D-1)}{2D+1} \frac{\vec{\mu}_g + \alpha\vec{\mu}_g}{a^3} \quad (5.1)$$

Here D is the dielectric constant of the medium, a is the radius of the cavity and $\vec{\mu}_g$ is the ground state dipole moment of the molecule. Because of the solute - solvent interaction, the ground state energy of the molecule in the solvent gets stabilized by the energy $U_g = |\vec{\mu}_g|^2 \beta L(D)$. In this equation $\beta = 2/a^3$ and $L_0(D) = \frac{D-1}{2D+1}$. After the electronic excitation, the initial reaction field has an equilibrium electronic polarization for the excited state together with the orientational polarization of the solvent, equilibrated to the ground state dipole. The initial stabilization of the excited state is $U_e = -\vec{\mu}_e(\vec{E}_{g,nuc} + \vec{E}_{e,elec})$, which shows that it is directly proportional to

the excited state dipole moment $\vec{\mu}_e$. The shift of the absorption peak a molecule in a solvent therefore is given by: $(U_e - U_g)/hc$.

In this study merocyanine molecules were dissolved in solvents with different polarities and optical properties were measured using the absorption spectroscopy. Results of this study are shown in the figure 5.4.

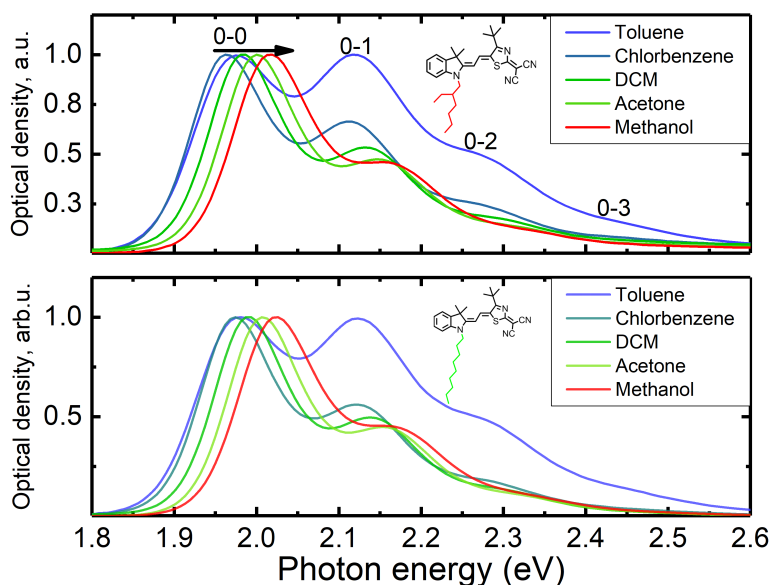


Figure 5.4: Optical density of MCT merocyanine (a) and MH (b), measured when dissolved in solvents with different polarities. The increase of the 0-1 vibronic peak in toluene can be seen and was assigned to a different molecular reorientation.

A strong correlation between solvatochromic shift of the 0-0 vibronic energy and polarity index ET_{30} of different solvents is shown in the figure 5.5. The ET_{30} is an empirical parameter based on the solvatochromism of a pyridinium phenolate betaine dye. The hypsochromic shift as a function of ET_{30} was observed for both MCT and MH molecules, which is a typical behavior for merocyanine type of chromophores. The shift solvatochromic shift in organic molecules is typically caused by changed interaction between solvent and solute. The negative or hypsochromic solvatochromic effect appears when increasing solvent polarity, the ground state of the molecule gets more stabilized than the first excited state in the Franck-Condon approximation.

The negative solvatochromism effect can be caused by a large ground state stabilization energy induced by strong solvent and solute interactions. It was shown that merocyanine molecules have a large ground state dipole moment $\vec{\mu}_g$ and the ground state dipole moment and ground state stabilization energy are directly related $U_g = |\vec{\mu}_g|^2 \beta L(D)$. This suggests that the negative solvatochromism is a di-

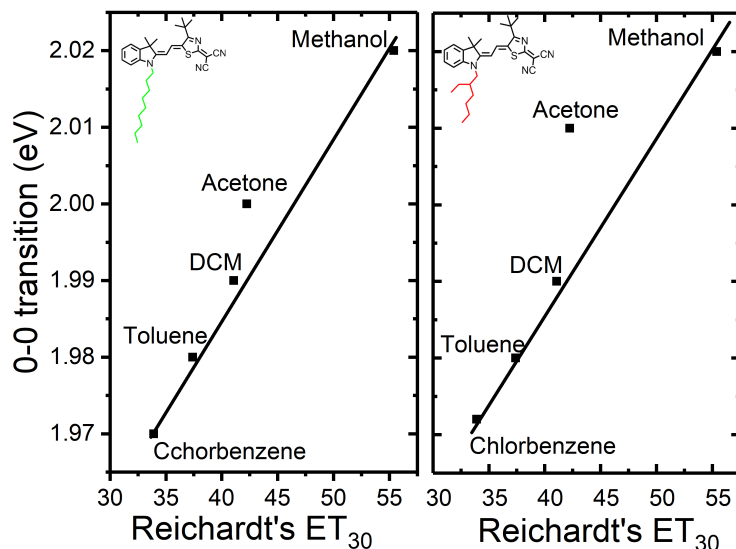


Figure 5.5: The spectral position of the 0-0 vibronic transition follows the Reichardt's ET_{30} empirical parameter of different solvents.

rect result of ICT (intermolecular charge transfer state) related ground state dipole moment in merocyanine molecules.

5.1.4 H-aggregation

Molecules with a strong dipole moment tend to couple together and form different kinds of structures such as aggregates and supra-molecules[9, 19, 20]. It is also known that H-aggregates formed from merocyanine molecules can be centrosymmetric structures (with positive and negative ends pointing to opposite directions) [21] which could reduce the electrostatic dipole scattering in merocyanine solids.

Molecular aggregates with a strong intermolecular interaction are known to have a substantially different absorption and fluorescence spectra compared to the monomer spectra, while the electronic structure of individual molecules in the aggregate remains unchanged. The typical distance between molecules in the molecular aggregate is large enough, so that tunneling effects can be neglected, meaning that Coulomb interactions are the one playing a major role.

In fact, the nature of the interaction in aggregate is somewhat similar to virtual photons mediated, non-radiative near field coupling in plasmonic structures. The classification between the H and J aggregate was first introduced by Michael Kasha[22]. In this aggregate model, a Davydov approach was used: a simple Frenkel exciton model was applied to treat the geometry determined crystal problem to-

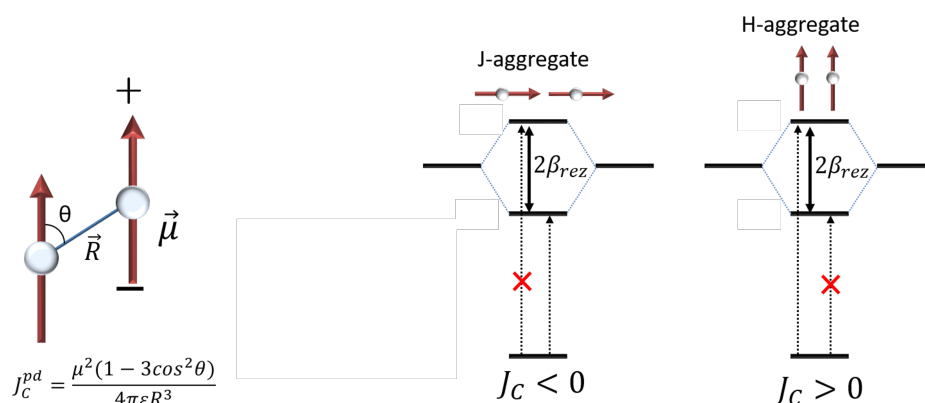


Figure 5.6: Theoretical model of the H and J aggregate formation in a simple dimer: a) representation of coulomb interaction between two dipoles of single molecules b) energy diagram of J and H aggregates. Here the intraction strength of the aggregate is depicted as 2β

gether with a purely Coulomb coupling between individual molecules[23]. Employing the exciton theory, it was shown that in certain aggregates, which know are known as H-aggregates, the Coulomb coupling is positive, leading to a band of singlet excitons in which the highest energy state consumes all the oscillator strength. This also suggests that according to Kasha's rule[24] the fluorescence comes only from lowest lying states, resulting in the fluorescence yield suppression in H type aggregates. On another hand, when the Coulomb interaction is negative, as in J type aggregates, the oscillator strength is maximized on the lowest exciton and no fluorescence suppression is expected.

To understand the exciton splitting in aggregates a simple two-point dipoles model with a Coulomb coupling between them:

$$J_C^{pd} = \frac{\vec{\mu}_1 \vec{\mu}_2 - 3(\vec{\mu}_1 \vec{R})(\vec{\mu}_2 \vec{R})}{4\pi\epsilon R^3} \quad (5.2)$$

In this formula the J_C^{pd} stand for the Coulomb coupling, $\vec{\mu}_1$ and $\vec{\mu}_2$ are *transition dipoles* of the optical transition in question namely the $S_0 - S_1$ transition. The \vec{R} is a displacement vectors which connects molecular mass center of two molecules and ϵ is the dielectric constant. Depending on the relative angle θ between two transition dipole moments $\vec{\mu}_1$ and $\vec{\mu}_2$ (in the figure 5.6) two aggregation species can be identified. One of the orientations which is known as the J-aggregate is when dipoles hold a "head-to-tail" orientation. In this case the angle θ is less then so called "magic" angle of 54.7 degrees, when the J_C^{pd} is zero. In the "head-to-tail" orientation case the Coulomb interaction is negative ($J_C^{pd} < 0$). When dipoles orient to "Side-by-Side" orientation, the Coulomb interaction becomes positive ($J_C^{pd} > 0$).

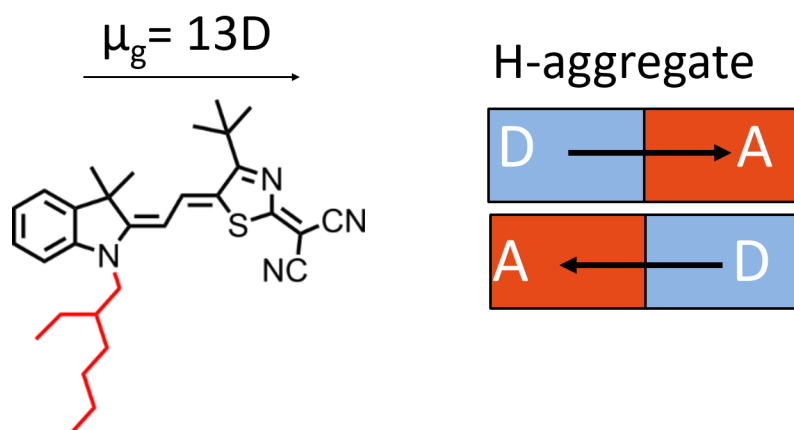


Figure 5.7: Structure of the investigated merocyanine molecule. The dipole moment of investigated molecules is driving the side to side, anti-symmetric dimer formation also known as H-aggregate.

The sign of the Coulomb interaction plays an important role in the photo physical properties of aggregated chromophores[22, 25, 26]. In case of two coupled monomers, the Coulomb interaction leads to a formation of two delocalized excitonic states, splitted by $2|J_C|$. The excited state splits to the in and out of phase linear combinations of two locally excited molecular states. The in-phase state is shifted by J_C as compared to the monomer and the out of phase component is characterized by the $-J_C$ shift. In a situation of negative Coulomb interaction $J_C < 0$ (J-aggregate) the oscillator strength is shifted to the low energy state and when the $J_C > 0$ the absorption strength of the higher energy state is enhanced. This behavior of H and J aggregates gives an opportunity to predict the molecular dimer packing by analyzing the absorption spectrum of a system made of aligned monomers.

5.2 H-aggregation of merocyanines in different solvents

As it was mentioned before, merocyanines are highly polar molecules and dipole-dipole interactions can lead to complex molecular aggregate formation[27]. These interactions are Van Der Waals - Keesom type interaction between two permanent dipoles which are of electrostatic nature which are in fact sensitive to dielectric properties of the surrounding medium. The angle averaged Keesom force interaction is given by the equation:

$$V = \frac{-m_1^2 m_2^2}{24\pi^2 \epsilon_0^2 \epsilon_r^2 k_B T r^6} \quad (5.3)$$

where m_1 m_2 are a dipole moments of two molecules, ϵ_0 permittivity of free space, ϵ_r dielectric constant of the surrounding medium, r distance between two molecules. A good way to control this can be achieved by using solvents with different dielectric constants ϵ_r . In this study we have chosen water $\epsilon_r = 80$ and acetone $\epsilon_r = 20,7$ [28]. Our investigated chromophores were unsolvable in water but were easily dissolved in the acetone solution. By adding a poor solvent to the solution, a situation can be created where intermolecular interactions overcome solvent repulsion and molecular aggregates can be formed. Results of solvent mixing are shown in the figure 5.8. As it was expected, by adding a non-dissolving water solvent to acetone, a sudden optical properties change was observed. The abrupt transition from monomer to aggregate is observed at 1:4 acetone to water ratio. At this point a strong dipole-dipole interaction overcomes electrostatic repulsion of a double solvent layer between two chromophores.

The appearance of a hypsochromically shifted band is directly related to the H-type aggregate formation of two parallel aligned molecules[25]. The parallel alignment of molecules is driven by the dipole: dipole interaction of polar molecules such as merocyanines. Using the spectral position of the H-aggregate peak, the resonance interaction strength 2β of the aggregate can be estimated. The peak positions from which the resonance energy was estimated, is shown with horizontal lines in the figure 5.8. For both investigated chromophores the resonant interaction energy of excited states of individual monomers is 160 meV. This interaction energy falls on the higher side of the expected value. The typical coupling strength in cyanine based H-aggregates can vary from 200 meV to 500 meV depending on molecular packing and dipole moment[9, 29, 30]. The large splitting energy can be caused by a large ground state dipole moment of investigated chromophores.

Another important feature in the absorption spectrum of merocyanine with large quantity of water is the appearance of the red-shifted spectral feature at 1.9 eV. This new state is followed by a H-aggregate formation and could be related to the relative orientation of aggregates. Similar differences also were reported for other merocyanines dyes in H-aggregate supramolecular and were assigned to different orientations in the molecular crystal[31].

In the figure 5.8 is also reported the computed (vide infra the Computational Methods section) electronic absorption spectrum of MH single crystal (vide infra for the X-Ray Structure Analysis). The electronic absorption spectrum of MH single crystal shows two main absorption bands, at 1.8 eV and 2.45 eV, featuring an energy splitting of 0.65 eV. The two bands are polarized along the b and c axis of the molecular crystal, showing a parallel alignment between the dipole moments. The

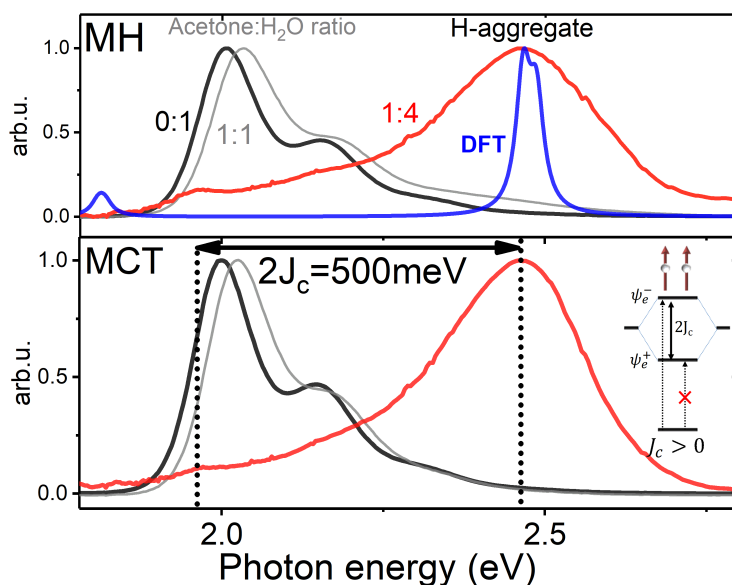


Figure 5.8: a) Control of the H-aggregation can be achieved by addition of poor solvent. The monomer spectrum is observed in the case of a "good" solvent - acetone (CH_3)₂CO. Addition of a "bad" solvent H₂O leads to increased intermolecular interaction leading to a sudden nucleation and aggregate formation.

spectral shape and the band splitting well match the experimental spectrum of MH in acetone-water solvent mixture. The strong similarity between the two spectra, as derived from the calculation on single crystal structure and the experimental solvent-induced aggregates, might suggest the formation of crystalline domains in solution. In particular, the presence of a low energy (1.8 eV) and a high energy (2.5 eV) band in the UV-VIS absorption spectra of films and blends suggests the presence of merocyanine aggregates.

5.3 H-aggregation in merocyanine films

For organic optoelectronics applications, the intermolecular interaction in solid molecular films is of biggest interest. To investigate the solid phase of molecules, MCT and MH molecules were spin coated on a quartz substrate leading to a molecular solid film formation. The linear absorption spectrum of such films are shown in the figure 5.9. The absorption spectrum of both films also showed the hypsochromically shifted spectral component which was previously assigned as H-aggregate transition. The spectral position of the H-aggregate peak both in liquid and in solid phases are at 2.5 eV, meaning that intermolecular interactions and packing behavior does not change going from one phase to another. It is also worth mentioning that broadening effects in solid films are affecting the spectral shape the H-aggregate

peak in solid state films. That is caused mainly by amorphous nature of the film. Comparison between MCT and MH merocyanine films is shown in the figure 5.9. Spectra of both films was adjusted by removing the pure H-aggregate component. This component was deducted from the solvent absorption data in 1:4 acetone-water solution. The weight of H-aggregate spectra was adjusted to 1/3 to avoid negative components in the resulting spectra. Removal of this spectral part lets to compare more intrinsic spectral properties of film spectra such as ratios between 0 – 0 and 0 – 1 vibronic components and broadening effects. Differences between modified MCT and MH spectra are shown below the figure 5.9 b. It indicates some small differences at the red and blue sides of the spectrum. The difference in low energy spectra part could correspond to below the gap states such as defect or CT states. Differences in the higher energy spectral part corresponds to small deviations in aggregation or additional broadening effects. This discrepancy in Aggregate formation is a direct result of different molecular packing, caused by different alkyl chains in studied merocyanine molecules.

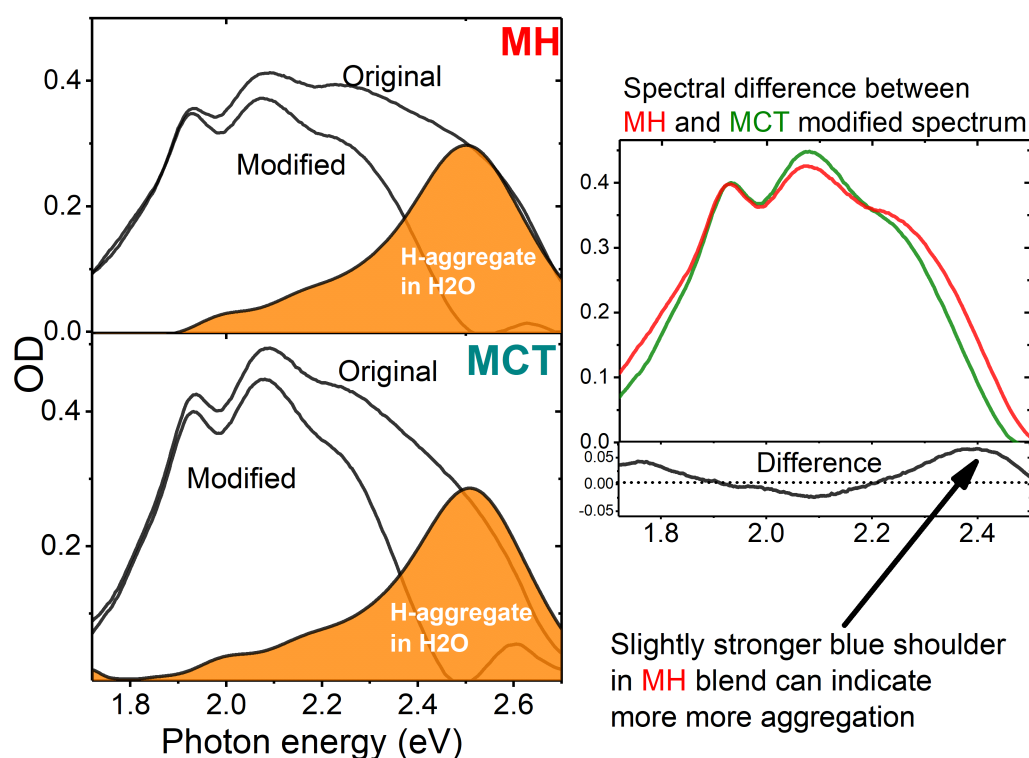


Figure 5.9: Absorption spectra of MCT and MH films together with their H-aggregate spectrum, measured in the acetone-water solution. The modified spectrum was calculated by subtracting the pure H-aggregate spectrum from the film.

5.3.1 Use of PC₆₁BM molecules to tailor H-aggregation in merocyanine films

The absorption spectra of PC₆₁BM:merocyanine films with different molar ratio between two molecules is shown in the figure 5.10a and the strength of the H-aggregate absorption component is plotted in the Figure 5.10b. A strong negative correlation between PC₆₁BM content in the blend film and H-aggregate strength was observed: blends with high PC₆₁BM concentration have less aggregation and vice-versa. This reduction in aggregation is evidence of a strong merocyanine: PC₆₁BM intermixing, where large PC₆₁BM molecules hinder the closely packed structure of H-aggregate formation by molecular hindrance. The sketch of the proposed model is shown in the figure 5.10c. This shows how much of impact the intermolecular interactions could have to micro crystallinity and morphology of merocyanine molecules.

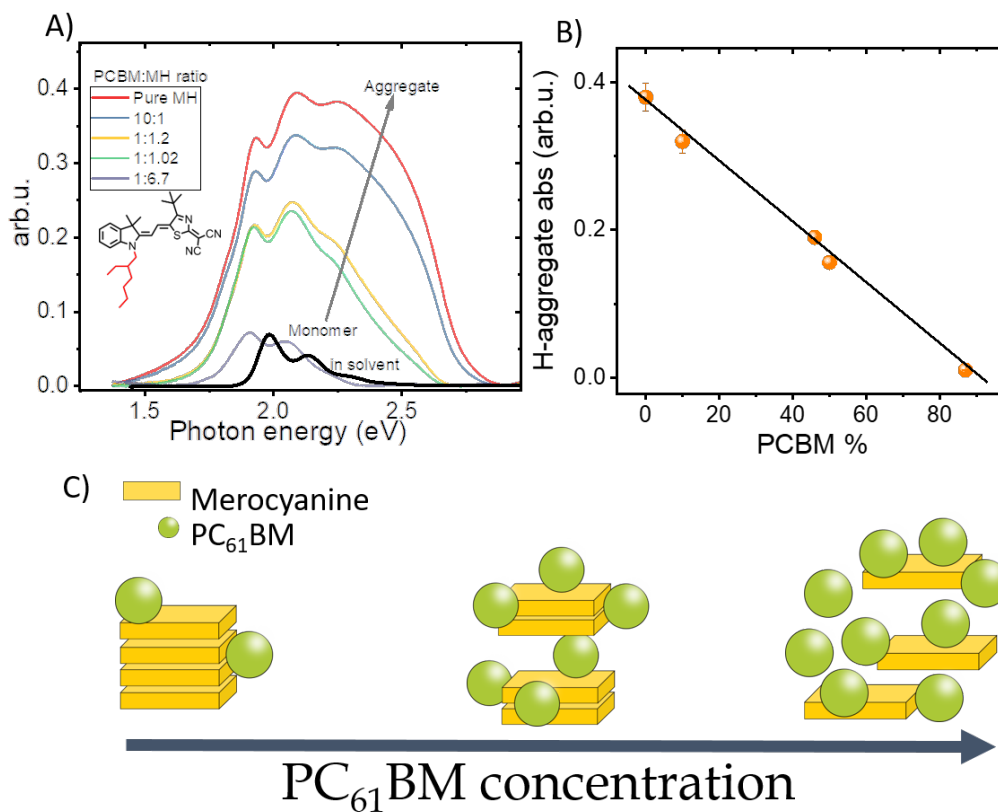


Figure 5.10: a) Absorption spectrum of MH:PC₆₁BM blend films with varying PC₆₁BM:MH molar ratio; b) the intensity of the H aggregation peak (taken at 2.3 eV) as a function of PC₆₁BM content; c) the sketch of merocyanine molecular packing at different PC₆₁BM concentrations.

The absorption spectrum shape of the film with PC₆₁BM:merocyanine ratio of 10 : 1 closely resembles the shape of the monomer spectrum with a slight red shift

in energy. We attribute this red-shift in the absorption energy to the change in the dielectric environment of the merocyanine molecules. From Onsager theory [18] it is known that local change in the dielectric constant changes the electrostatic interaction between the charge distribution $\rho(r)$ of a molecule and the local electric field E^{loc} of surrounding molecules as it was shown in the equation 5.1. This shift affects the energy of the ground and excited state of the molecules, leading to different absorption energy. It was shown by Madigan *et al.* [32] that the theory of solvation also could successfully be applied to amorphous organic films. The dielectric constant of PC₆₁BM molecules is ($\epsilon_r = 3.9$) which is larger than a typical organic cyanine type film ($\epsilon_r = 2$), and similar red-shift in absorption energy was absorbed also in other fullerene blends[33, 34].

5.4 Conclusions

Molecular packing behavior of two different merocyanine molecules was investigated. A strong H-aggregate type spectral shift with a coupling energy of 250 meV in the absorption spectrum was observed. By analyzing the H-aggregation behavior in films and liquid, it was found that in bulk hetero junction types of films, aggregation gets largely suppressed. This process was investigated in more details with changing the concentration of PC₆₁BM molecules in investigated films. The main mechanism behind such strong aggregation suppression is the molecular hindrance effect, caused by alkyl chains of merocyanine molecules.

5.4.1 Collaborations

The study, presented in this chapter was done with a collaboration with Dirk Hertel (preparation of merocyanine samples) and Daniele Fazzi (theoretical DFT calculations of H-aggregate formation).

References

1. Lei, T., Wang, J. Y. & Pei, J. Roles of flexible chains in organic semiconducting materials. *Chem. Mater.* **26**, 594–603 (2014).
2. Mei, J. & Bao, Z. Side chain engineering in solution-processable conjugated polymers. *Chem. Mater.* **26**, 604–615 (2014).
3. Zhang, Z. G. & Li, Y. Side-chain engineering of high-efficiency conjugated polymer photovoltaic materials. *Sci. China Chem.* **58**, 192–209 (2015).

4. Min, J., Luponosov, Y. N., Gerl, A., Polinskaya, M. S., Peregudova, S. M., Dmitryakov, P. V., Bakirov, A. V., Shcherbina, M. A., Chvalun, S. N., Grigorian, S., Kaush-Busies, N., Ponomarenko, S. A., Ameri, T. & Brabec, C. J. Alkyl Chain Engineering of Solution-Processable Star-Shaped Molecules for High-Performance Organic Solar Cells. *Adv. Energy Mater.* **4**, 1301234 (2014).
5. Qu, S., Qin, C., Islam, A., Wu, Y., Zhu, W., Hua, J., Tian, H. & Han, L. A novel D–A– π –A organic sensitizer containing a diketopyrrolopyrrole unit with a branched alkyl chain for highly efficient and stable dye-sensitized solar cells. *Chem. Commun.* **48**, 6972 (2012).
6. Tumbleston, J. R., Collins, B. A., Yang, L., Stuart, A. C., Gann, E., Ma, W., You, W. & Ade, H. The influence of molecular orientation on organic bulk heterojunction solar cells. *Nat. Photonics* **8**, 385–391 (2014).
7. Zhou, K., Zhang, R., Liu, J., Li, M., Yu, X., Xing, R. & Han, Y. Donor/Acceptor Molecular Orientation-Dependent Photovoltaic Performance in All-Polymer Solar Cells. *ACS Appl. Mater. Interfaces* **7**, 25352–25361 (2015).
8. Sieber, F. MEROCYANINE 540. *Photochem. Photobiol.* **46**, 1035–1042 (1987).
9. Rösch, U., Yao, S., Wortmann, R. & Würthner, F. Fluorescent H-Aggregates of Merocyanine Dyes. *Angew. Chemie Int. Ed.* **45**, 7026–7030 (2006).
10. Petrenko, A. & Stein, M. Molecular Reorganization Energy as a Key Determinant of J-Band Formation in J-Aggregates of Polymethine Dyes. *J. Phys. Chem. A* **119**, 6773–6780 (2015).
11. Würthner, F., Yao, S., Debaerdemaeker, T. & Wortmann, R. Dimerization of Merocyanine Dyes. Structural and Energetic Characterization of Dipolar Dye Aggregates and Implications for Nonlinear Optical Materials. *J. Am. Chem. Soc.* **124**, 9431–9447 (2002).
12. Lohr, A., Grüne, M. & Würthner, F. Self-Assembly of Bis(merocyanine) Tweezers into Discrete Bimolecular π -Stacks. *Chem. - A Eur. J.* **15**, 3691–3705 (2009).
13. Lissau, H., Frisenda, R., Olsen, S. T., Jevric, M., Parker, C. R., Kadziola, A., Hansen, T., van der Zant, H. S. J., Brøndsted Nielsen, M. & Mikkelsen, K. V. Tracking molecular resonance forms of donor–acceptor push–pull molecules by single-molecule conductance experiments. *Nat. Commun.* **6**, 10233 (2015).

14. Mustroph, H., Reiner, K., Mistol, J., Ernst, S., Keil, D. & Hennig, L. Relationship between the molecular structure of cyanine dyes and the vibrational fine structure of their electronic absorption spectra. *ChemPhysChem* **10**, 835–840 (2009).
15. Pouradier, J. Remarque sur le spectre d'absorption des cyanines en solution. *J. Chim. Phys.* **61**, 1107–1114 (1964).
16. Yamada, Y., Nakamura, T., Endo, M., Wakamiya, A. & Kanemitsu, Y. Photocarrier recombination dynamics in perovskite $\text{CH}_3\text{NH}_3\text{PbI}_3$ for solar cell applications. *J. Am. Chem. Soc.* **136**, 11610–3 (2014).
17. Dragsten, P. R. & Webb, W. W. Mechanism of the membrane potential sensitivity of the fluorescent membrane probe merocyanine 540. *Biochemistry* **17**, 5228–5240 (1978).
18. Onsager, L. Electric Moments of Molecules in Liquids. *J. Am. Chem. Soc.* **58**, 1486–1493. arXiv: ja01299a050 (1936).
19. Yao, S., Beginn, U., Gress, T., Lysetska, M. & Würthner, F. Supramolecular Polymerization and Gel Formation of Bis(Merocyanine) Dyes Driven by Dipolar Aggregation. *J. Am. Chem. Soc.* **126**, 8336–8348 (2004).
20. Khairutdinov, R. F. & Serpone, N. Photophysics of Cyanine Dyes: Subnanosecond Relaxation Dynamics in Monomers, Dimers, and H- and J-Aggregates in Solution. *J. Phys. Chem. B* **101**, 2602–2610 (1997).
21. Würthner, F. & Meerholz, K. Systems Chemistry Approach in Organic Photovoltaics. *Chem. - A Eur. J.* **16**, 9366–9373 (2010).
22. Kasha, M. Energy Transfer Mechanisms and the Molecular Exciton Model for Molecular Aggregates. *Radiat. Res.* **20**, 55 (1963).
23. Davydov, A. S. The theory of molecular excitons. *Sov. Phys. Uspekhi* **7**, 145–178 (1962).
24. Kasha, M. Characterization of electronic transitions in complex molecules. *Discuss. Faraday Soc.* **9**, 14 (1950).
25. Kasha, M. Rawls, A. M. The exciton model in molecular spectroscopy. *Pure Appl. Chem.* **11**, 371–392 (1965).
26. Hochstrasser, R. M. & Kasha, M. Application of the exciton model to monomolecular lamellar systems. *Photochem. Photobiol.* **3**, 317–331 (1964).

27. Würthner, F. Dipole-Dipole Interaction Driven Self-Assembly of Merocyanine Dyes: From Dimers to Nanoscale Objects and Supramolecular Materials. *Acc. Chem. Res.* **49**, 868–876 (2016).
28. Maryott, A. A. & Smith, E. R. *Table of Dielectric Constants of Pure Liquids* 1–44 (1951).
29. Nüesch, F. & Grätzel, M. H-aggregation and correlated absorption and emission of a merocyanine dye in solution, at the surface and in the solid state. A link between crystal structure and photophysical properties. *Chem. Phys.* **193**, 1–17 (1995).
30. Ryu, N., Okazaki, Y., Pouget, E., Takafuji, M., Nagaoka, S., Ihara, H. & Oda, R. Fluorescence emission originated from the H-aggregated cyanine dye with chiral gemini surfactant assemblies having a narrow absorption band and a remarkably large Stokes shift. *Chem. Commun.* **53**, 8870–8873 (2017).
31. Liess, A., Lv, A., Arjona-Esteban, A., Bialas, D., Krause, A.-M. M., Stepanenko, V., Stolte, M. & Würthner, F. Exciton Coupling of Merocyanine Dyes from H- to J-type in the Solid State by Crystal Engineering. *Nano Lett.* **17**, 1719–1726 (2017).
32. Madigan, C. F. & Bulović, V. Solid State Solvation in Amorphous Organic Thin Films. *Phys. Rev. Lett.* **91**, 247403 (2003).
33. Loi, M. A., Toffanin, S., Muccini, M., Forster, M., Scherf, U. & Scharber, M. Charge transfer excitons in bulk heterojunctions of a polyfluorene copolymer and a fullerene derivative. *Adv. Funct. Mater.* **17**, 2111–2116 (2007).
34. Jahani, F., Torabi, S., Chiechi, R. C., Koster, L. J. A. & Hummelen, J. C. Fullerene derivatives with increased dielectric constants. *Chem. Commun.* **50**, 10645–10647 (2014).

Chapter 6

Charge transfer state formation in merocyanine:PC₆₁BM

The scope of this chapter is photophysical properties of a charge transfer (CT) state in merocyanine dimers. Here two different merocyanine dyes were studied, having different packing behavior, resulting in different molecular geometries in a mixture with a PC₆₁BM. It was shown that different merocyanine molecules have different packing behavior and interfacial CT state formation. To get more insight in to the dynamical properties of the observed interfacial CT state, transient absorption experiments on merocyanine:PC₆₁BM blends and pristine merocyanine films were performed. In the transient spectrum, a CT peak was observed both in the pristine and in blend films. This concludes that the observed CT state is an intermolecular CT state between different merocyanine molecules. The intensity of the CT peak for different merocyanines was different, confirming that merocyanines with different packing behavior can impact the oscillator strength of the CT state in the merocyanine dimer.¹

¹Parts of this chapter were published in K. Budzinauskas *et al.*, Impact of the interfacial molecular structure organization on the charge transfer state formation and exciton delocalization in merocyanine:PC₆₁BM Blends, *J. Phys. Chem. C*, **124**, 21978-21984 (2020).

The organic solar cell devices usually consist of two components: electron donor and electron acceptor molecules. Device performance measures such as an open-circuit voltage (V_{oc}) depend on the offset between the highest occupied molecular orbitals of a donor and acceptor. Parameters of donor and acceptor energy levels also impact the overall efficiency of a solar cell device. It is known that the alignment of molecular orbitals at donor:acceptor interface are strongly dependent on the molecular orientation [1]. It is also known that molecular orientation not only alters the energy level alignment but also charge decay mechanisms, such as the radiative recombination rate of the exciton at the donor:acceptor interface [2]. These strong geometrical dependencies arise from the nature of a π conjugated molecules, where the orientation of π orbitals could vastly impact photophysical properties of organic materials. Some authors have shown that when π orbitals of donor and acceptor molecules are parallel, it can reduce non-radiative recombination losses and lower the open circuit voltage V_{oc} [2].

In this chapter we were focusing on geometry driven charge transfer state formation and dynamics using different merocyanine dyes: MCT² and MH³ (shown in figure 6.1). The most noticeable difference between studied merocyanine dyes are alkyl chains (shown in color in the figure 6.1). Generally it is accepted that different sidechains should affect molecular packing properties due to molecular hindrance effects involved, especially in films when intermolecular distances are small[3]. In the previous chapter it was shown that packing behavior of MCT and MH molecules indeed are different. The optical absorption spectra of both merocyanines in diluted (concentration $< 10^{-5}$ mol/l) methanol are identical, showing that molecular orbitals, corresponding to HOMO \rightarrow LUMO level in optical transitions are not affected by different alkyl chains.

Most notable differences of MCT:PC₆₁BM and MH:PC₆₁BM absorption spectra occur in the H-aggregate related spectral region (2.2 – 2.5 eV)[4] as shown in the figure 6.2. It can reasonably be assumed that this effect is indeed caused by different alkyl chains of merocyanine dye, which are responsible for molecular packing. In case of MH merocyanine the H-aggregate formation process is only slightly altered by the incorporation of PC₆₁BM molecules, whereas MCT shows drastic reduction of H-aggregation in MCT:PC₆₁BM film. The more detailed study of H-aggregation in PC₆₁BM and merocyanine blends was done in the chapter 5 of this thesis.

²2-((Z)-4-tert-butyl-5-((E)-2-(3,3-dimethyl-1-(2-ethylhexyl)indolin-2-ylidene)ethylidene)thiazol-2(5H)-ylidene)malononitrile

³2-((Z)-4-tert-butyl-5-((E)-2-(3,3-dimethyl-1-nonylindolin-2-ylidene) ethylidene) thiazol-2(5H)-ylidene) malononitrile

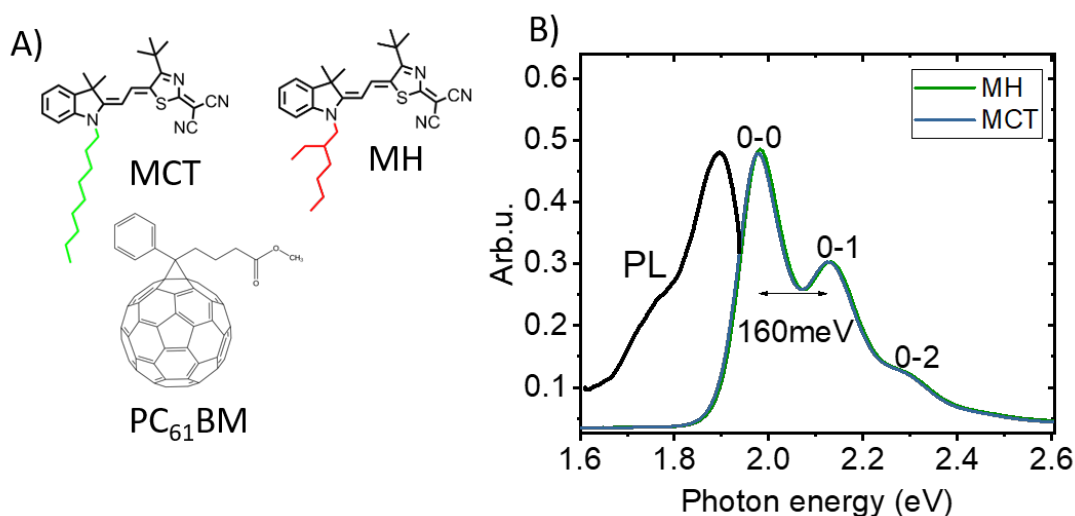


Figure 6.1: a) Structure of studied molecules; b) absorption and photoluminescence spectra of MCT and MH merocyanines, dissolved in methanol solvent.

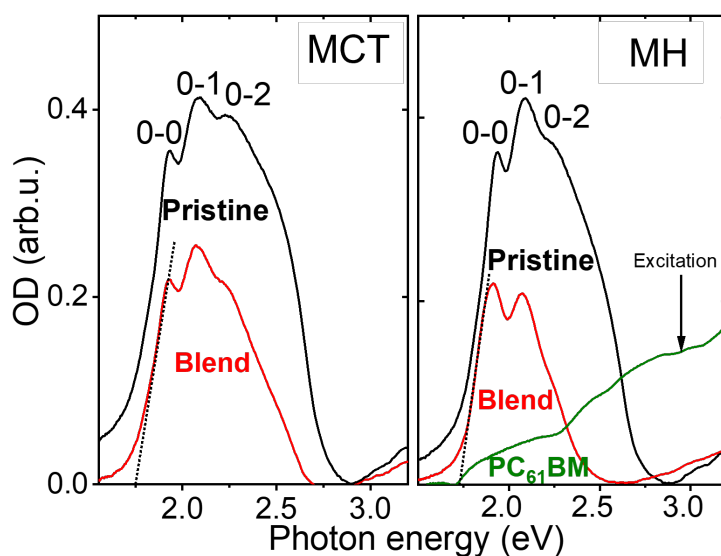


Figure 6.2: Absorption spectrum of different merocyanine films deposited on a quartz substrate together with absorption spectrum of pristine PC₆₁BM film. Dotted line in the absorption spectrum were used to deduce the optical gap of merocyanine films. In the high photon energy range (3eV and more), the S_0 - S_2 type of transition in merocyanines can occur.

6.1 Photophysical properties of PC₆₁BM

In order to fully understand the photochemistry of merocyanine and PC₆₁BM ([6,6]-Phenyl-C₆₁-butyric acid methyl ester) blend, it is crucial to know the basic photophysical properties of individual components. First, PC₆₁BM is a compound, derived from C₆₀ with an additional side chain and a carbon bond. The side chain increases

solubility of the molecule and allows the use of it for solution processed photovoltaics. The ground state of C_{60} fullerene has $^1A_{1g}$ character and the excited state is $^1T_{1u}$ (second singlet transition S_2) [5]. There is also lower excited state of $^1T_{1g}$ which has a symmetry forbidden [5] transition (named as S_1). There are also states which appear due to the coupling of nearby molecules. Existence of charge transfer (CT) exciton, where electron and hole are on adjacent C_{60} molecules is known for a long time. These excitons can be observed in the static absorption spectra at energies of 2.65 eV and 2.7 eV. The splitting of CT excitons can be explained by two different configurations of adjacent C_{60} molecules: a five ring:double bond or six ring: double bond interaction [6, 7].

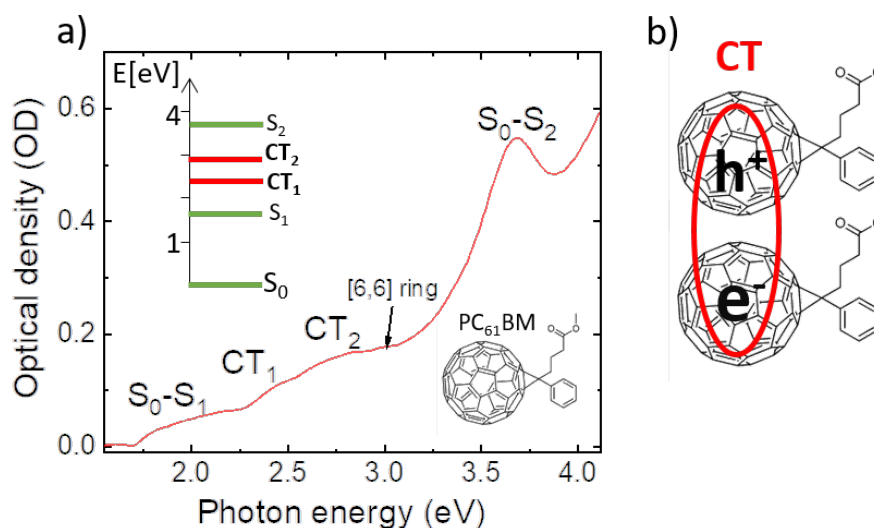


Figure 6.3: a) Absorption spectrum of a $PC_{61}BM$ film with marked specific optical transitions seen in the spectrum b) the illustration of a proposed charge transfer state between two $PC_{61}BM$ molecules.

The above mentioned electronic and optical properties are almost the same for $PC_{61}BM$. One of the most important difference is that it has perturbed conjugated π -system compared to C_{60} . The side double C bond connection to fullerene converts sp^2 hybridized carbons to sp^3 and causes the contraction of the π -electron system from 61 to 59 π electrons. The addition of a side chain breaks the I_h symmetry of a pure C_{60} . Also due to the symmetry breaking, the triplet quantum yield is lowered (in pure C_{60} it is close to a unity in benzene solvent) [8] and the symmetry forbidden $S_0 - S_1$ transition becomes more allowed [9].

In the static absorption spectrum there is also an additional peak at around 2.88 eV (figure 6.3) which is not present in the pristine C_{60} . This peak is typical for [6,6] - closed ring bridged methano-fullerenes [10] due to a local symmetry breaking.

The CT_1 (2.69 eV) and CT_2 (2.45 eV) state energies coincide with charge transfer excitons found in pure C_{60} molecules. That indicate that there are charge transfer exciton between $PC_{61}BM$ molecules and those transition can be accessed in the absorption spectrum in a visible spectral range. Similar spectral features were also reported by other authors with ellipsometry measurements, carried out on $PC_{61}BM$ films[11], meaning that the theory of photophysical properties of C_{60} can also be successfully applied to $PC_{61}BM$ molecules.

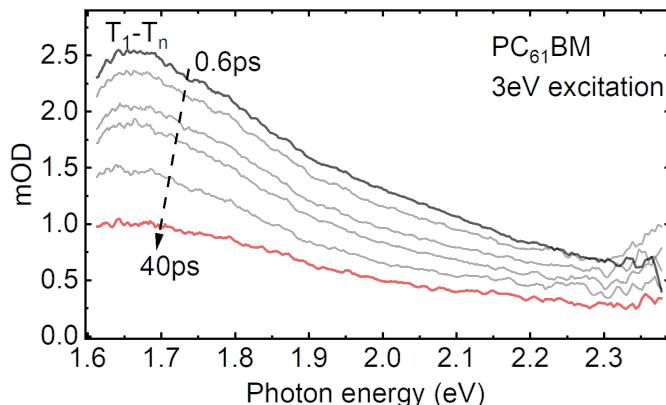


Figure 6.4: Transient absorption spectra of $PC_{61}BM$ films at different delay times excited with a 3 eV laser pulse.

To shed more light on photophysical properties of $PC_{61}BM$ molecules, transient absorption experiments on $PC_{61}BM$ films, deposited on quartz, were performed. The excitation energy of 3 eV was implemented, generating carriers just above the $S_0 - S_1$ excitation. This excitation energy was also used in bulk hetero-junction analysis, discussed in further sections. The transient absorption spectra at different delays (0.6 ps to 40 ps) is shown in the figure 6.4. After the photoexcitation, carriers rapidly decay to the triplet state (below the S_1 state) and a strong induced absorption at 1.65 eV corresponding to the $T_1 - T_n$ triplet-triplet transition is expected [12]. This transition was also observed in our time resolved absorption spectra and is in good agreement with literature.[11] At early delay times in the blue side of the photoinduced spectra, a weak spectral feature at 2.3 – 2.4 eV was also observed. This feature could be related to the population of the CT_1 state, also observed in the absorption spectrum of $PC_{61}BM$ at 2.4 – 2.5 eV in the figure 6.3. However, the observed feature is on the limit of the measurable spectral range and near the dispersion correction delay limit of the system. We would argue that more experiments would be necessary to confirm or deny this claim.

6.2 Charge transfer state formation in merocyanine films

To further investigate the interplay between molecular ordering of merocyanine molecules and their influence on photo-physical properties, time resolved studies, using transient absorption experiment was implemented. Transient absorption (TA) experiments were performed using Yb:KGW based laser system Pharos (Light Conversion) with 150 kHz repetition rate and 40 fs pulse duration with internal NOPA 800 nm and 1450 nm outputs. The 3 eV(400 nm) excitation pulse was generated via second harmonic generation by focusing 800 nm pulse to the beta barium borate (BBO) crystal. White light continuum probe was generated by focusing 1450 nm beam into the 4 mm thick Sapphire crystal. The overall experiment resolution is 80 fs and it deviates from the original 40 fs laser output mainly because of additional dispersion, caused by glass optics.

The excitation photon energy through out all time resolved studies was set to 3 eV, and its relative energetic position relative to the absorption spectrum of both PC₆₁BM and merocyanine molecules is shown in the figure 6.2. The optical density of pure PC₆₁BM molecules at 3 eV is 0.18 and both studied merocyanine molecules at this photon energy absorb very weak, with optical density of pristine MCT and MH films at 0.05. Considering that the sample thickness of both films are similar, with a molar ratio between merocyanine and PC₆₁BM at 1:1.2, for one excited merocyanine molecule there are 4.32 excited PC₆₁BM, giving a spectral selectivity of 4:1. This implies a selective excitation of PC₆₁BM molecules and with a visible probe pulse, selective probing on merocyanine molecules. This kind of energetical alignment of photon energies allows to directly investigate the charge carrier and energy transfer from PC₆₁BM to merocyanine through an intermediate charge transfer state or with a direct energy transport (for example Förster energy transfer).

Results of the transient absorption(TA) measurement on merocyanine films and merocyanine:PC₆₁BM blends are shown in the figure 6.5b and 6.5c. The negative spectral components in the TA spectra of different samples at 1.92 eV, 2.05 eV are the ground state bleach (GSB) of 0 – 0 and 0 – 1 vibronic replicas of merocyanine molecules. The additional negative transient component at 1.8 eV was observed in both pristine and blend cases of both investigated merocyanines. This observation is contradictory to the expected charge transfer state formation between donor and acceptor molecules, since it is observed in pure merocyanine films. In the figure 6.5 a) the absorption spectrum of MCT merocyanine and MCT:PCBM blend is shown and with a weak spectral shoulders, appearing below the 0 – 0 transition, meaning

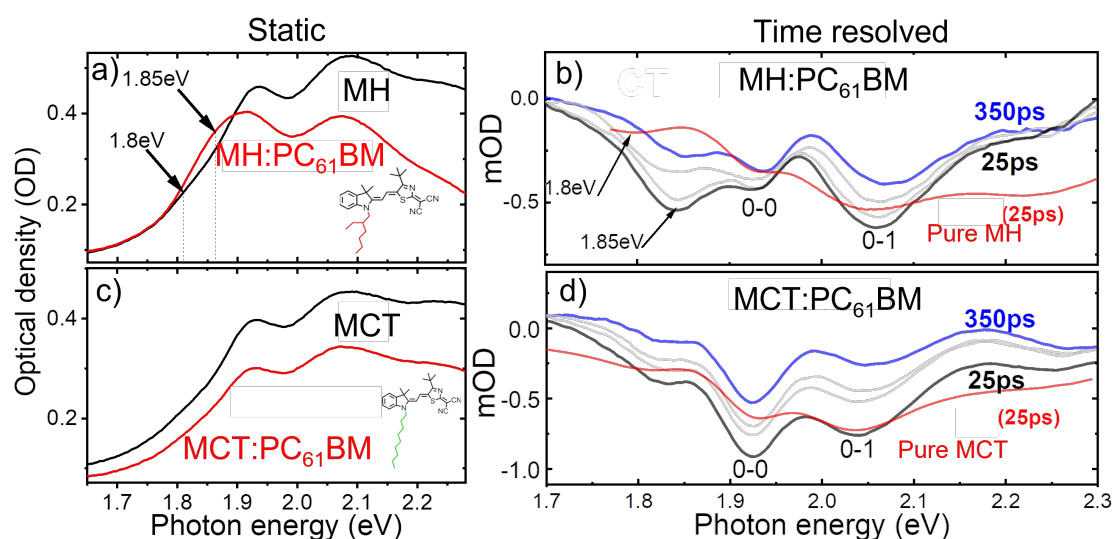


Figure 6.5: a) Absorption and b) transient absorption spectra of MCT and MCT:PC₆₁BM c) Absorption spectrum and d) time resolved absorption of MH and MH:PC₆₁BM MH:PC₆₁BM films. The 3 eV laser pulse was used for the excitation and white light continuum for probing the absorption change. Strong stimulated emission associated to the CT state was observed at 1.85 eV

that it is a possible below gap transition. By investigating the transient absorption spectra of the same merocyanine at 25 ps after the excitation in figure 6.5 a), similar spectral peaks with matching energetic positions occurred. As further explained in the modelling section, the 1.85 eV transition was assigned to a state featuring an inter-molecular CT character amongst merocyanines. In a less polar merocyanine similar CT excitons were previously suggested, however never modelled before [13].

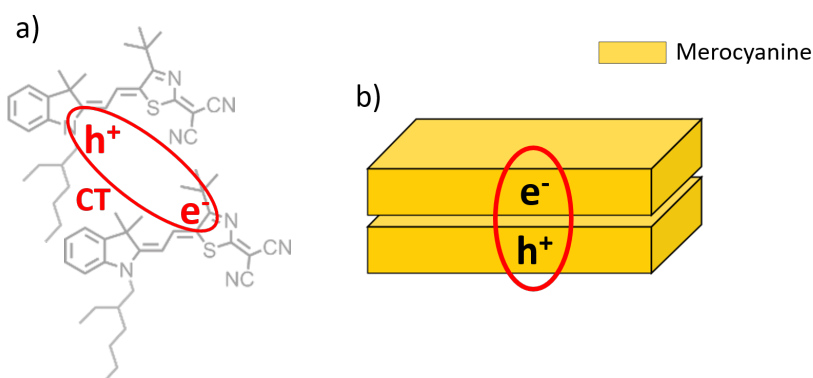


Figure 6.6: Intermolecular charge transfer state between two nearest merocyanine molecules with electrons on the propyl group and holes on the nitrile group. Merocyanine molecules tend to form H-aggregates, this packing model would imply that CT state also forms in merocyanine dimers with on top configuration.

In the transient spectrum of MCT:PC₆₁BM film, the amplitude of this component is comparably larger than the 0 – 0 ground state bleach component at 1.92 eV. For this to occur, a strong stimulated emission from the CT state due to a large population of excited carriers in this state must be present. For comparing relative amplitude of the CT state (1.85 eV) transition versus the ground state bleach signal (1.92 eV), the ratio between peak amplitudes of these transition was deduced from the transient spectrum. In MCT:PC₆₁BM film this ratio is 0.79 and in MH:PC₆₁BM film the ratio is 2.3, when in pristine films of investigated merocyanines ratios are almost identical: 0.46 and 0.45. This finding indicates either different oscillator strength of the CT transition or different population of the CT state in investigated Merocyanine:PC₆₁BM blends. Here we assume the oscillator strength to be the dominant factor. This assumption is based on differences in absorption spectra between MCT and MH blends in the figure 6.5a). This finding can be ascribed to the underlying CT state near the 0 – 0 transition with oscillator strength higher in MCT:PC₆₁BM film because in the MH:PC₆₁BM no additional shoulder below the 0 – 0 transition could be observed. These differences could occur due to a different molecular geometry in investigated films. This highlights the strong differences in photophysics of two merocyanine films when PC₆₁BM molecules are present. We stress that molecular packing in MCT and MH blends in fact is different, resulting in reduced H-aggregate formation in MCT:PC₆₁BM blend and smaller H-aggregate spectral weight in the 2.35 eV – 2.65 eV spectral region in the absorption spectrum.

In transient absorption experiment the excitation energy of 3 eV was used and as mentioned before - it allows the 4 : 1 selective excitation of PC₆₁BM molecules. The monitoring of merocyanine states with a visible probe beam should enable the observation of energy and charge transfer processes. In the time domain, a fingerprint of such a process would be a growing component in the ground state bleach or stimulated emission signal. In fact the growing component at the ground state bleach of merocyanine was observed in our transient absorption measurements with higher PC₆₁BM concentration but that could also be caused by other effect then energy or charge transfer from PC₆₁BM. After the photoexcitation of PC₆₁BM with 3 eV pulses, the a strong photo induced signal occurs in the 2 eV – 1.4 eV range (figure 6.4) and it overlaps with the ground state bleach signal of the merocyanine. The sum of two exponentially decaying signals with opposite amplitudes and similar decay times would yield a decay curve with what appears to be a growing part.

To reproduce this component a simple sum of the photoinduced signal of pure PC₆₁BM and ground state bleach signal of pure merocyanine was done. In this calculation, fitted decays of pure PC₆₁BM and merocyanine (MCT) were used. Results

of this are shown in the figure 6.7. The computed curve fits the growing signal and deviates from the signal only in early delay times, where carrier thermalization and exciton-exciton recombination could play a role. To elaborate further on whether there is a charge or energy transfer between PC₆₁BM and merocyanine, more experiments in different spectral range are necessary. For example visible excitation and ultraviolet probe, where electron transfer process from merocyanine to PC₆₁BM would be possible and detectable.

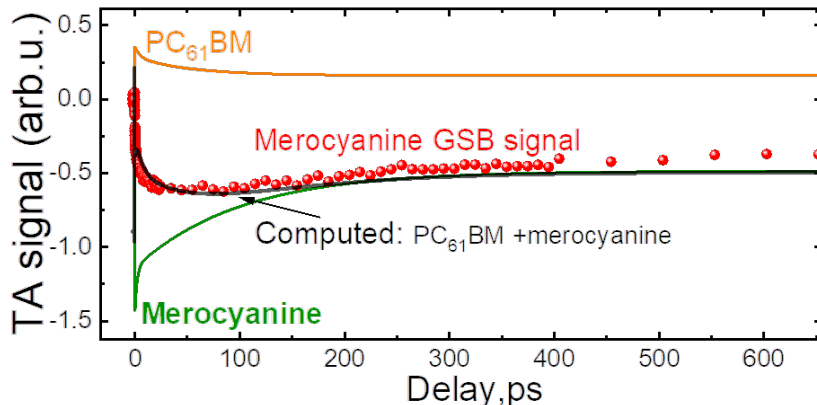


Figure 6.7: Growing component in the ground state bleach signal of MCT:PC₆₁BM film with extra PC₆₁BM (1:12 merocyanine:PC₆₁BM ratio) was observed. The growing component can be computed by adding the pure transient signal of excited PC₆₁BM and pure merocyanine film.

The spectral position of the CT state in mixed films (1.85 eV) is blue shifted as compared to the pristine films (1.85 eV). The blue shift in the CT state energy can be ascribed to the change in the CT state coupling energy, which is related to the effective dielectric constant of the material.[14] In this study we postulate that PC₆₁BM molecules are responsible for this effect caused by their relatively high dielectric constant ($\epsilon_r = 3.9$) compared to a typical merocyanine molecule ($\epsilon_r = 2.8$).[15–17]

To investigate the CT state recombination in more detail, a temperature dependent transient absorption study was performed. Temperature dependent temporal evolution of the CT state peak (probed at 1.85 eV) in MCT:PC₆₁BM films are shown in the figure 6.8. The decay data was fitted using a single exponential decay function, convolved with a Gaussian and a step function. At low temperature, a slowing down of the decay rate was observed indicating the activated decay mechanism. From the slope of Arrhenius graph (figure 6.8) the 40 meV activation barrier for the CT state recombination/dissociation was deduced. Intermolecular CT excitons on merocyanine dimers could dissociate to free charges or recombine back to the ground state. For the second process to occur the activation barrier is expected

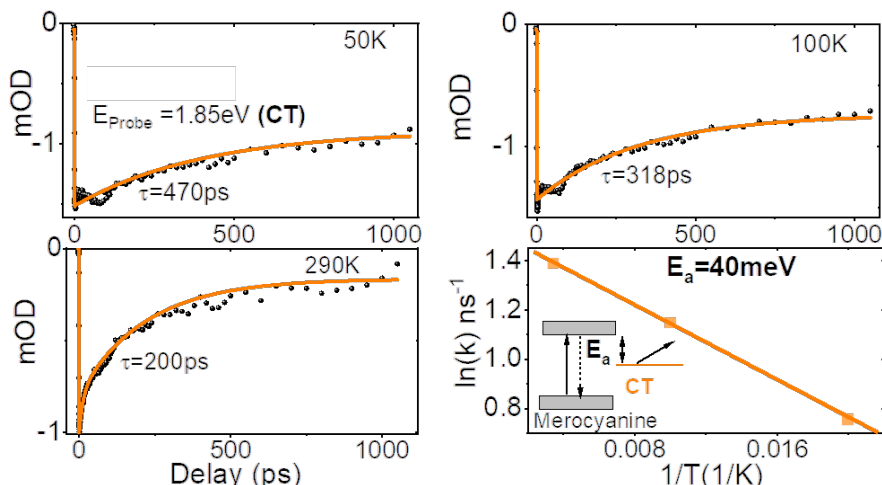


Figure 6.8: Temperature dependent decay dynamics of the CT state in MCT:PC₆₁BM blends. Arrhenius graph used to deduce the energy barrier of the charge transfer state recombination/dissociation process.

to be larger because CT should overcome the energy difference between the charge transfer exciton and 0 – 0 transition (0.5 eV). So a transition from the CT state to a triplet state or to another intermediate state is possible, but to shed more light on the exact temporal evolution of the CT exciton, additional experiments are needed.

6.2.1 Computational studies of merocyanine packing using DFT

To elaborate more on how molecular geometry at donor:acceptor surface could influence photophysical properties, theoretical studies were implemented. In the figure 6.9 are reported the TDDFT vertical transition energies (unscaled values) for the MCT cases, namely: the merocyanine dimer (2xMCT) and the clusters with both on-top (2xMCT:PC₆₁BMt) and on-side (2xMCT:PC₆₁BM_s) configurations. The merocyanine dimers are minimal structural models representing the pure merocyanine films, while the clusters with PC₆₁BM the BHJ interfaces. Both MCT and MH dimers show a bright excited state, here referred as S^* , at similar energies and oscillator strengths (2.82 eV, $f = 1.54$ for MCT and 2.79 eV, $f = 1.95$ for MH, see figure 6.9). S^* can be assigned to the 0 – 0 band absorption observed in the experiments (see Figure 6.5). In the presence of PC₆₁BM, S^* slightly shifts for both molecules, as a consequence of the inter-molecular interactions. Both MCT and MH, in dimers or in clusters with PC₆₁BM, show a weak dipole allowed low energy state S_1 . S_1 is more intense for MCT than MH clusters.

The analysis of the electron-hole densities shows that S_1 can be described as

a weak inter-molecular CT state (see partial charge values in the figure 6.9). The presence of PC₆₁BM does not significantly alter neither its character, nor the energy and oscillator strength, being for all cases higher for MCT than MH.

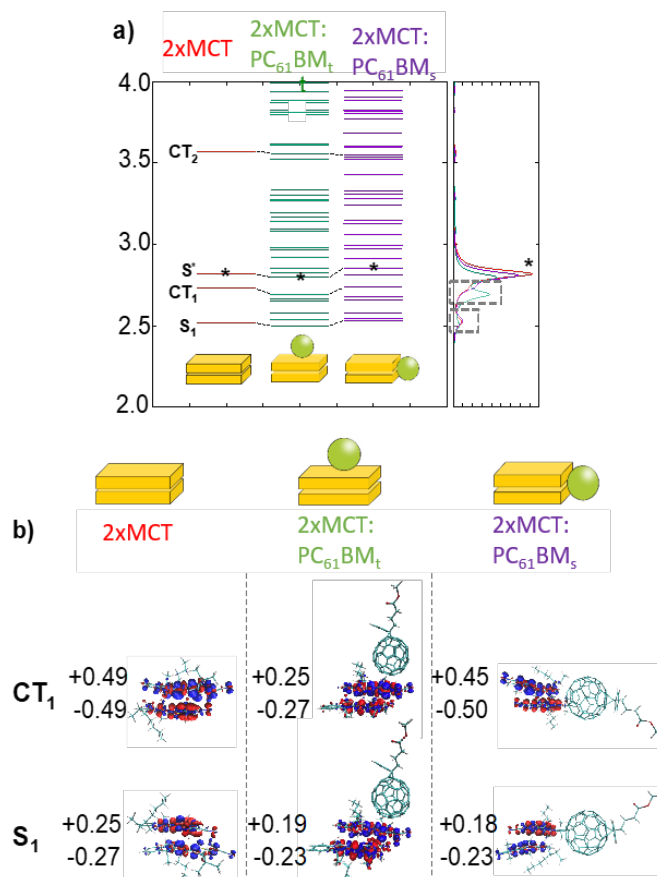


Figure 6.9: a) Computed $TD - \omega B97X - D3/6 - 31G^*$ excited state vertical energies (unscaled values) for MCT molecular clusters, namely: dimers (2xMCT, red), dimer with PC₆₁BM on top (2xMCT:PC₆₁BM_t, green), dimer with PC₆₁BM on side (2xMCT:PC₆₁BM_s, purple). Absorption spectra plotted as convolution of Lorentzian functions. The label (*) represents the optically allowed excited state (in the text S*), here assigned to the 0 – 0 transition. Dotted lines highlight the absorption bands that can be assigned to the stimulated emission transition observed in the experiment at 1.85 eV: electron-hole density plots for CT₁ and S₁ states for the three molecular clusters respectively. Computed partial charges for the merocyanine molecules in CT₁ and S₁ states. Reproduced from[4].

Remarkably, an excited state showing a strong inter-molecular CT character between merocyanines, is predicted below S*. This state is named CT₁ (figure 6.9) and it is present for both on top and on side PC₆₁BM clusters. It derives from the CT₁ transition already present in the pure merocyanine dimer. CT₁ shows a clear electron-hole density separation, localized on the merocyanine domain. Fur-

thermore, its energy, oscillator strength and partial charges are highly affected by the relative position of the PC₆₁BM. For the on-top PC₆₁BM configuration, higher stabilization energy and oscillator strength for CT₁ are computed than the on-side (figure 6.9). For the case of MH clusters, the computed TDDFT energy for the CT state is higher than S^* , and any clear CT state could be located below the optical allowed transition. This aspect might be due to various reasons: i) different local packing and dimer geometries, as induced by different alkyl side chains, ii) a small cluster size considered in the simulations, which is not sufficient for a full description of the electronic structure of MH:PC₆₁BM cases. For such reasons a further computational investigation will be needed to systematically address this point.

Comparing the TDDFT calculations with the experimental data, for the case of MCT we can associate the CT₁ to the stimulated emission band observed at 1.85 eV (figure 6.5). This state is predicted both in pure MCT and in MCT:PC₆₁BM clusters, as also experimentally observed (pure films vs. BHJ, figure 6.5). Because of the aforementioned TDDFT limits in computing the energies of the merocyanine excited states, we cannot completely exclude that the stimulated emission signals might also be assigned to the S_1 state, which shows a weak CT character as well (figure 6.9). We point out that our models are kept minimal in order to explore many structural configurations and to catch the crucial photophysical aspects, however we do not exclude the appearance of further low-lying CT states surrounding the optical gap (S^*) states, the more we increase the cluster size. Similar effects have been reported in literature for oligothiophene: PC₆₁BM clusters[15].

6.2.2 Merocyanine:PC₆₁BM device characterization

Due to a high dipole moment of merocyanine dyes, photogenerated exciton is placed on the nitrile and propyl-amine groups, electron on nitrile and hole on the propyl-amine groups[18]. Two main models which used to describe CT exciton dissociation at the D/A interface are Onsager Braun and Barker models [19, 20]. Both of these models require to have temperature dependent field assisted CT dissociation rate which was not yet observed. This comes to no surprise because of the nature of CT state dissociation: CT state dissociation is an energy releasing process. The CT exciton dissociation and device performance in the framework field dependent tunneling was numerically modeled by Petersen *et al*[21, 22]. In functioning devices the probability of exciton dissociation at the D/A interface could be modeled as the competition between exciton dissociation and recombination processes. First,

model for bound carrier dissociation probability was proposed by Braun *et al*[19]:

$$P_{BP}(F_{el}) = \frac{k_{diss}^{BP}(F_{el})}{k_{diss}^{BP}(F_{el}) + k_{rec}^{BP}(F_{el})} = \frac{1}{1 + k_{rec}^{BP}(F_{el})/k_{diss}^{BP}(F_{el})} \quad (6.1)$$

where $k_{diss}^{BP}(F_{el})$ and $k_{rec}^{BP}(F_{el})$ are dissociation and recombination rates respectively [19]. It shows that with high exciton recombination rate, the overall exciton dissociation probability drops. Recently, a more sophisticated model with a tunneling term was introduced by Petersen *et al.* and it reproduces experimentally observed temperature invariant of CT exciton dissociation rate and a strong dependency on donor:acceptor distance because of tunneling effects[21]. The field dependent tunneling distance is:

$$r_{tunnel}(F_{el}) = r_{tunnel,0} - \frac{-\alpha F_{el}}{2q} \quad (6.2)$$

where α denotes the effective value of the excited state polarizability in the direction of the applied field. It shows how the initial distance between excitons on donor:acceptor interface can determine the exciton dissociation efficiency in terms of tunneling. Also the influence on the local polarizability as shown in equation 6.2 is of crucial importance in explaining the tunneling process at donor/acceptor interface. All this theory strongly indicates that tuning molecular orientation and donor:acceptor interface could change the tunneling term and probability of exciton dissociation P_{ex} via changes in local polarizability α or relative distance $r_{tunnel,0}$ between donor and acceptor molecules.

Based on this theory, the change in micro structure and aggregation, which was observed in the absorption spectra of MCT and MH merocyanine films, should affect device performance of merocyanine based donor:acceptor solar cells. To shed more light on how aggregation could affect exciton splitting and dissociation behavior in electric fields, devices with merocyanine and PC₆₁BM as well as devices with only merocyanine molecules were fabricated.

Device architecture and measurements methods

All solar cells were fabricated on indium–tin oxide (ITO, 125 nm) coated glass. The substrates were exposed to ozone for 3 min and transferred to the evaporation chamber to evaporate 10 nm MoO₃. After transfer to a glove box active layers of 7 nm were spin-coated from chloroform solutions of 13 to 15 mg/ml mixed in a ratio of 2 : 3 (MCT to PC₆₁BM). Neat film were prepared without PC₆₁BM in the same way. The device fabrication was completed by thermal evaporation of 5 nm Ca and

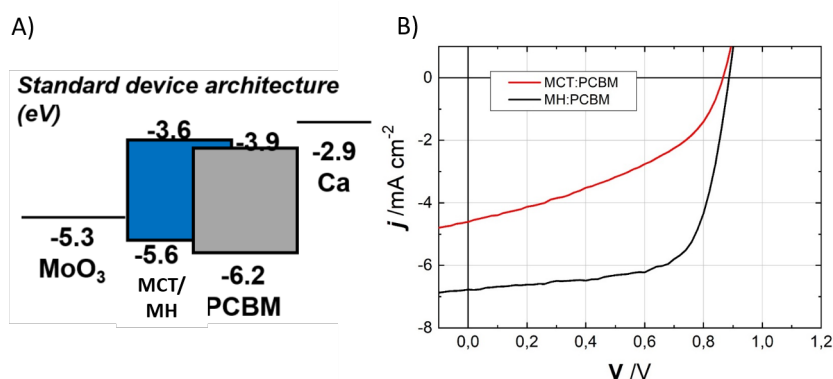


Figure 6.10: a) Device structure of the merocyanine:PC₆₁BM; b) JV curves of devices with two different merocyanine molecules.

Material	V_{oc} [V]	J_{sc} [cm ² /Vs]	FF	PCE [%]	μ [cm ² V ⁻¹ s ⁻¹]	
					SCLC	OFET
MH:PC ₆₁ BM	0.89	6.77	0.68	4.09	$1.5 \cdot 10^{-5}$	
MCT:PC ₆₁ BM	0.87	4.61	0.42	1.66	$1.4 \cdot 10^{-7}$	
MH					$2 \cdot 10^{-5}$	$9 \cdot 10^{-5}$
MCT					$7 \cdot 10^{-7}$	$2 \cdot 10^{-4}$

Table 6.1: Voltamperic characteristics of merocyanine : PC₆₁BM devices; mobilities (in a vertical direction) of pristine films (with OFET architecture) and blend merocyanine films.

120 nm Ag for solar cells or 10 nm MoO₃ and 120 nm Ag for unipolar diodes (SCLC). OFET substrates were obtained from Fraunhofer IPMS Dresden (300 nm SiO₂, C = 15 nF/cm²) and coated with the same solution used for unipolar diodes. The solar cell characteristics were measured using a Keithley 2425 source-measurement unit with a filtered Xe lamp, providing the AM 1.5 G solar spectrum. The intensity of the lamp was adjusted to 100 mWcm⁻². OFETs were characterized using a semiconductor parameter analyzer (Keithley 4200). Mobilities were obtained from saturation regime curves using standard OFET models.

Short circuit current and the free energy of a charge transfer state

Merocyanine based solar cell devices were made with an architecture as shown in the figure 6.10a, voltamperic characteristics of such devices are shown in the figure 6.10 b. To summarize, a strong differences in short circuit current J_{sc} were observed (6.77 cm²/Vs in MH devices versus 4.61 cm²/Vs in MCT devices), leading to dras-

tically different fill factor (FF) and therefor, large differences in power conversion efficiency (PCE). The efficiency (PCE) of MH:PC₆₁BM devices is 4.06% and for MCT:PC₆₁BM its 1.66%. Such strong differences in device characteristics cannot be explained by a simple difference in the amount of absorbed photons, since the integrated area of MCT:PC₆₁BM and MH:PC₆₁BM are 0.142 and 0.119, giving a difference of 19% difference. Second important physical property which could explain the loss in J_{sc} and rationalize such drastic differences in efficiency is different energy of the charge transfer exciton between donor and acceptor. We have used the empirical approximation, described by Veldman *et al.* [23] to attain the CT state energy at room temperature using V_{oc}:

$$E_{CT} = qV_{oc} + 0.47 \text{ eV} \quad (6.3)$$

The free energy of the photo induced electron transfer is defined as $\Delta G_{CT} = E_{CT} - E_g$, where E_g is the band gap of the material. It was shown by Nuzzo. that decrease in the free energy leads to reduced short circuit current (J_{sc}), so by comparing ΔG_{CT} one can get more insights to the cause of decreasing J_{sc} [24].

We have used a similar approach to explain the decline in J_{sc} in PC₆₁BM films based on differences in the free energy ΔG_{CT} . The open circuit voltage (V_{oc}) was deduced from J/V curves and is 0.89 V and 0.87 V for MH:PC₆₁BM and MCT:PC₆₁BM respectively. Using this information the deduced charge transfer state energy E_{CT} is 1.36 eV and 1.34 eV for MH and MCT devices respectively. To calculate the free energy term, the optical gap of both analyzed blends has to be deduced. This can be done from the absorption spectra of both films (figure 6.2). The optical gap E_g of both films are 1.925 eV and 1.91 eV and it was deduced by the linear extrapolation from absorption edge. Using this, the free energy for photo-induced electron transfer ΔG_{CT} for MH and MCT devices is -0.565 eV and -0.57 eV. It is clear that the 46% drop in J_{sc} for MCT:PC₆₁BM devices cannot be explained only by ΔG_{CT} . The drop in short circuit current also could be a result of macroscopical parameters such as different charge carrier mobility or diffusion. It was demonstrated that differences in electron and hole mobilities could lead to a space-charge-limited photo-current caused by imbalance between hole and electron transport[25]. The maximum electrostatically allowed photo current that could be extracted from a device in the space-charge-limited-current regime is

$$J_{ph} = q \left(\frac{9\varepsilon_0\varepsilon_r\mu_h}{8q} \right)^{1/4} R^{3/4}V^{1/2} \quad (6.4)$$

where R denotes the generation rate of electron hole pairs, V is the applied voltage

and is limited by the slowest charge carrier mobility. Koster *et al.* has modeled the current-voltage characteristics of a functioning device using this formula and found that a large drop in the current is caused by the occurrence of a space charge effect which is occurring only when hole and electron mobilities are largely mismatched[26]. In our study, charge carrier mobilities of all devices were measured in two different ways: with space charge limited current (SCLC) and in field effect transistor configuration. For the SCLC measurement merocyanine layers were sandwiched between two MoO₃ layers, resulting in a hole selectivity. Therefore, using this method a hole mobility in pure merocyanine as well as in merocyanine:PC₆₁BM films was extracted. In case of OFET structure, the extracted mobility is not carrier selective. The measured carrier mobility of MCT films using SCLC method is $7 \cdot 10^{-7} \text{ cm}^2\text{V}^{-1}\text{s}^{-1}$, for the same materials, the mobility measured with OFET is $2 \cdot 10^{-4} \text{ cm}^2\text{V}^{-1}\text{s}^{-1}$. The 3 orders of magnitude difference in mobilities means a largely unbalanced carrier mobilities and would result in space charge limited current regime in a solar cell and the reduced short circuit current J_{sc} .

6.3 Conclusions

The intermolecular charge transfer state between two adjacent merocyanine molecules was analyzed using both time resolved spectroscopy and theoretical studies. Experimentally it was shown that different alkene chains of merocyanine molecules can drastically alter the packing behavior of molecules. The charge transfer state was measured using transient absorption spectroscopy and showed a strong stimulated emission signal, associated with it. Theoretical calculations have shown that the relative orientation between PC₆₁BM and merocyanine molecules can change the CT state oscillator strength by means of different delocalization.

6.3.1 Collaborations

The study, presented in this chapter was done with a collaboration with Daniele Fazzi (theoretical calculations of molecular packing and energy levels) and Dirk Hertel (sample preparation and device measurements).

References

1. Li, L. H., Kontsevoi, O. Y. & Freeman, A. J. Orientation-dependent electronic structures and optical properties of the P3HT:PCBM interface: A first-principles GW-BSE study. *J. Phys. Chem. C* **118**, 10263–10270 (2014).

2. Ran, N. A., Roland, S., Love, J. A., Savikhin, V., Takacs, C. J., Fu, Y.-T., Li, H., Coropceanu, V., Liu, X., Brédas, J.-L., Bazan, G. C., Toney, M. F., Neher, D. & Nguyen, T.-Q. Impact of interfacial molecular orientation on radiative recombination and charge generation efficiency. *Nat. Commun.* **8**, 79 (2017).
3. Sharber, S. A. & Thomas, S. W. Small Changes With Big Consequences: Swapping Two Atoms In Side Chains Changes Phenylene-Ethynylene Packing And Fluorescence. *Chem. – A Eur. J.* **24**, 16987–16991 (2018).
4. Budzinauskas, K., Fazzi, D., Hertel, D., R uth, S., Schelter, J., Weitkamp, P., Diesing, S., Meerholz, K. & Van Loosdrecht, P. H. Impact of the Interfacial Molecular Structure Organization on the Charge Transfer State Formation and Exciton Delocalization in Merocyanine:PC61BM Blends. *J. Phys. Chem. C* **124**, 21978–21984 (2020).
5. Eder, R., Janner, a. & Sawatzky, G. Theory of nonlinear optical response of excitons in solid C₆₀. *Phys. Rev. B. Condens. Matter* **53**, 12786–12793 (1996).
6. Nakamura, A., Ichida, M., Yajima, T., Shinohara, H. & Saitoh, Y. Ultrafast relaxation of excitons and photopolymerization in C₆₀ and C₇₀. *J. Lumin.* **66-67**, 383–388 (1995).
7. Kazaoui, S., Ross, R. & Minami, N. Intermolecular charge-transfer excitation in C₆₀ films: Evidence from luminescence and photoconductivity. *Phys. Rev. B* **52**, R11665–R11668 (1995).
8. Bensasson, R. V., Hill, T., Lambert, C., Land, E. J., Leach, S. & Truscott, T. G. Pulse radiolysis study of buckminsterfullerene in benzene solution. Assignment of the C₆₀ triplet-triplet absorption spectrum. *Chem. Phys. Lett.* **201**, 326–335 (1993).
9. Wang, H., He, Y., Li, Y. & Su, H. Photophysical and electronic properties of five PCBM-like C₆₀ derivatives: Spectral and quantum chemical view. *J. Phys. Chem. A* **116**, 255–262 (2012).
10. Isaacs, L., Wehrsig, A. & Diederich, F. Improved purification of C₆₀ and formation of sigma- and pi- homoaromatic methano-bridged fullerenes by reaction with alkyl diazoacetates. *Helv. Chim. Acta* **76**, 1231–1250 (1993).
11. Bencheikh Aboura, F., Duch e, D., Simon, J. J. & Escoubas, L. Ellipsometric study of the optical transitions of PC₆₀BM and PC₇₀BM thin films. *Chem. Phys.* **450-451**, 102–108 (2015).

12. Cook, S., Ohkita, H., Kim, Y., Benson-Smith, J. J., Bradley, D. D. C. & Durrant, J. R. A photophysical study of PCBM thin films. *Chem. Phys. Lett.* **445**, 276–280 (2007).
13. Peckus, D., Deviziš, A., Augulis, R., Graf, S., Hertel, D., Meerholz, K. & Gulbinas, V. Charge Transfer States in Merocyanine Neat Films and Its Blends with [6,6]-Phenyl-C₆₁-butyric Acid Methyl Ester. *J. Phys. Chem. C* **117**, 6039–6048 (2013).
14. Wang, F., Nakano, K., Yoshida, H., Hashimoto, K., Segawa, H., Hsu, C. S. & Tajima, K. Effects of End-On Oriented Polymer Chains at the Donor/Acceptor Interface in Organic Solar Cells. *J. Mater. Chem. A*, 22889–22898 (2018).
15. Bernardo, B., Cheyngs, D., Verreet, B., Schaller, R. D., Rand, B. P. & Giebink, N. C. Delocalization and dielectric screening of charge transfer states in organic photovoltaic cells. *Nat. Commun.* **5**, 1–7. arXiv: arXiv:1011.1669v3 (2014).
16. Ashwell, G. J., Paxton, G. A., Whittam, A. J., Tyrrel, W. D., Berry, M. & Zhou, D. Merocyanine dyes: Self-assembled monolayers. *J. Mater. Chem.* **12**, 1631–1635 (2002).
17. Torabi, S., Jahani, F., Van Severen, I., Kanimozhi, C., Patil, S., Havenith, R. W., Chiechi, R. C., Lutsen, L., Vanderzande, D. J., Cleij, T. J., Hummelen, J. C. & Koster, L. J. A. Strategy for enhancing the dielectric constant of organic semiconductors without sacrificing charge carrier mobility and solubility. *Adv. Funct. Mater.* **25**, 150–157 (2015).
18. Ojala, A., Petersen, A., Fuchs, A., Lovrincic, R., Pölking, C., Trollmann, J., Hwang, J., Lennartz, C., Reichelt, H., Höffken, H. W., Pucci, A., Kirchartz, T. & Würthner, F. Merocyanine/C₆₀ Planar Heterojunction Solar Cells: Effect of Dye Orientation on Exciton Dissociation and Solar Cell Performance. *Adv. Funct. Mater.* **22**, 86–96 (2012).
19. Braun, C. L. Electric field assisted dissociation of charge transfer states as a mechanism of photocarrier production. *J. Chem. Phys.* **80**, 4157–4161 (1984).
20. Barker, J. A., Ramsdale, C. M. & Greenham, N. C. Modeling the current-voltage characteristics of bilayer polymer photovoltaic devices. *Phys. Rev. B - Condens. Matter Mater. Phys.* **67**, 1–9 (2003).
21. Petersen, A., Ojala, A., Kirchartz, T., Wagner, T. A., Würthner, F. & Rau, U. Field-dependent exciton dissociation in organic heterojunction solar cells. *Phys. Rev. B* **85**, 245208 (2012).

22. Petersen, A., Kirchartz, T. & Wagner, T. A. Charge extraction and photocurrent in organic bulk heterojunction solar cells. *Phys. Rev. B* **85**, 045208 (2012).
23. Veldman, D., Meskers, S. C. J. & Janssen, R. A. J. The Energy of Charge-Transfer States in Electron Donor–Acceptor Blends: Insight into the Energy Losses in Organic Solar Cells. *Adv. Funct. Mater.* **19**, 1939–1948 (2009).
24. Di Nuzzo, D., Wetzelaer, G.-J. A. H., Bouwer, R. K. M., Gevaerts, V. S., Meskers, S. C. J., Hummelen, J. C., Blom, P. W. M. & Janssen, R. A. J. Simultaneous Open-Circuit Voltage Enhancement and Short-Circuit Current Loss in Polymer: Fullerene Solar Cells Correlated by Reduced Quantum Efficiency for Photoinduced Electron Transfer. *Adv. Energy Mater.* **3**, 85–94 (2013).
25. Mihailetschi, V. D., Wildeman, J. & Blom, P. W. M. Space-Charge Limited Photocurrent. *Phys. Rev. Lett.* **94**, 126602 (2005).
26. Koster, L. J., Mihailetschi, V. D., Xie, H. & Blom, P. W. Origin of the light intensity dependence of the short-circuit current of polymer/fullerene solar cells. *Appl. Phys. Lett.* **87**, 1–3 (2005).

Summary

The scope of this work covers ultrafast phenomena and excitation dynamics in both organic and hybrid perovskite semiconductors that are used for solar cell applications. For this purpose different types of time resolved spectroscopy techniques were used such as transient absorption and two photon photoemission.

In MAPbI₃ we have used hole extraction layer PEDOT:PSS and transient absorption technique to measure hole mobility in a contactless manner.

It was shown that molecular packing plays a crucial role in organic photovoltaic cells. First of all, the strong nature of polar molecules such as merocyanine can lead to aggregate formation. In our studies, it was shown that investigated merocyanine molecules form H-aggregates. Using experimental and computational methods the 250 meV coupling energy in H-aggregate was deduced. Using two different merocyanine molecules with different packing behavior we were able to show the correlation between packing behavior and the charge transfer exciton formation.

In this study the donor: acceptor type blend with merocyanine and PC₆₁BM was used. We have shown that the relative position between merocyanine and PC₆₁BM (on edge and top of a merocyanine dimer) can change the delocalization of the intermolecular charge transfer exciton on merocyanine dimer. Our experimental findings also were confirmed by computational analysis (DFT).

In a new type of hybrid perovskite: 4 cation, mixed halide GACsFAMA perovskite, it was found that organic counterparts of the material can influence the lifetime of the photoexcited carriers. Using transient absorption, two photon photoemission, and time resolved fluorescence it was found that in hybrid perovskites the long carrier lifetime can be achieved by altering the organic backbone of the material.

List of publications

- E. Jung, K. Budzinauskas, S. Oez *et al.*, Femto - to microsecond dynamics of excited electrons in quadruple cation perovskite, *ACS Energy Lett.*, **5**, 785-792 (2020).
- K. Budzinauskas *et al.*, Impact of the interfacial molecular structure organization on the charge transfer state formation and exciton delocalization in merocyanine:PC₆₁BM Blends, *J. Phys. Chem. C*, **124**, 21978-21984 (2020).
- K. Budzinauskas *et al.*, Charge carrier migration and hole extraction from MAPbI₃, *J.Phys.:Conf. Ser.* **1220** 012053 (2019).
- R. Versteeg *et al.*, Nonequilibrium quasistationary spin disordered state in the Kitaev-Heisenberg magnet α -RuCl₃, *arXiv*:**2005.14189**, (2020).
- F. Sekiguchi *et al.*, Slowdown of photoexcited spin dynamics in the non-collinear spin-ordered phases in skyrmion host GaV₄S₈ (Manuscript submitted for publication).

Offizielle erklärung

Hiermit versichere ich an Eides statt, dass ich die vorliegende Arbeit selbständig und ohne die Benutzung anderer als der angegebenen Hilfsmittel angefertigt habe. Alle Stellen, die Wörtlich oder sinngemäßig aus veröffentlichten und nicht veröffentlichten Schriften entnommen wurden, sind als solche kenntlich gemacht.

Die Arbeit ist in gleicher oder ähnlicher Form oder auszugsweise im Rahmen einer anderen Prüfung noch nicht vorgelegt worden. Ich versichere, dass die eingereichte elektronische Fassung der eingereichten Druckfassung vollständig entspricht.